國立交通大學

電子工程學系 電子研究所

博士論文

低溫強磁場橢偏儀之設計和量測及低能隙量子井厚度相關之電子傳輸有效質量和遷移率

Low Temperature and High Magnetic Field Ellipsometer Design and Measurement & Well-thickness Dependent Electron Transport Effective Mass and Mobility in Low Bandgap Quantum Wells

研究生：蘇聖凱

指導教授：李建平 教授

中華民國一〇三年六月

低溫強磁場橢偏儀之設計和量測及低能隙量子井厚度相關之電子傳輸有效質量和遷移率

Low Temperature and High Magnetic Field Ellipsometer Design and Measurement & Well-thickness Dependent Electron Transport Effective Mass and Mobility in Low Bandgap Quantum Wells

研究生：蘇聖凱　　Student：Sheng-Kai Su

指導教授：李建平　　Advisor：Chien-Ping Lee

國立交通大學
電子工程學系 電子研究所
博士論文

A Dissertation
Submitted to Department of Electronics Engineering and
Institute of Electronics
College of Electrical and Computer Engineering
National Chiao Tung University
in Partial Fulfillment of the Requirements
for the Degree of
Doctor of Philosophy
in
Electronics Engineering

June 2014
Hsinchu, Taiwan, Republic of China

中華民國一〇三年六月

低溫強磁場橢偏儀之設計和量測及低能隙量子井厚度相關之電子傳輸有效質量和遷移率

學生：蘇聖凱　　　　　　　　　　　　　　　　指導教授：李建平 博士

國立交通大學

電子工程學系 電子研究所 博士班

摘　　要

論文的第一部分涵蓋了光譜橢偏儀在近紅外波段（700-1000nm）可使樣品置於低溫（～4.2Ｋ）和強磁場（磁場最高達 14T）下量測的設計和實現。論文中將詳細探討在低溫環境下系統的光學和機械的各個組成部分。我們把主要的光學原件都結合在一個可插入到常規的長頸液態氦杜爾瓶的探測器上，這樣的設計使得系統擁有很長的空宇光路徑（～ 1.8 ｍ × 2）。在偏振光的解析方面，我們使用偏振片-樣品-（四分之一波片）-旋轉偏振片的橢偏儀配置。在光路方面，我們用兩個介電反射鏡，一個在樣品前，另一在樣品之後；而在樣品座下的兩軸壓電驅動傾角器則可用來調控反射光的方向，使光能順利反射回旋轉偏振片而被量測。系統的功能性量測結果和其隨機誤差的分析都將在文中展示。我們用此自行設計的橢偏儀系統探索砷化鎵極化子在磁場下傳播的特性。藉此，我們可同時量測到砷化鎵激子橢偏光譜的振幅和相位頻譜以及其相位譜在能量接近砷化鎵激子躍遷時，光左、右旋的轉變。更重要的，我們藉此量測方法觀察到有趣且未曾被發表過的砷化鎵激子光譜的精細結構，且這些精細結構的磁光行為無法由已知特性的激子態做解釋。鑑於此，我們把樣品的表面和磊晶界面都當作砷化鎵極化子的邊界，如此可解釋這些精細結構的由來並歸咎其為多重極化子模態間的干涉結果。而對於此干

涉精細結構的磁響應，我們提出了一個同時考慮極化子的空間色散和激子的中心運動與相對運動耦合所導致的有效質量提升的模型對其做定性的解釋。

在論文的第二部分，我們提出了一個設計特殊半導體量子井的想法，這種量子井相對於一般的量子井而言；即使厚度減小，仍能提供較小的電子傳輸有效質量和較高的遷移率。在理論計算中，我們同時考慮了能帶的非拋效應和量子井能障所帶來的影響。在低溫情況下，主要的散射機制包括界面粗糙度，合金無序和雜質的散射均被用來評估電子在量子井中的遷移率。四種不同組合的低能隙量子井的結果和比較都將在文中展現。通過適當選取合適的能帶組合的量子井和其能障的材料，此新穎的傳輸特性可被實現。

Low Temperature and High Magnetic Field Ellipsometer Design and Measurement & Well-thickness Dependent Electron Transport Effective Mass and Mobility in Low Bandgap Quantum Wells

Student：Sheng-Kai Su Advisor：Dr. Chien-Ping Lee

Department of Electronics Engineering & Institute of Electronics
National Chiao Tung University

ABSTRACT

The first part of this thesis covers the design and implementation of a spectral ellipsometer at near-infrared wavelength (700-1000nm) for samples placed in high magnetic fields (up to 14 Tesla) at low temperatures (~4.2 K). It details both the optical and mechanical aspects of the system in the low temperature environment. The main optical components are integrated in a probe, which can be inserted into a conventional long-neck He dewar and has a very long free-space optical path (~1.8 m x 2). A polarizer-sample-(quarter-wave plate)-rotating analyzer configuration was employed. Two dielectric mirrors, one before and one after the sample in the optical path, helped to reflect the light back to the analyzer and a two-axis piezo-driven goniometer under the sample holder was used to control the direction of the reflected light. Functional test results and analysis on the random error of the system are shown. The properties of GaAs polariton propagating in magnetic field have been explored using this self-designed ellipsometry system. We obtained both the amplitude and phase ellipsometric spectra simultaneously and observed helicity transformation at energies near the GaAs exciton transitions in the phase spectra. Interesting fine structures, which have not been reported before, have been observed and their magneto-optical behavior cannot be accounted by the known properties of excitonic states. Treating the surface and the growth interface as boundaries, we attribute the fine structures to the interference among various polariton modes.

A model considering both the polariton spatial dispersion and the exciton effective mass enhancement induced by the coupling of the exciton center of mass and relative motions is proposed to explain the magnetic response of the interference ellipsometry spectra.

In the second part of this thesis, we propose an ideal to design a special kind of semiconductor quantum wells, which, in contrary to conventional quantum wells, are able to provide smaller electron transport effective mass and higher mobility when the quantum well thickness is decreased. The theory used accounts for both the nonparabolicity effect and the influence of the barrier. Major scattering mechanisms at low temperatures, including the scatterings by the interface roughness, the alloy disorder, and impurities have been considered in mobility calculations. The results of four different combinations of quantum wells are shown and compared. By properly choosing the well/barrier materials with proper band lineups, the novel transport property is achievable.

誌謝

我要感謝在我完成研究計畫的過程中許多給予我幫助和支持的人。我首先要感謝我的指導教授，李建平老師，給予我很大的自由，很充沛的資源去完成我本來從未以為我能完成的事。與老師談話時常能激發我的一些想法，事實上，論文中第二部分的想法就是源自於一次午餐閒聊時老師的提問。感謝多年來老師不論在研究還是生活上的提點和信心的給予讓我可以安心的走在想要走的道路上。

我還要感謝中興大學物理系的孫允武老師。沒有他的幫助，我將無法順利完成低溫強磁場橢偏儀的建製。感謝孫老師對於專業知識以及期刊論文寫作的幫助和指導。從他身上我學到做科學研究以及論文寫作的嚴謹態度。儀器的完成還仰賴許多人的幫助。感謝李良箴博士在儀器機械和低溫系統部分給予的幫助，巫朝陽同學在儀器控制和自動化方面的付出，郭鴻榮學弟幫忙畫的 3D 設計圖以及宋育泰工程師對於實驗上的幫助。

I would like to thank Professor Oleksandr Voskoboynikov, whose humor and meaningful discussions, helping me overcome many difficulties in theoretical calculations.

還要感謝林聖迪老師午後的 coffee time “閒聊” 和給予的許多研究上和未來規劃上的建議。感謝實驗室的學長：羅明城、林大鈞、凌鴻緒、陳建旭的帶領和指導以及同學、學弟妹們：潘建宏、李宗霖、林岳明、林建宏、許宏任、李依珊 *et al.*的幫助。

最後我要感謝我的父母，他們的付出和支持，讓我即使已近而立之年仍無憂於“養家活口”的重責而能埋首於書本和研究之中。歲月無聲，縱使帶走厚厚的青春，卻也留下許多回憶。那些辛苦、挫折與小小的成就，現今「也無風雨也無晴」了。

蘇聖凱 謹誌於
國立交通大學電子所

中華明國一〇三年五月

Contents

List of Figures

List of Tables

Abbreviations

ABC	**A**dditional **B**oundary **C**ondition
ADS	**A**lloy **D**isorder **S**cattering
Amp	**Amp**lifier
BIS	**B**ackground **I**mpurity **S**cattering
CM	**C**enter of **M**ass
DVM	**D**igital **V**oltage **M**eter
FWHM	**F**ull **W**idth at **H**alf **M**aximum
IRS	**I**nterface **R**oughness **S**cattering
MBE	**M**olecular **B**eam **E**pitaxy
PEM	**P**hoto-**E**lastic **M**odulator
QW	**Q**uantum **W**ell
RAE	**R**otating **A**nalyzer **E**llipsometry
RIS	**R**emote **I**mpurity **S**cattering
SI	**S**emi **I**nsulating
SIMS	**S**econdary **I**on **M**ass **S**pectrometer

Physical Constants

Speed of Light in Vacuum $c = 2.99792 \times 10^{8}\ \mathrm{ms}^{-1}$

Mass of Electron $m_0 = 9.10938 \times 10^{-31}\ \mathrm{kg}$

Planck's Constant $\hbar = 1.05457 \times 10^{-34}\ \mathrm{J\ s}$

Charge of Electron $e^- = 1.60218 \times 10^{-19}\ \mathrm{C}$

Permeability of Free Space $\mu_0 = 4\pi \times 10^{-7}\ \mathrm{NA}^{-1}$

Permittivity of Free Space $\varepsilon_0 = 8.8542 \times 10^{-12}\ \mathrm{Fm}^{-1}$

Bohr Radius $a_0 = 0.5292 \times 10^{-10}\ \mathrm{m}$

Bohr magneton $\mu_B = 927.4 \times 10^{-26}\ \mathrm{JT}^{-1}$

Symbols

A	analyzer angle	degree (°)
A	sample area	m^2
a_{lc}	lattice constant	$\mathring{A}$
B	magnetic field (induction) of magnets	T
$\mathcal{D}$	displacement field	$\mathrm{FV\ m}^{-2}$
E	electric field	$\mathrm{V\ m}^{-1}$
E	electron energy	eV
E_g	bandgap energy	eV
H	magnetic field	$\mathrm{A\ m}^{-1}$
I	light intensity	W
k	electron in-plane wavevector	m^{-1}
l	QW thickness	nm
M_{ex}	exciton center of motion effective mass	m_0
$m_{e,h}$	electron/hole effective mass	m_0
$\mathcal{P}$	polarization	$\mathrm{FV\ m}^{-2}$
$\mathbf{p}$	momentum	$\mathrm{J\ s\ m}^{-1}$
p	polarization parallel to incident planes	
q	wavevector	m^{-1}
q	change of the electron in-plane wavevector	m^{-1}
$\mathbf{r}$	space coordinate	m
r	reflection coefficient	
s	polarization perpendicular to incident planes	
T	temperature	K

t	time	s
V	potential energy	eV
Y	admittance	S
Z	impedance	Ω
Π	polarizer angle	degree ($^\circ$)
Ψ	real part of ellipsometry parameter	degree ($^\circ$)
θ	incidence angle	degree ($^\circ$)
θ	scattering angle	degree ($^\circ$)
ψ	wavefunction	
Δ	imaginary part of ellipsometry parameter	degree ($^\circ$)
ω	angular frequency	s^{-1}
ε	dielectric function	Fm^{-1}
ϵ	strain tensor	
χ	susceptibility	
τ	scattering relaxation time	s
μ	reduce mass	m_0
μ	mobility	$\mathrm{cm}^2\ (\mathrm{V\text{-}s})^{-1}$

Dedicated to my parents

Part I

Low Temperature and High Magnetic Field Ellipsometer Design and Measurement

Chapter 1

Introduction

Taking precise and careful measurements of subtle phenomena in semiconductors is very important in understanding the physical properties of the material. In the first part of the thesis, we describe the design and construction of an ellipsometer that can be used in high magnetic field and low temperatures. This is an unique scientific instrument, which is able to perform measurements that could not be done before. A lot of innovative ideas have been used and many difficult obstacles have been overcome in this challenging project. This is the first and the only ellipometer in the world that can be operated in such harsh environment. The system has been fully tested and characterized. We have used it in the study of exciton-polariton properties of GaAs. It has provided information that could not be achieved otherwise.

1.1 Ellipsometry

Ellipsometry is a technique to measure the change of a polarization state of light after being interacted with sample [1–3]. From analysing the polarization change, we can explore the light-matter interaction and deduce parameters such as overlayer/film thickness and complex dielectric functions [1–3]. More specifically, the spectroscopic ellipsometry is able to measure wavelength dependent complex dielectric functions providing additional information on the electronic states and the band structure of crystalline materials. This is especially important for semiconductor analysis and is useful for optoelectronic applications. Unlike reflectance and photoemission spectra, spectroscopic ellipsometry simultaneously provides both real and imaginary parts of ellipsometric spectra connected to the complex dielectric function, which fully characterizes the inherent wavelength dependence linear response (both the absorption and dispersion) of materials.

Its high sensitivity integrated with a high magnetic field (B) and low temperature (T) environment for the sample has attracted researchers to utilize such a technique to explore interesting quantum electron systems of which the optical response can show very intriguing effect induced by B. For many of these studies, especially on new phenomena of materials and new structures, it is desirable that these measurements are performed at low temperatures (T) and high magnetic fields (B). For example, nonmagnetic semiconductor nano-object based artificial materials have been proposed to exhibit magnetic-material-like collective optical responses which can be revealed by low-T and high-B ellipsometric measurements [4–8]. Another area of interest is the spatial dispersive exciton-polariton related problems [9–13], for which the obliquely incident geometry nature and high-B fields provide extra information of the momentum space parallel to the interface and the effect of spin configurations. We believe such a comprehensive study will help to develop the microscopic theory of exciton-polariton behaviors in magnetic fields. Therefore a versatile but miniature ellipsometer that can be fitted into and operated in a low temperature and high magnetic field environment is of great importance for the studies mentioned above.

A generalized magneto-optical ellipsometry system was proposed by Berger *et al.* [14] to obtain complex refraction index and magneto-optical coupling constant simultaneously. Later, Neuber *et al.* [15] showed a temperature-varying generalized spectral magneto-optical ellipsometer design with a He-flow cryostat and a small electromagnet of a few tens of mT. Schubert *et al.* [16] extended this technique to far-infrared and a higher magnetic field of a few Tesla to characterize the carrier properties of n-GaAs; Hofmann *et al.* [17] further pushed the technique to terahertz frequency range. Mok *et al.* [18] presented a variable-angle vector-magneto-optical generalized ellipsometer with field magnitude up to 400 mT at room temperature. However, all the previous systems had relatively short optical path designs and were equipped with small coil magnets or split-coil superconducting magnets, which limited the strength of the applied magnetic fields. To extend the operation range of the spectroscopic ellipsometry systems to higher magnetic fields, a new approach to design a ellipsometer is presented in this thesis.

1.2 Exciton-Polariton Light Semiconductor Coupling

As mentioned above, the self-designed ellipsometer performs measurements different from common reflectance and transmission experiments for the sample in the low temperature and high magnetic field environment. We use it to investigate the properties of GaAs exciton-polariton propagation in high magnetic fields. The term "exciton-polariton", was first introduced by J. J. Hopfield [19] to refer to the coupling of the electromagnetic field and the excitonic polarization field in semiconductors. This concept has exerted considerable influences on researches in the linear optical regime [20–23] and on future applications such as plasma-gain lasing [24, 25], low energy switches [26–28], single photon sources [29–31], etc. When spatial dispersion of polaritons [32, 33] in the presence of interfaces is considered, the polariton problem becomes more complicated. Lack of knowledge on the exciton polarization near interfaces leads to various types of "additional boundary condition"(ABC) [32, 34–36] be proposed to match the multi-polariton modes in the material and the single electromagnetic wave at an interface.

Over the past 20 years there have been a lot of researches on polariton effects in GaAs QWs for fundamental and practical reasons. These effects have been explained by the interference among multi-polariton modes and the exciton center-of-mass (CM) motion quantization. And the mechanisms exchange dominating for different QW thickness comparing to the photon wavelength and the exciton Bohr radius in the material [37, 38]. For a thick quantum well (QW), some features have been observed and have been explained as due to the interference among multi-polariton modes [39]. When the layer thickness is reduced, the exciton center-of-mass (CM) motion quantization has been expected to play a more important role [38]. However, to recognize all the features induced by these coupled mechanisms is complicated. Recently, more elaborate microscopic models [10–13] have been developed to explain the interplay of the interference of polariton and the CM motion quantization for intermediate sample length and have an excellent agreement with recent experimental results [9]. However, no such treatments with magnetic fields have been published up to now.

Applying magnetic fields to semiconductors has attracted many interests in studying the behavior of magneto-exciton and being available to obtain the important parameters (diamagnetic shift coefficient, g-factor, band-parameters, etc.) of material [40]. The last decade has seen growing importance placed on research in the magnetic field induced phenomena due to the coupling between the quantized exciton CM and relative motions [41–44]. Magnetic fields are not only a perturbation but also lead coupling of exciton CM motion and internal motion [41, 42, 45, 46], and possibly induces mixing of the exciton s-state and other states [43, 44]. This is especially important for the sample that the exciton can move freely in magnetic fields. However, all the experiments published previously were done with a normal-incidence configuration that can not provide a wavevector parallel to the sample surface and obliquely moving excitons in magnetic fields.

1.3 Scope of Part I

Having an ellipsometer that can operate at low temperatures and high magnetic fields makes it possible to perform experiments mentioned above in a different way. The first part of the research (Chapter 2) details the design, construct and characterization of the spectroscopic ellipsometry system that can be inserted into an Oxford long-neck low temperature dewar, which is equipped with a superconducting magnet with field up to 14 T. This ellipsometer employs free space optics to bring the polarized light in and out of the sample stage, which is placed ∼1.6 m deep into the cryostat. Specific mechanical design to control the light beam and stabilize the overall system is presented. The system is fully tested and functional, and has provided magneto-optical spectroscopic information of our samples with high resolution and clarity.

The second part of this work involves measuring III-V semiconductor samples using the self-designed ellipsometer. More specifically, we study the behavior of GaAs polariton in a substrate and a 1-μm layer grown by molecular beam epitaxy (MBE) in high magnetic fields at 4.2 K. Unlike the previous measurements done with a normal incident angle, our measurements were performed with an oblique (60°) incident angle under variable magnetic fields up to 14 Tesla (T) and were able to show simultaneously both the phase and the amplitude ratios of the two principal axis reflectivities.

From the measurement done with taking the ratio of the two principal-axis reflectivities and a large wavevector component parallel to the interfaces of a GaAs epilayer, fine structures in the ellipsometry spectra were observed. The peculiar structures, which cannot be seen in our GaAs substrate sample and have not been reported in the previous measurements of GaAs epilayer [47–52], were present even at 0 T. The fine structures evolved with the magnetic field in a fashion that cannot be explained by the traditional models of the magnetic field induced quantization.

Treating our sample as a slab of GaAs with two boundaries , which are the surface and the epilayer-substrate interface, and using the theory of the dispersive polariton with Pekar's ABC [32, 36], we were able to explain qualitatively the observed fine structures in the ellipsometry spectra as a result of the interference among various polariton modes in the slab. The behavior of the spectra under magnetic fields was explained as a possible result of the enhancement of exciton effective mass [45, 46], which is due to the coupling of the exciton CM and relative motions in the presence of magnetic field. We hope the results and their explanations provided in this work can stimulate an appropriate theoretical description.

Chapter 2

Ellipsometry System Design & Measurements

2.1 Description of The Complete System

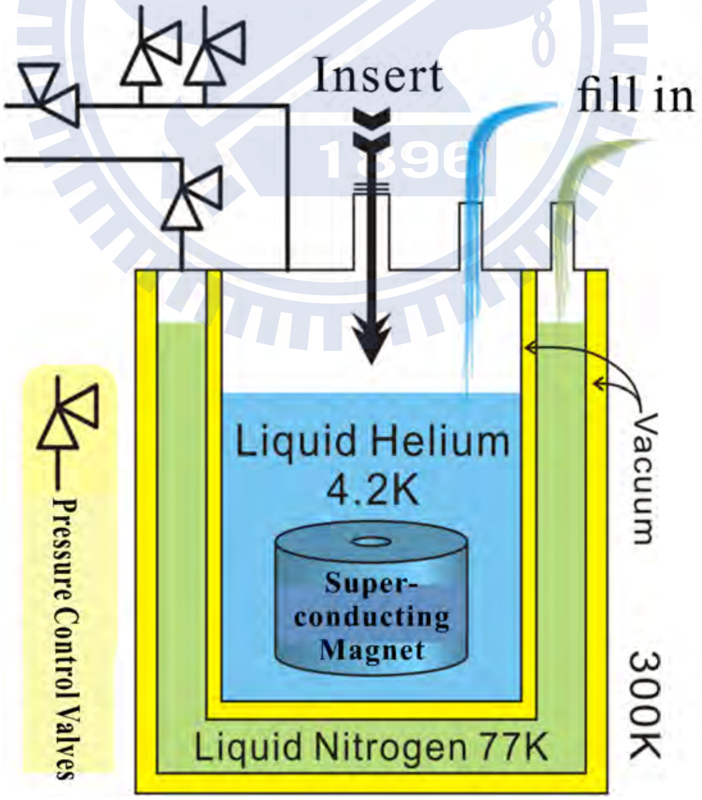

FIGURE 2.1: Diagram of the long-neck liquid-Helium dewar with a liquid-Nitrogen jacket.

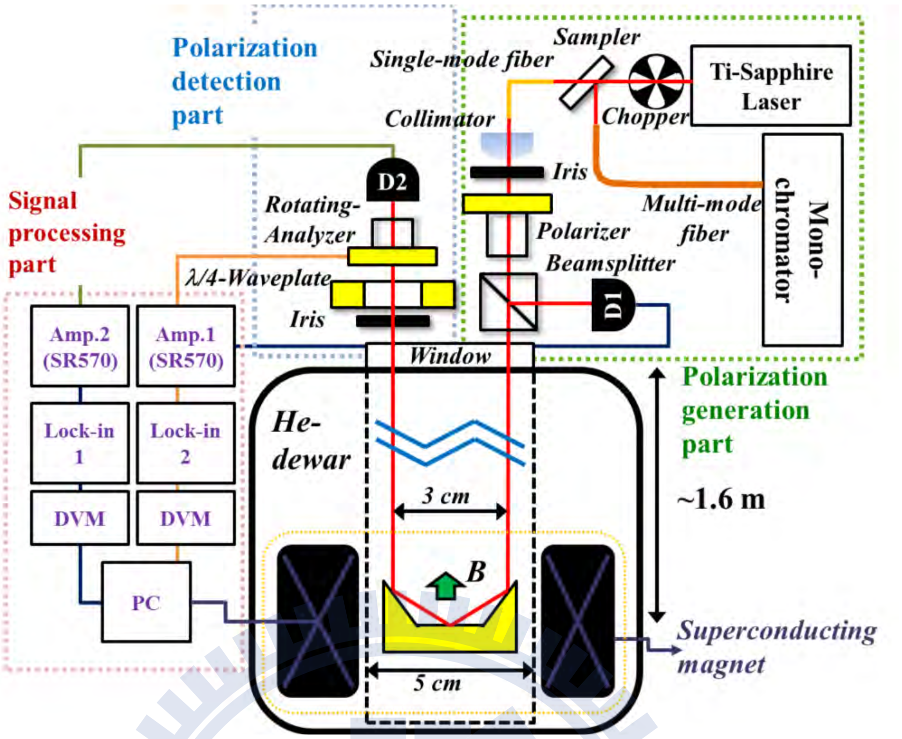

Figure 2.2: Schematic diagram of the ellipsometery system, which can be fit into a long-neck cryogenic dewar with a small-bore high-field superconducting magnet.

To overcome the constraints of the small bore size (50 mm) of the high-field (14 T) superconducting magnet and a long optical path set by the long-neck liquid-Helium dewar with a liquid-Nitrogen jacket (Fig. 2.1), we designed a multi-reflection sample stage mounted at the end of an insert. The laser beam is brought in through free-space along the insert. In this way, we are able to maintain a large incident angle and high polarization stability of the laser beam into the sample as required by an ellipsometry system. To make sure the laser beam traveling from the top window of the dewar can go back to the same window after being reflected by the sample at the center of the magnet that is placed near the bottom of the dewar, we use two dielectric mirrors besides the sample under test to form a triple-reflection configuration.

Figure 2.2 shows the complete schematic diagram of the ellipsometry system. The whole system was constructed as an insert for the low temperature dewar. It consists of a polarization generation part, a polarization detection part, a signal processing part, and a sample stage that holds the sample and the two dielectric mirrors in a low-temperature environment. A Ti-sapphire laser provides the coherent light in the wavelength range of 700 nm to 1000 nm and its FWHM linewidth is about 3 Å. The laser beam is firstly split into two by a beam-sampler. One beam is coupled into a monochromator for wavelength measurement, and the other is coupled into a 10-m long single-mode fiber ended with a collimator. The light out of the collimator passes through a Glan-Laser calcite polarizer with an extinction ratio larger than 10^5 and then becomes a linearly polarized light. One of the laser beams being branched out by the beam-splitter is detected by a silicon photodiode (D1) to monitor the fluctuation of polarization and intensity, while the other beam is guided into the cryogenic dewar through a window at room temperature. The incident beam is reflected by a dielectric mirror before reaching the sample. The outgoing beam is reflected by another dielectric mirror and then goes to the polarization detection part placed outside the dewar. The polarization detection part includes a quarter-wave plate, a rotating analyzer, and another silicon photodiode (D2). The photocurrents from D1 and D2 are measured by lock-in amplifiers and current preamplifiers respectively in the signal processing part. All reflections, two from the mirrors and one from the sample, have a 60° incident angle and share the same incident plane, making the incoming beam and outgoing beam parallel to each other. The holder containing the mirrors and sample is attached to a two-axis piezoelectric goniometer which can tune the sample orientation in-situ.

2.2 Operation Principle

The polarization state of a light beam can be expressed in the form of Jones vector [1–3]. For a triple-reflection process, the output and input Jones vectors are related by

$$\begin{aligned}\begin{pmatrix} p_{\text{out}} \\ s_{\text{out}} \end{pmatrix} &= \begin{pmatrix} r^{\text{C}}_{pp} & r^{\text{C}}_{sp} \\ r^{\text{C}}_{ps} & r^{\text{C}}_{ss} \end{pmatrix} \begin{pmatrix} r^{\text{B}}_{pp} & r^{\text{B}}_{sp} \\ r^{\text{B}}_{ps} & r^{\text{B}}_{ss} \end{pmatrix} \begin{pmatrix} r^{\text{A}}_{pp} & r^{\text{A}}_{sp} \\ r^{\text{A}}_{ps} & r^{\text{A}}_{ss} \end{pmatrix} \begin{pmatrix} p_{in} \\ s_{in} \end{pmatrix} \\ &\equiv \begin{pmatrix} r^{\text{eff}}_{pp} & r^{\text{eff}}_{sp} \\ r^{\text{eff}}_{ps} & r^{\text{eff}}_{ss} \end{pmatrix} \begin{pmatrix} p_{in} \\ s_{in} \end{pmatrix} = \mathbf{r}^{\text{eff}} \begin{pmatrix} p_{in} \\ s_{in} \end{pmatrix}, \end{aligned} \tag{2.1}$$

where p and s are the electric field components parallel and perpendicular to the incident plane, and r is the complex reflection coefficient with subscripts and superscripts specifying the polarization states and reflecting materials, respectively. For example, r^B_{ps} represents the ratio of the s-component of the light reflected by the sample in the middle and the p-component of the incident light. The effective reflection matrix, $\mathbf{r}^{\text{eff}}$, represents the overall result of all three reflections. The ratio of the output and input ratios of the p- and s- polarization components is defined as [53]

$$\begin{aligned}\rho &= \frac{p_{out}/s_{out}}{p_{in}/s_{in}} = \frac{(r^{\text{eff}}_{pp}/r^{\text{eff}}_{ss}) + (r^{\text{eff}}_{sp}/r^{\text{eff}}_{ss})(p_{in}/s_{in})^{-1}}{1 + (r^{\text{eff}}_{pp}/r^{\text{eff}}_{ss})(r^{\text{eff}}_{ps}/r^{\text{eff}}_{pp})(p_{in}/s_{in})} \\ &= \frac{R^{\text{eff}}_{pp} + R^{\text{eff}}_{sp}(p_{in}/s_{in})^{-1}}{1 + R^{\text{eff}}_{pp}R^{\text{eff}}_{ps}(p_{in}/s_{in})},\end{aligned} \tag{2.2}$$

where [16, 53]

$$R^{\text{eff}}_{pp} = \frac{r^{\text{eff}}_{pp}}{r^{\text{eff}}_{ss}} = \tan\Psi^{\text{eff}}_{pp} e^{i\Delta^{\text{eff}}_{pp}}; \tag{2.3a}$$

$$R^{\text{eff}}_{sp} = \frac{r^{\text{eff}}_{sp}}{r^{\text{eff}}_{ss}} = \tan\Psi^{\text{eff}}_{sp} e^{i\Delta^{\text{eff}}_{sp}}; \tag{2.3b}$$

$$R^{\text{eff}}_{ps} = \frac{r^{\text{eff}}_{ps}}{r^{\text{eff}}_{pp}} = \tan\Psi^{\text{eff}}_{ps} e^{i\Delta^{\text{eff}}_{ps}}, \tag{2.3c}$$

$\tan\Psi$ and Δ stand for the amplitude ratio and the phase difference of the reflectivities.

To extract the reflection information from the triple-reflection measurement, we must obtain the effect of the dielectric mirrors first. This can be done through a calibration procedure by using three identical mirrors, i.e., using the same dielectric mirror (M) to replace the sample. The overall result of the three identical reflections then has the form

$$\begin{pmatrix} (r^{\text{M}}_{pp})^3 + 2f^{\text{M}}_{pp} + f^{\text{M}}_{ss} & r^{\text{M}}_{sp}F^{\text{M}} \\ r^{\text{M}}_{ps}F^{\text{M}} & (r^{\text{M}}_{ss})^3 + 2f^{\text{M}}_{ss} + f^{\text{M}}_{pp} \end{pmatrix}, \tag{2.4}$$

where $f^{\text{M}}_{pp} = r^{\text{M}}_{pp}r^{\text{M}}_{ps}r^{\text{M}}_{sp}$, $f^{\text{M}}_{ss} = r^{\text{M}}_{ss}r^{\text{M}}_{ps}r^{\text{M}}_{sp}$, and $F^{\text{M}} = (r^{\text{M}}_{pp})^2 + r^{\text{M}}_{ps}r^{\text{M}}_{sp} + r^{\text{M}}_{pp}r^{\text{M}}_{ss} + (r^{\text{M}}_{ss})^2$. Here we assume the reflection coefficients to be the same due to the same material and identical incident angle. The ellipsometry parameters for each mirror can be obtained with neglecting the product of $r^{\text{M}}_{ps}r^{\text{M}}_{sp}$ terms that are at least three orders smaller than the product of diagonal terms in general.

$$R^{\text{M}}_{pp} = (R^{\text{cal}}_{pp})^{1/3}; \tag{2.5a}$$

$$R^{\text{M}}_{sp} = R^{\text{cal}}_{sp}[(R^{\text{cal}}_{pp})^2 + R^{\text{cal}}_{pp} + 1]^{-1}; \tag{2.5b}$$

$$R^{\text{M}}_{ps} = R^{\text{cal}}_{ps}[(R^{\text{cal}}_{pp})^{-2} + (R^{\text{cal}}_{pp})^{-1} + 1]^{-1}. \tag{2.5c}$$

The superscript "cal" represents the three identical mirror calibration measurement.

For a measurement where the second mirror is replaced by a sample (σ), the effective reflectivity matrix becomes

$$\begin{pmatrix} (r^{\mathrm{M}}_{pp})^2 r^{\sigma}_{pp} & r^{\mathrm{M}}_{pp} r^{\mathrm{M}}_{ss} r^{\sigma}_{sp} + g_{sp} \\ g_{ps} + r^{\mathrm{M}}_{pp} r^{\mathrm{M}}_{ss} r^{\sigma}_{ps} & (r^{\mathrm{M}}_{ss})^2 r^{\sigma}_{ss} \end{pmatrix}, \tag{2.6}$$

where $g_{sp/ps} = r^{\mathrm{M}}_{sp/ps}(\mathrm{r}^{\mathrm{M}}_{ss}\mathrm{r}^{\sigma}_{ss} + \mathrm{r}^{\mathrm{M}}_{pp}\mathrm{r}^{\sigma}_{pp})$. The ellipsometry parameters of the sample (σ) are then obtained by Eg. (2.3) as

$$R^{\sigma}_{pp} = \frac{R^{\mathrm{eff}}_{pp}}{(R^{\mathrm{M}}_{pp})^2}; \tag{2.7a}$$

$$R^{\sigma}_{sp} = [R^{\mathrm{eff}}_{sp} - R^{\mathrm{M}}_{sp}(1 + \frac{R^{\mathrm{eff}}_{pp}}{R^{\mathrm{M}}_{pp}})](R^{\mathrm{M}}_{pp})^{-1}; \tag{2.7b}$$

$$R^{\sigma}_{ps} = [R^{\mathrm{eff}}_{ps} - R^{\mathrm{M}}_{ps}(1 + \frac{R^{\mathrm{M}}_{pp}}{R^{\mathrm{eff}}_{pp}})]R^{\mathrm{M}}_{pp}. \tag{2.7c}$$

The mirror contributions R^{M}_{pp}, R^{M}_{sp}, and R^{M}_{ps} can be deduced from the three-mirror calibration procedure in Eq. (2.5).

2.3 Mechanical Design

The main part of the ellipsomety system is designed as a long insert (Fig. 2.3) to fit into an Oxford He long-neck dewar (Fig. 2.1). Because of the long distance (∼1.8 m) between the center of magnetic field and the outlet window and the extreme conditions in the dewar, the mechanical design of the ellipsometer has to be done very carefully to ensure stable operation and ruggedness under harsh conditions. It also needs to be flexible enough to allow fine adjustment of the optical path to make sure that the light beam travels through free space to the sample and back to the polarization detection part accurately. The main mechanical support of the insert is provided by four parallel 6 mm-outside-diameter stainless-steel tubes, which are kept in place and separated by several aluminum spacer plates. In each of the spacer plate, there are two cross-shaped holes to allow the laser beams to travel through. Such a frame structure avoids the possibility of bending the insert frame and also suppresses mechanical vibrations. The top of the frame structure,

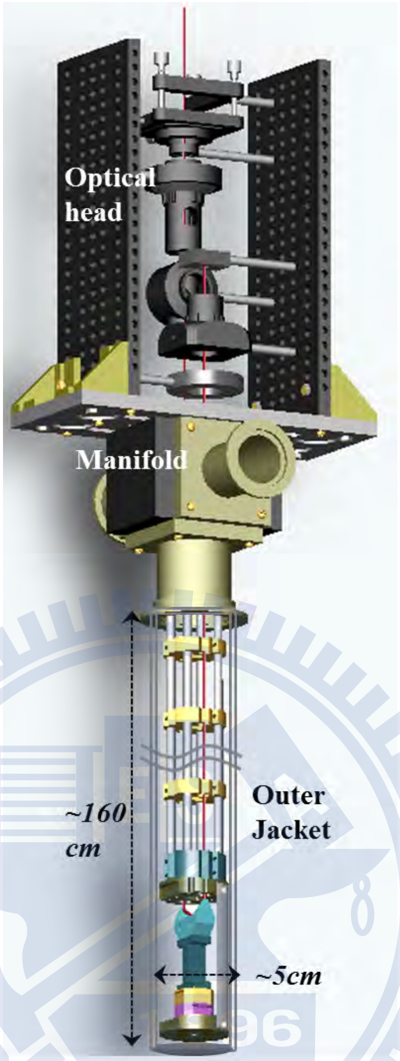

FIGURE 2.3: Overall view of the ellipsometer insert.

as shown in Fig. 2.4 (a), is connected to a manifold that supports the optical head and provides necessary ports for pumping and electrical feedthroughs. The optical head mainly consists of two 25 cm ×10 cm ×1 cm parallel optical breadboards that hold the optical components and detectors. The bottom of the insert, as shown in Fig. 2.4 (b), includes a sample stage, a two-axis piezoelectric goniometer and a protective housing, whose material are all titanium. Between components of different materials, beryllium-copper washers are used to reduce the deformation caused by different contractions at low temperatures. To ensure the reflected beam reaching the polarization detection part, the sample stage is mounted on a two-axis piezoelectric goniometer with its rotation center coinciding with the sample position to provide a very precise and instantaneous angle-control without sample displacement.

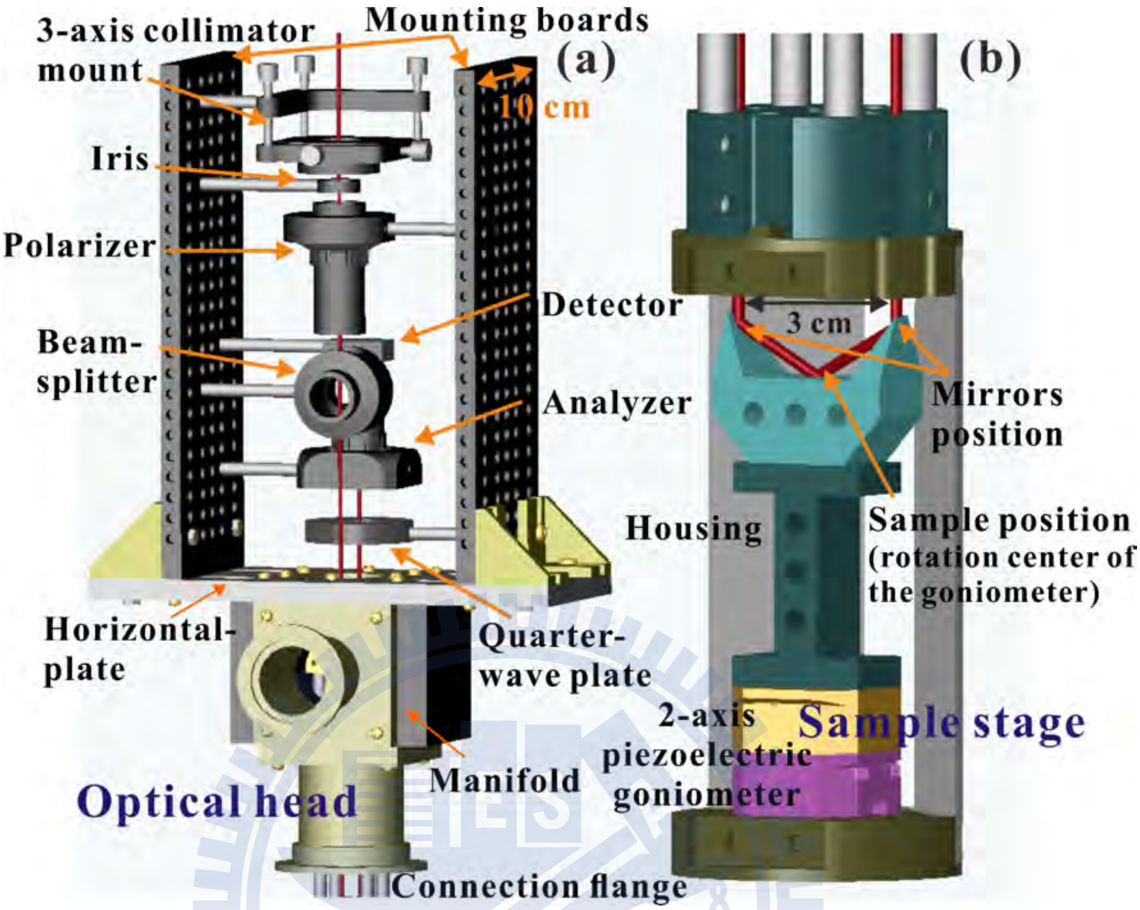

FIGURE 2.4: Design of the ellipsometer insert. (a) The optical head consists of all polarization optical elements in the room temperature environment. (b) The bottom of the insert, positioned in 4.2 K environment, includes a sample stage, a two-axis piezoelectric goniometer and a protective housing.

A thin-wall stainless steel jacket (see Fig. 2.3) with a 50 mm inner diameter is used to protect the insert and also allows the sliding seal to be used during cooling. The outer jacket must be fit to the insert by carefully tuning the 8 screws in the connection flange on the manifold to avoid any contact between them. Four springs are placed below the horizontal plate of the optical head to counterbalance the weight of the whole insert and also buffer the vibration from the dewar.

2.4 Experimental Procedure

In real measurement, two semi-insulating GaP substrates are used as the dielectric mirrors because GaP possesses a larger band gap than most III-V materials and a

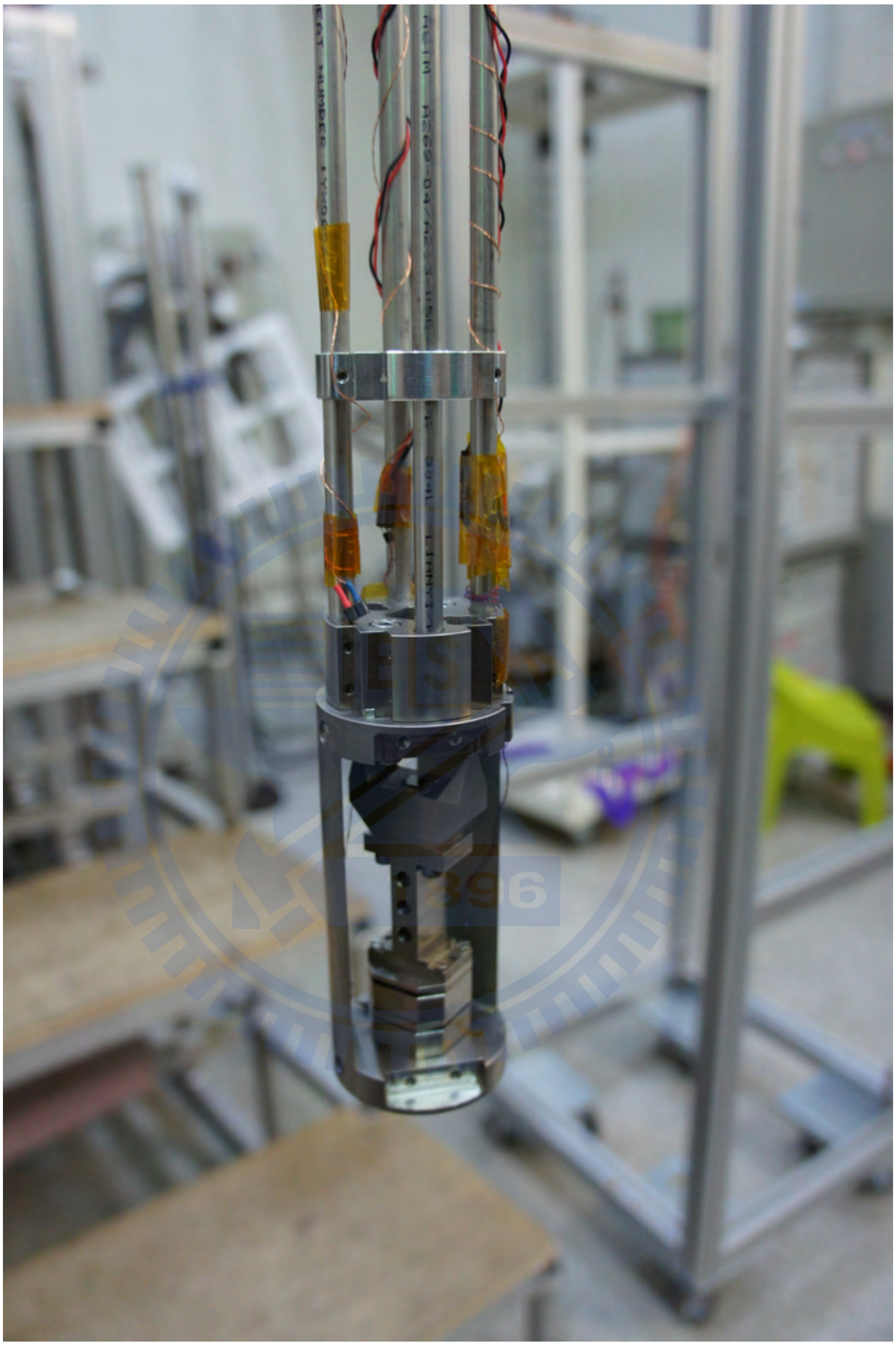

FIGURE 2.5: The first step of the experimental procedure: sample preparation and optical alignment. The alignment was done by fine tuning the 3-axis collimator mount in the optical head and the 2-axis goniometer in the bottom of the sample stage with the help of two cross-shape holes shown in the picture.

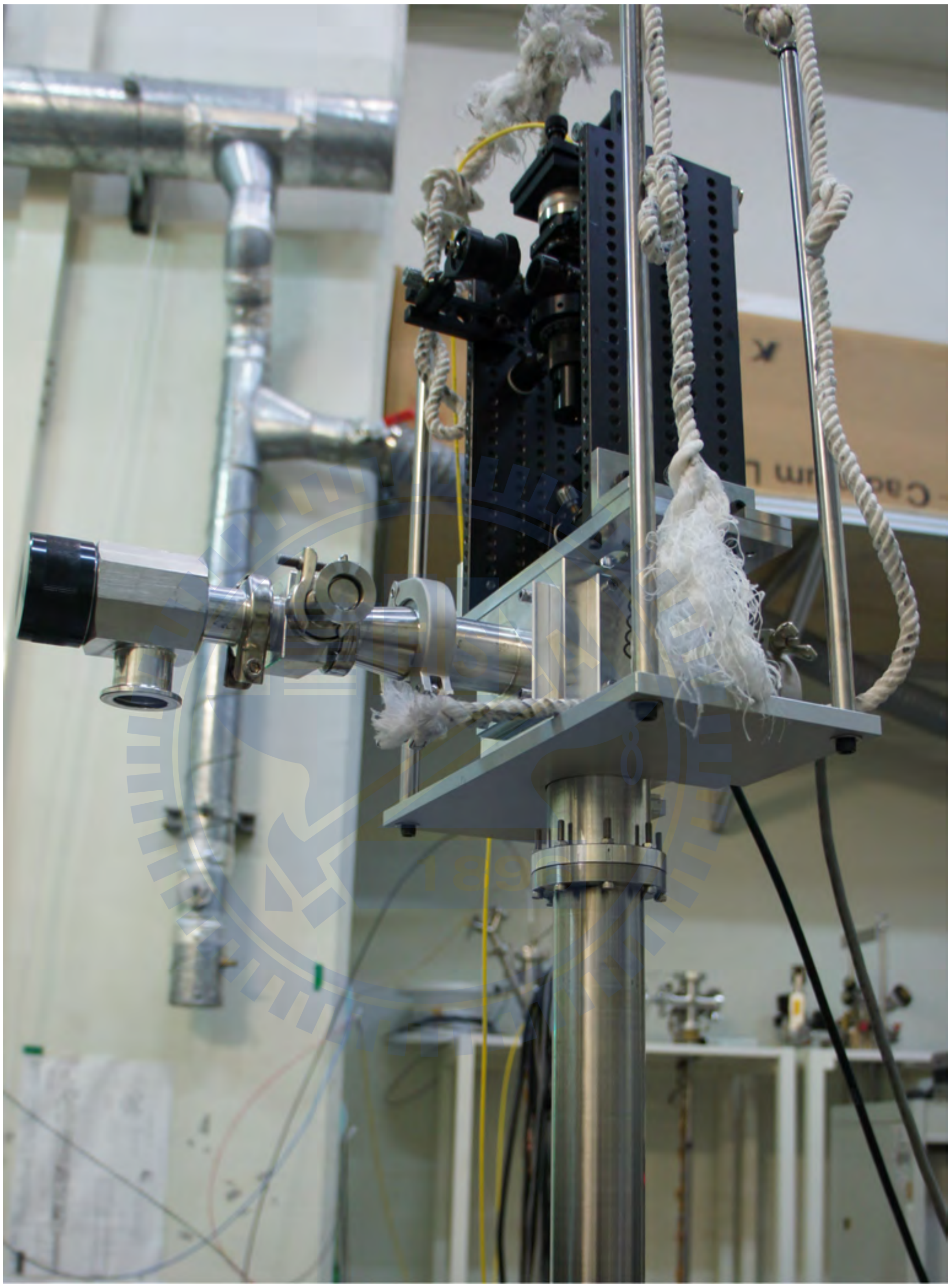

FIGURE 2.6: The second step of the experimental procedure: pumping. The outer jacket, which is a thin wall (~ 1 mm) stainless steel tube, was connection to the flange on the manifold carefully by tuning the 8 screws shown in the picture. The pressure inside the insert was pumped down to $\sim 10^{-5}$ mbar, and ~ 25 mbar Helium gas was introduced into the insert

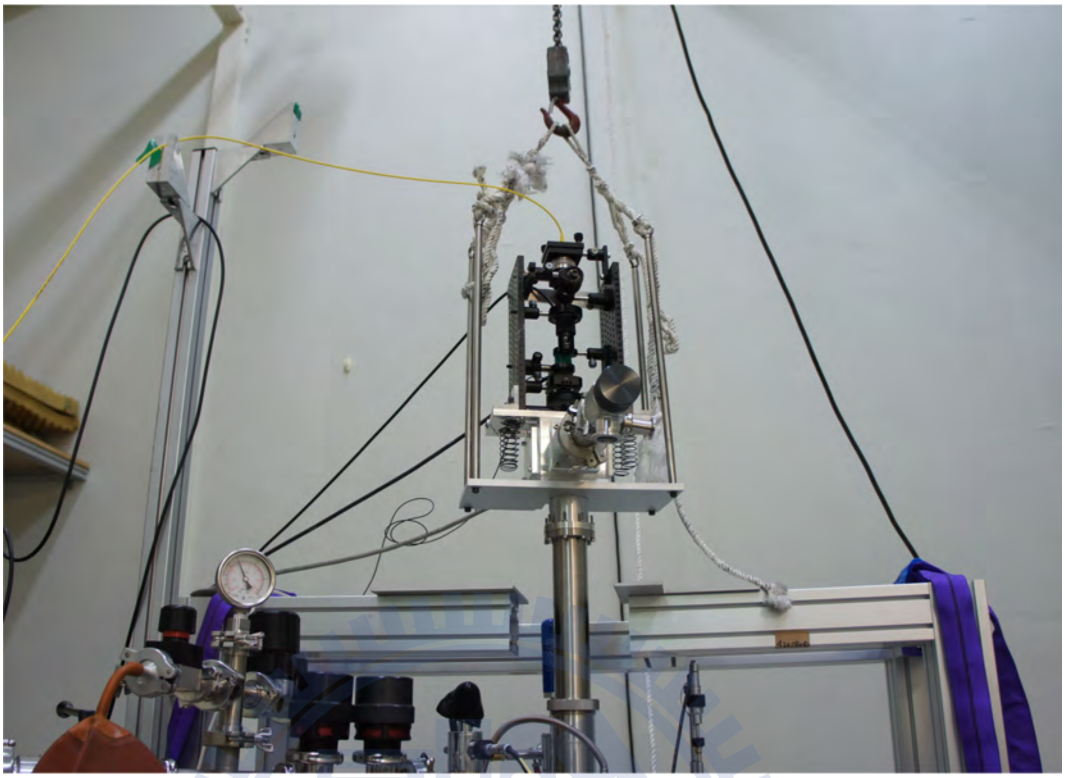

FIGURE 2.7: The third step of the experimental procedure: cooling. The insert was lowered down into the low temperature dewar slowly via a sliding seal shown in the picture.

reasonably large refractive index. In addition, no significant photo and magneto-optical response is observed for GaP under magnetic fields in the measurement band. These two GaP side mirrors and sample was mounted on the sample stage carefully by grease. To compensate the thickness difference of GaP and GaAs substrates, a glass slide was put under the GaAs substrate.

The optical alignment procedure was carried out by fine tuning the three-axis collimator mount on the top of the optical head (see Fig. 2.4 (a)) for the input light beam and the two-axis piezoelectric goniometer at the bottom of the sample stage (see Fig. 2.4 (b) and Fig. 2.5) for the reflected light beam. After the alignment, the insert was carefully sealed by the outer jacket with an O-ring and bolts and then pumped down to $\sim 10^{-5}$ mbar (Fig. 2.6). During the time of pumping, the intensity of the reflected light measured by the detector was maintained stable before and after sealed to insure no contact between the insert and the jacket[1]. Before the probe being inserted into the dewar, $\sim$ 25 mbar Helium gas was introduced into the insert for heat exchange.

---

[1] by carefully tuning the 8 screws in the connection flange (see Fig. 2.6).

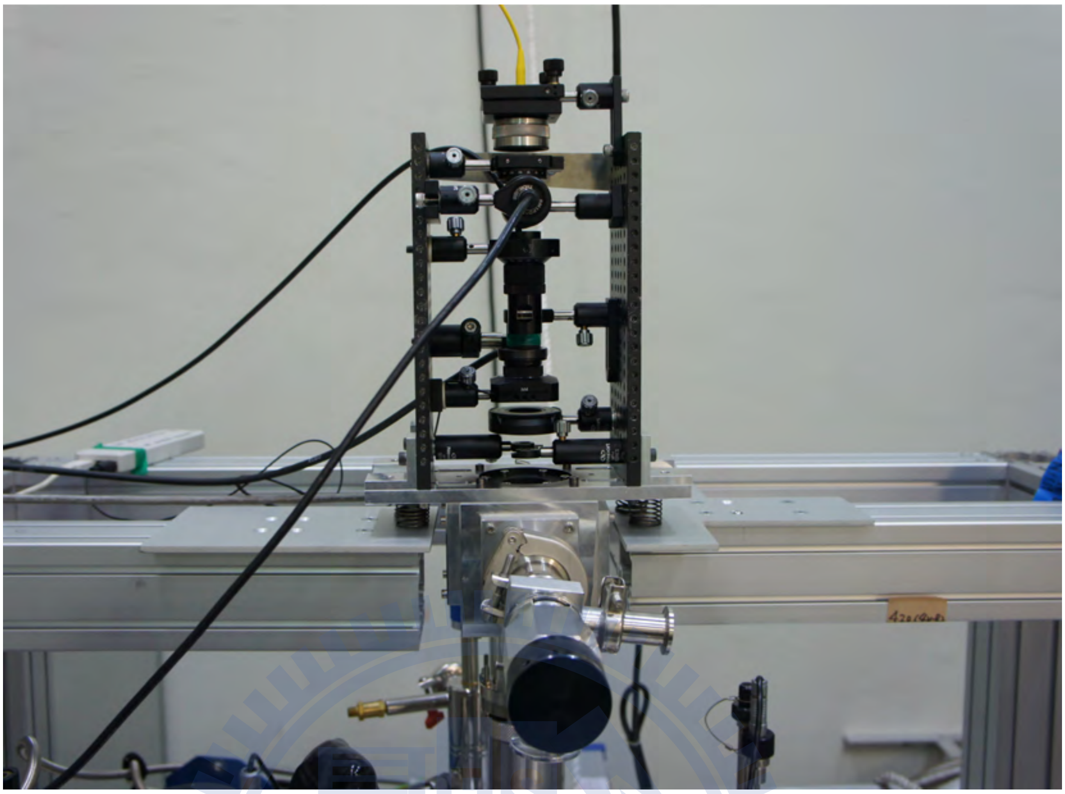

Figure 2.8: The final step of the experimental procedure: system ready.

In the cooling procedure, the insert was lowered down into the low temperature dewar slowly via a sliding seal (Fig. 2.7) and at the same time the goniometer was adjusted instantaneously to keep the reflected light signal stable. The cooling procedure need to be manipulate slowly enough to avoid rapid changes in temperature. Once the whole probe was totally inserted into the dewar and the optical head was poised on the elevated table like in Fig. 2.8, the system was idle till thermal equilibrium and was ready to perform a measurement.

2.5 Data Acquisition and Reduction

Figure 2.9 shows the data acquisition procedure. The parameters including the polarizer angle Π, the ranges and the steps of the laser wavelength, and the magnetic field are set at the beginning. The superconducting magnet can be switched to the persistent mode to save Helium consumption once the field strength reaches the setting value. The wavelength of the Ti-sapphire laser is auto-controlled by a step

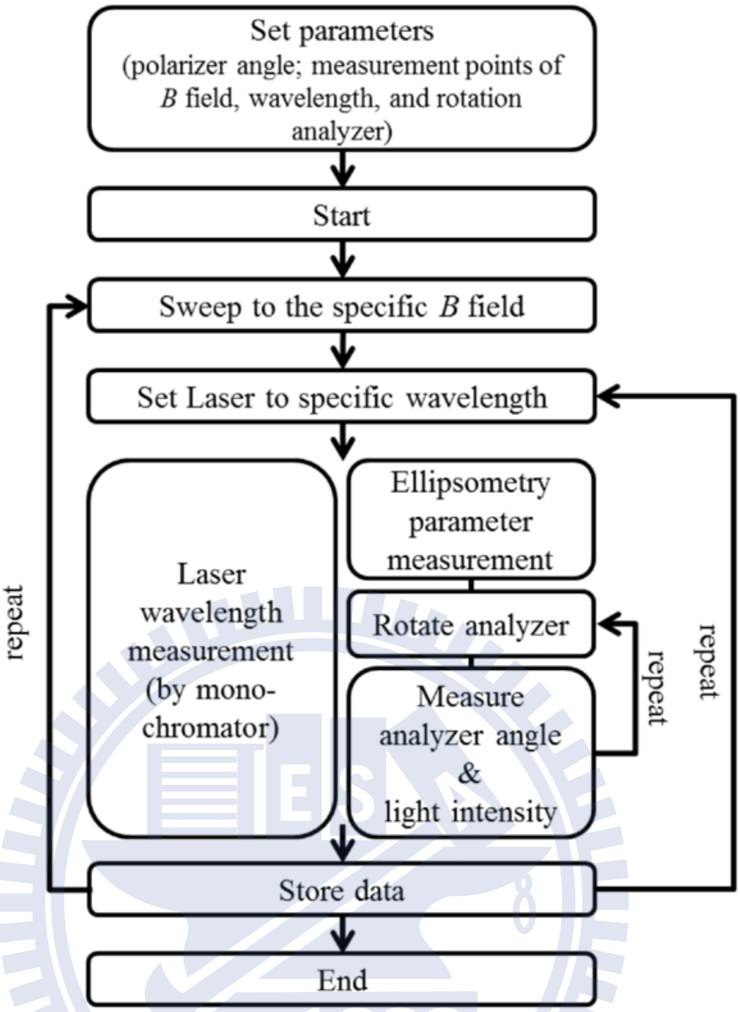

FIGURE 2.9: Flowchart of the data acquisition.

motor and is characterized by a monochromator together with the ellipsometry parameter measurement.

A polarizer-sample-rotating analyzer ellipsometry (RAE) configuration is used to measure the ellipsometry parameters. The measured light intensity can be expressed as [1–3, 53] (see Appendix A)

$$\begin{aligned} I(\Pi, A) \quad &= \quad |E_{in}|^2 \, |r_{ss}|^2 \cos^2 \Pi \, |(R_{pp} + R_{sp} \tan \Pi) \cos A \\ & \qquad + (R_{ps} R_{pp} + \tan \Pi) \sin A \, |^2, \end{aligned} \tag{2.8}$$

where E_{in} is the complex amplitude of the electric field before the polarizer. A and Π are the angles between the incident plane and the analyzer and polarizer transmission axes, respectively. This equation can be further simplified to

$$I(\Pi, A) = I_D[1 + \alpha\cos(2A) + \beta\sin(2A)], \tag{2.9a}$$

where [53]

$$\alpha = \frac{|R_{pp} + R_{sp}\tan\Pi|^2 - |R_{ps}R_{pp} + \tan\Pi|^2}{|R_{pp} + R_{sp}\tan\Pi|^2 + |R_{ps}R_{pp} + \tan\Pi|^2}, \tag{2.9b}$$

and

$$\beta = \frac{2Re\{(R_{pp} + R_{sp}\tan\Pi)(R_{sp}R_{pp} + \tan\Pi)\}}{|R_{pp} + R_{sp}\tan\Pi|^2 + |R_{ps}R_{pp} + \tan\Pi|^2}. \tag{2.9c}$$

The ellipsometry parameters depend only on α and β, and are independent of the average intensity I_D. We can obtain α and β from the Fourier expansion of $I(\Pi, A)$ [54]:

$$I_D = \frac{1}{N}\sum_{i=1}^{N} I_i; \tag{2.10a}$$

$$\alpha = \frac{2}{I_D N}\sum_{i=1}^{N} I_i\cos 2A_i; \tag{2.10b}$$

$$\beta = \frac{2}{I_D N}\sum_{i=1}^{N} I_i\sin 2A_i. \tag{2.10c}$$

where I_i is the intensity at A_i, and N is the total number of analyzer angles measured. We can use the Kerr measurement (see Appendix A) or follow the maturely developed method [16, 53] by choosing several azimuthal settings Π and using Eq. (2.9) to determine all the ellipsometry parameters R_{pp}, R_{ps}, and R_{sp}.

In some of our studies, the R_{pp} response function near the exciton transition energy at low temperatures and high magnetic fields is important. The contribution from measured R_{ps} and R_{sp} to R_{pp} spectra is small (see Appendix A) and does not influence the data fitting and interpretation shown in Chapter 5. For simplicity and clarity, we will focus on the response of R_{pp} and neglect R_{ps} and R_{sp} in the following data analysis. The Eqs. (2.9b) and (2.9c) become the same as in the standard ellipsometry situation [1–3].

$$\alpha = \frac{\tan^2\Psi_{pp} - \tan^2\Pi}{\tan^2\Psi_{pp} + \tan^2\Pi}, \tag{2.11a}$$

and

$$\beta = \frac{2\tan\Pi\tan\Psi_{pp}\cos\Delta_{pp}}{\tan^2\Psi_{pp} + \tan^2\Pi}. \tag{2.11b}$$

2.6 Error Analysis

For precise detection of the changes of R^{σ}_{pp} of the measured spectra under various external magnetic fields, to minimize the random error of the RAE technique with a multi-reflection configuration is important. It can be shown that making the light before the rotating analyzer circularly polarized gives better precision for RAE [55] (see Appendix B). Therefore, we choose a polarizer angle Π close to the measured ellipsometry angle Ψ^{eff}_{pp} to balance the intensities of p- and s-polarized components after three times of reflection.

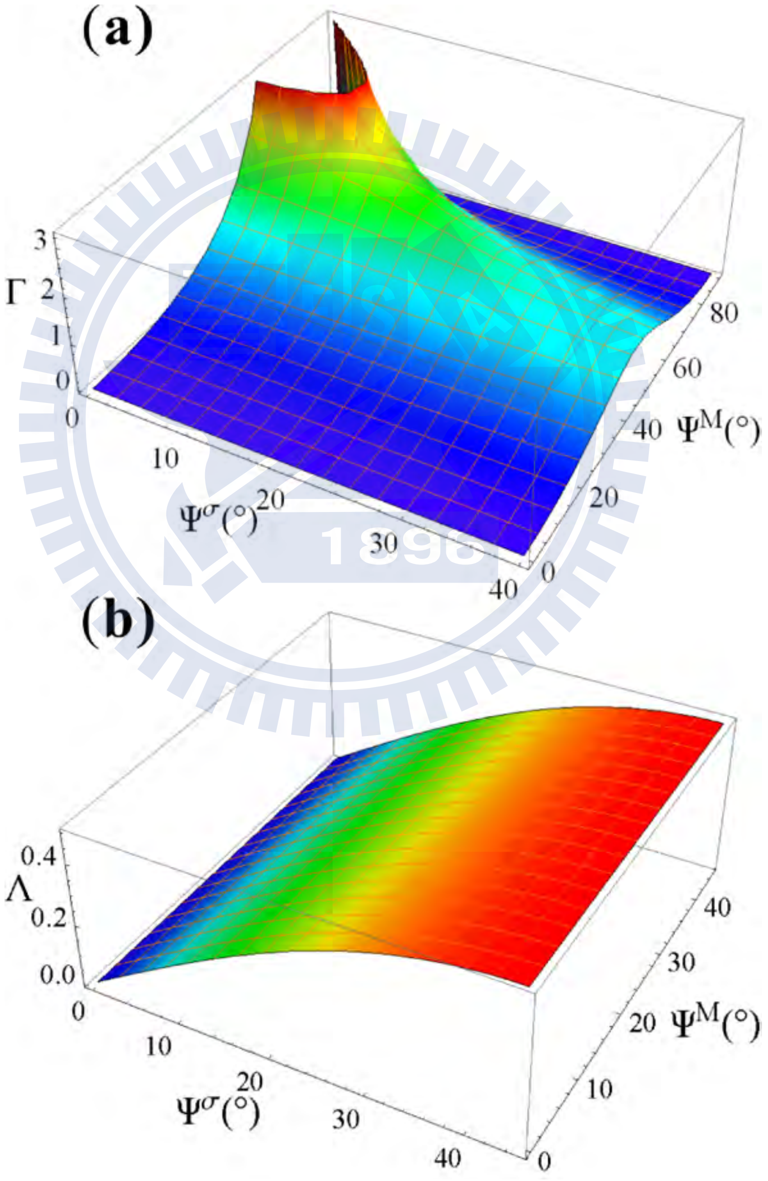

FIGURE 2.10: Γ (a) and Λ (b) (in Eqs. (2.12) and (2.14)) as a function of Ψ^{σ}_{pp} and Ψ^{M}_{pp} .

To analyze the precision of the measured result, we first find the relationship between the error of Ψ_{pp}^{eff} and the error of Ψ_{pp}^{σ} by taking the derivative of the real part of Eq. (2.7a).

$$d\Psi_{pp}^{\text{eff}} = \frac{\sec^2 \Psi_{pp}^{\sigma} \tan^2 \Psi_{pp}^{\text{M}}}{1 + \tan^2 \Psi_{pp}^{\sigma} \tan^2 \Psi_{pp}^{\text{M}}} d\Psi_{pp}^{\sigma} \equiv \Gamma d\Psi_{pp}^{\sigma}, \tag{2.12}$$

where Γ represents the coefficient that relates the two error quantities. Figure 2.10 (a) shows Γ as a function of Ψ_{pp}^{σ} and Ψ_{pp}^{M}. For a given error in the triple reflection measurement, the error in the sample's parameter can be minimized by choosing proper Ψ_{pp}^{σ} and Ψ_{pp}^{M} to maximize Γ. Thus, we can choose the mirrors once we know the dielectric constant of the sample. For example, if Ψ_{pp}^{σ} equals 22° (for GaAs at a wavelength near 800 nm and a 60° incident angle), we can choose Ψ_{pp}^{M} close to 45° (see Fig. 2.10(a)) to minimize the error ($d\Psi_{pp}^{\sigma}$) of the deduced sample parameter.

However, the error in the triple reflection measurement, $d\Psi_{pp}^{\text{eff}}$, depends on the polarizer angle Π and is related to the error in the Fourier component α by (see Appendix B)

$$d\Psi_{pp}^{\text{eff}} = [\frac{\cos^2 \Psi_{pp}^{\text{eff}} (\tan^2 \Pi + \tan^2 \Psi_{pp}^{\text{eff}})^2}{4 \tan \Psi_{pp}^{\text{eff}} \tan^2 \Pi}] d\alpha. \tag{2.13}$$

By using this relationship and choosing $\Pi = \Psi_{pp}^{\text{eff}}$ for best precision, Eq. (2.12) can be rewritten as

$$d\Psi_{pp}^{\sigma} = \frac{\tan^2 \Psi_{pp}^{\text{M}} \tan \Psi_{pp}^{\sigma}}{\Gamma[1 + (\tan^2 \Psi_{pp}^{\text{M}} \tan \Psi_{pp}^{\sigma})^2]} d\alpha \equiv \Lambda d\alpha. \tag{2.14}$$

The error $d\Psi_{pp}^{\sigma}$ is now related to the error in the Fourier coefficient $d\alpha$ (see Appendix B) by a factor Λ, which depends on the parameter Γ and the Ψ_{pp} values of the mirrors and the sample. Figure 2.10 (b) shows the factor Λ as a function of Ψ_{pp}^{σ} and Ψ_{pp}^{M}. For a typical sample (ex. $\Psi_{pp}^{\text{GaAs}} \sim 22^\circ$), Λ is a slowly varying function of Ψ_{pp}^{M}. The precision is not sensitive to the choice of a mirror when the polarizer angle Π is chosen close to Ψ_{pp}^{eff}.

The precision of the phase difference Δ_{pp} can be shown as (see Eq. (B.1b) in Appendix B)

$$d\Delta_{pp}^{\text{eff}} = \frac{1}{\sin \Delta_{pp}^{\text{eff}} (1 - \alpha^2)^{3/2}} [(\alpha^2 - 1) d\beta - (\alpha\beta) d\alpha]. \tag{2.15}$$

It can be improved by adding a quarter-wave plate in front of the analyzer especially for measuring dielectric samples whose Δ_{pp} is close to 0° or 180°. Then, Eq. (2.11b) becomes

$$\sin \Delta_{pp}^{\text{eff}} = -\text{sgn}(P)\frac{\beta}{\sqrt{1-\alpha^2}} \tag{2.16}$$

for the fast axis of a quarter-wave plate parallel to the incident plane. From Eq. (2.16), the sign of Δ_{pp} can be distinguished by adding a quarter-wave plate in front of a rotating analyzer. This is important especially for the measurements with photon energy close to the exciton or polariton states (see Chapter 3).

To test the performance of this system at low temperature, we have taken data for more than 200 periods of rotations of the analyzer. The resulted standard deviations (shown in Fig. 2.11) of Ψ_{pp}^{eff} and Δ_{pp}^{eff} are 0.04° and 0.3°(while Ψ_{pp}^{σ} and Δ_{pp}^{σ} are $\sim 0.25^\circ$ and 0.3°) for $\Psi_{pp}^{\text{eff}} = 3.05^\circ$, $\Delta_{pp}^{\text{eff}} = 100.2^\circ$, and $\Pi = 4^\circ$. We can then use the standard deviations ($d\Psi_{pp}^{\text{eff}}$ and $d\Delta_{pp}^{\text{eff}}$) and the known parameters (α, β and dA) to obtain the intensity fluctuation δ defined as dI/I_D in Appendix B) using the coupled coupled Eqs. (B.3a) and (B.3b). We found that the contribution of δ is larger than that of the error of the analyzer angle dA and the residue from the asymmetry of A_i in real measurements. It can be attributed to the mechanical vibration through such a long framework of the insert. Although the random errors are not as small as that of conventional ellipsometers, the precision of this system is good enough for many of the proposed studies [4–8], and more importantly, it can operate at much higher magnetic fields than the ones reported previously.

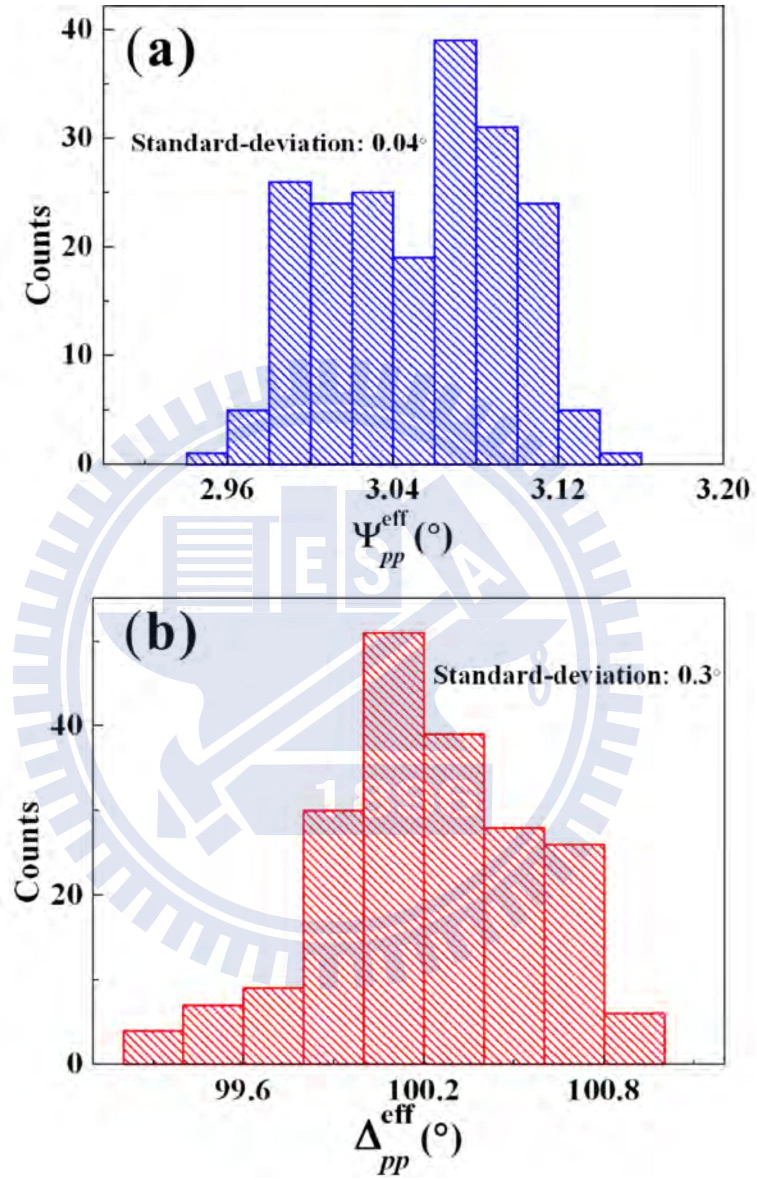

FIGURE 2.11: Histograms of Ψ_{pp}^{eff} and Δ_{pp}^{eff} shown as bar charts. (a) The standard deviation of Ψ_{pp}^{eff} is 0.04°at average of 3.05° (b) The standard deviation of Δ_{pp}^{eff} is 0.3° at average of 100.2°.

Chapter 3

Results

We have used this self-designed ellipsometer to measure the samples including a semi-insulating GaAs (001) wafer and a 1-μm un-doped MBE grown layer on the substrate (Fig. 3.1). The results of them will shown in this chapter.

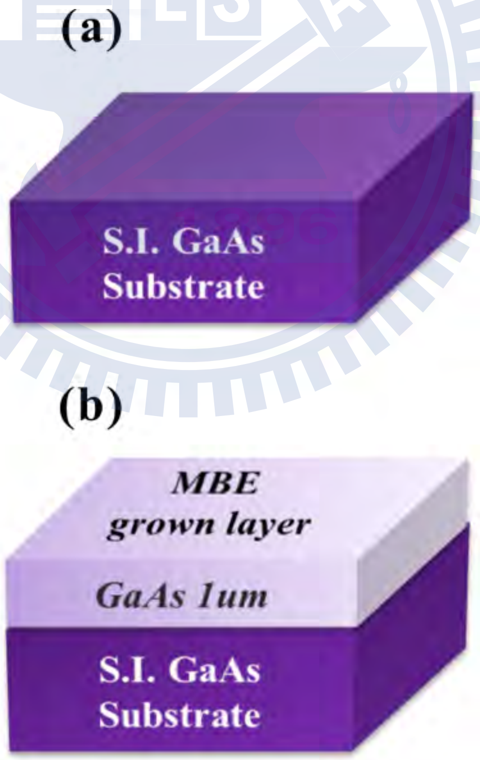

FIGURE 3.1: Sample structures. (a) Semi-insulating (S.I.) GaAs wafer ($\sim$ 350 μm); and (b) MBE grown 1μm un-doped GaAs layer on S.I. GaAs wafer ($\sim$ 350 μm).

3.1 GaAs Substrate

The Ψ^{σ}_{pp} and Δ^{σ}_{pp} spectra of GaAs substrate from 1.514 to 1.532 eV at 4.2 K are shown in Figs. 3.2(a) and 3.2(b) respectively for different magnetic fields up to 14 Tesla. In Fig. 3.2(b), the asymmetric curves in Δ^{σ}_{pp} spectra across the 180° line indicate that the phase differences change sign from right-handed (negative helicity) to left-handed (positive helicity) polarizations [56] near the transitions. The raw RAE data with a quarter-wave plate in front of the rotating analyzer at wavelength 812.12 nm and 812.4 nm (marked by the dashed cycles in Fig. 3.2(b)) are plotted in a polar coordinate in Fig 3.2(c). The sign change of Δ^{σ}_{pp} can be determined from the orientations of the long-axes (the dash lines) of the polar curves located in different quadrants (see Appendix C).

Semi-insulating GaAs substrates, because of the high defect density, usually have broadened spectra due to a large damping. Thus it is difficult to observe the fine structure of level splitting at high fields and even the signal from the zero-field exciton becomes very weak. In comparison, we show in Fig. 3.3 the ellipsometric measurement of a high-quality GaAs layer grown by molecular beam epitaxy (MBE). The layer, grown on a (100) semi-insulating GaAs substrate, was undoped and had a thickness of 1-μm. Unlike what was seen from the substrate alone, the result from the epilayer shows discernible features in the ellipsometry spectra even at zero magnetic field as shown in Fig. 3.3, and some of the features exhibit intriguing behaviors when high magnetic fields are applied. These features, which have not been reported before, can now be studied and observed using our ellipsometry system. The data will be showed in the next section.

3.2 GaAs 1-μm Epitaxial Layer

Figure 3.4 (a) shows the measured phase difference Δ and the amplitude ratio Ψ (inset) of the sample (to distinguish from the results of the GaAs substrate and for convenience, we drop the superscript "σ "and subscript "pp " in the following) at 0 T and 1 T. Fine structures with multiple peaks and dips are observed in the spectra and become apparent when the magnetic field is applied. In Fig 3.4 (a), similar to the results of the GaAs substrate, the measured curves in the Δ spectra across 180° (dash-line) indicates the sign change of Δ. The raw RAE data measured at 1 T

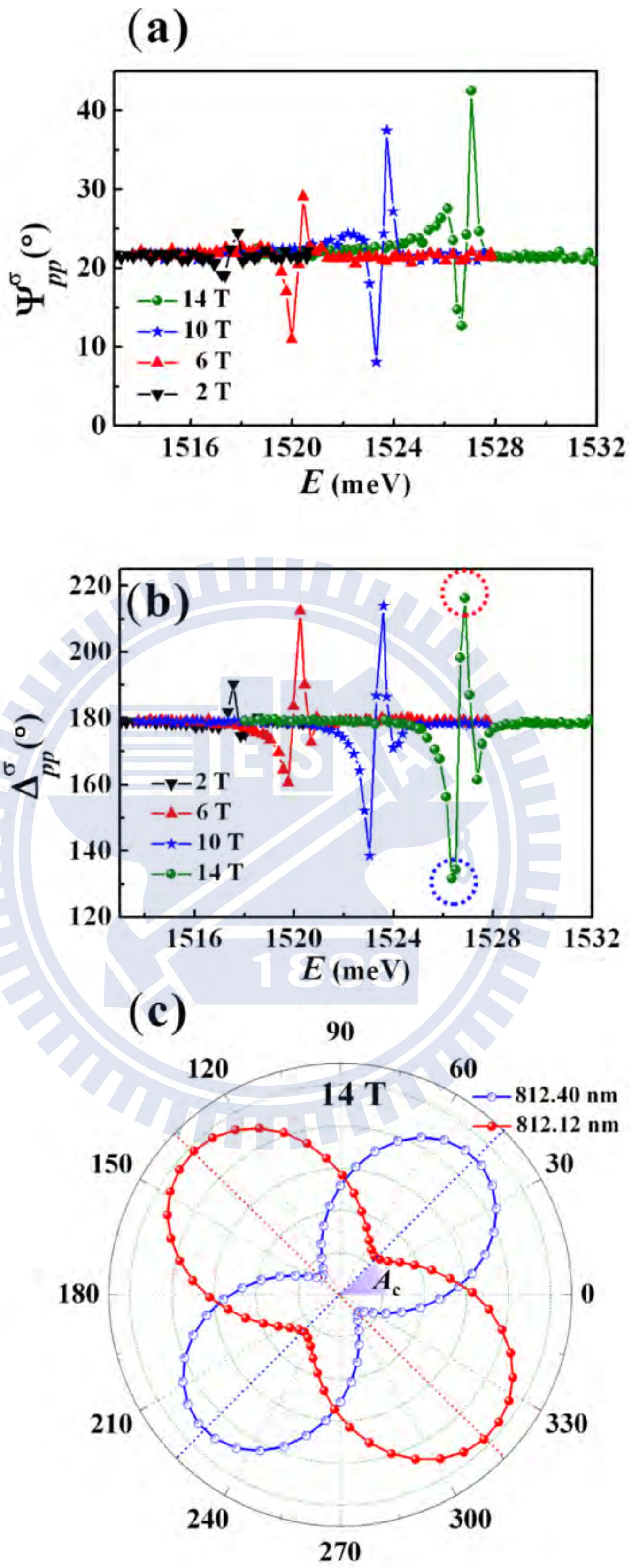

FIGURE 3.2: Spectra of (a) Ψ^{σ}_{pp} and (b) Δ^{σ}_{pp} of intrinsic GaAs substrate for different magnetic fields at 4.2 K. (c) Intensity versus analyzer angle at 812.12 nm (solid points) and 812.40 nm (open circles) in polar coordinates at 14 T. The angle A_c is defined in Appendix C.

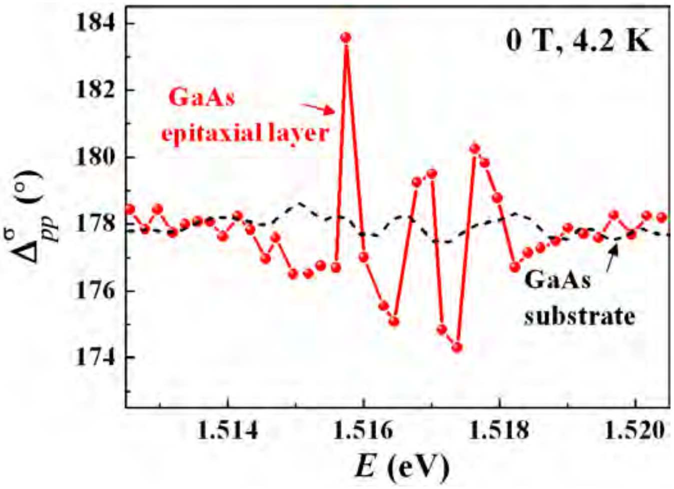

FIGURE 3.3: Comparison of Δ_{pp}^{σ} spectra of GaAs substrate (dash-line) and GaAs epitaxial layer (solid-line) grown by MBE at zero magnetic field.

with the fast axis of the quarter-wave plate parallel to the incident plane at energies 1.5157 eV and 1.516 eV are showed in polar plots in Fig 3.4 (b). The orientation of the long-axes (dot-lines) of the two elliptical intensity distributions located in different quadrants represents that the handedness of the two polarisation states are different (Appendix C). The polarisation states turn from elliptical clockwise to counterclockwise for the energy approaching from 1.5157 eV to 1.516 eV in the Δ spectrum of 1 T.

When magnetic field is increased ($\geq$ 6 T), more dips and peaks appear in the spectra. We show, for instance, the spectra of Ψ and Δ at 14 T in Fig. 3.5. It shows the corresponding property of the real (Ψ) and imaginary (Δ) spectra, which ensures the reliability of the measurement. We denote appropriately the dips as A, B, C, and D in the spectrum Δ the order from lower energy to higher energy.

To observe how the fine structures evolve with varied magnetic fields, we show the spectra of Δ with the magnetic field varied from 2 to 14 T in Fig. 3.6. The spectra are shifted in energy to exclude the diamagnetic shift differences. While the dips B, C, and D are observed starting from 0 T, the dip A appears only above 6 T. The separation of the dips A and B becomes larger when the magnetic field increases, but the dips C and D become closer first and then nearly maintain a certain distance when the magnetic field increases.

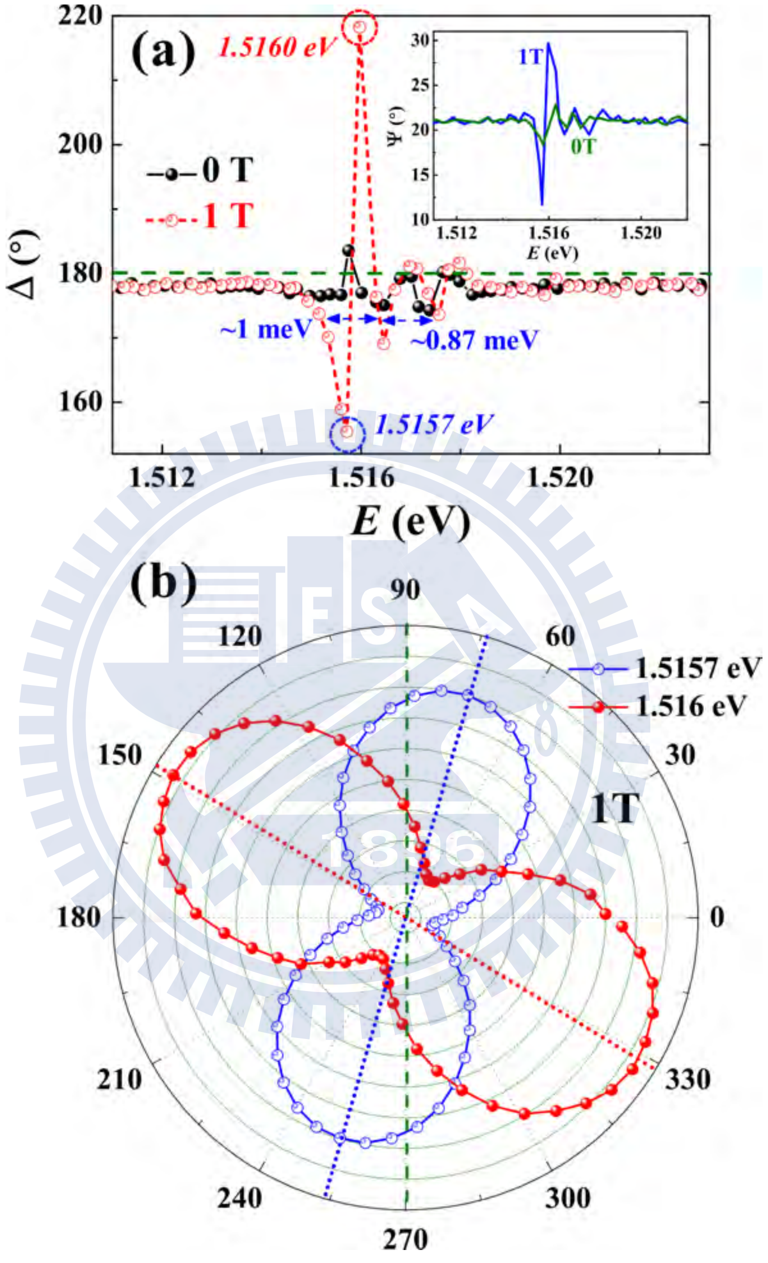

FIGURE 3.4: (a) Spectra of Δ and Ψ (the inset) of GaAs epitaxial layer for magnetic fields of 0 T and 1 T at 4.2 K. (b) The raw data of the rotating-analyser ellipsometry measurements in polar coordinates at 1 T, 4.2 K for the energies 1.5157 eV (open circles) and 1.5160 eV (solid points).

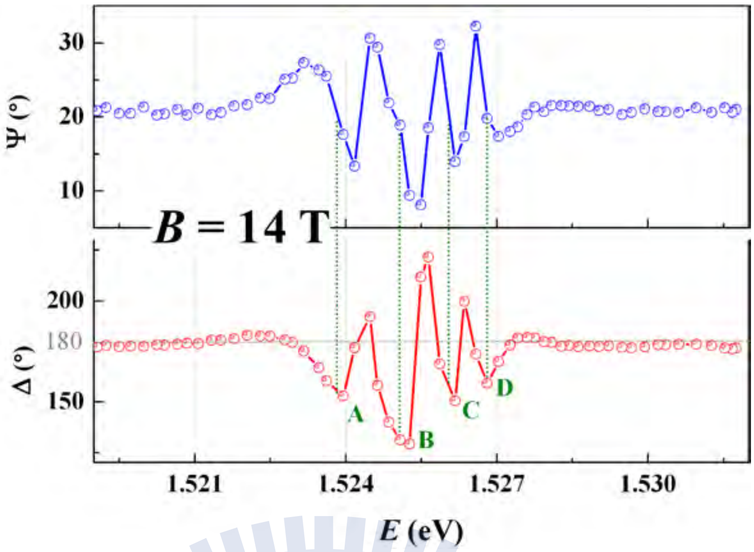

FIGURE 3.5: Spectra of Ψ and Δ at 14 T, 4.2 K. Four dips are denoted as A, B, C, and D in the spectrum of Δ. The four dot-lines show the corresponding property of the spectra Ψ and Δ.

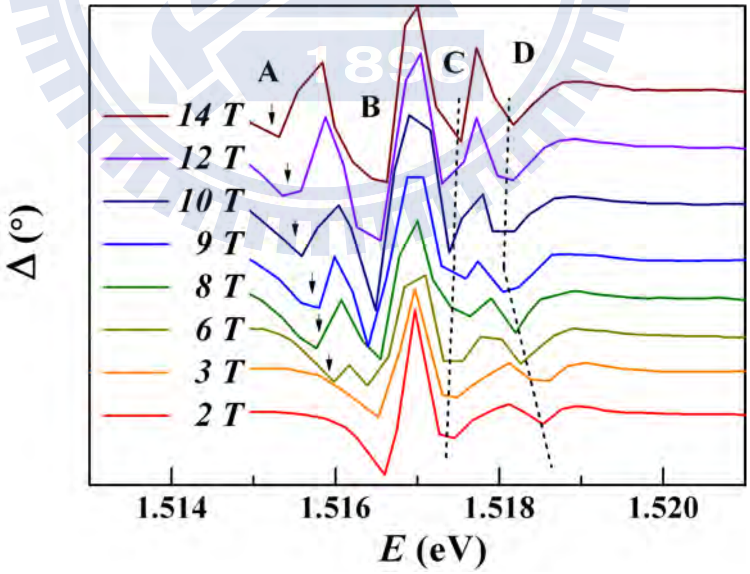

FIGURE 3.6: Spectra of Δ for magnetic fields varied from 2 to 14 T at 4.2 K. The spectra are shifted to exclude the differences of the diamagnetic shift. The arrows represent the increasing separation between the dips A and B, and the dash-lines show the change of the dips C and D with magnetic fields.

Chapter 4

Theory & Models

4.1 Direct-Excitons in Semiconductor

4.1.1 Multi-Band Theory

In this section, we review the direct-exciton model constructed by Baldereschi and Lipari [57] as the band mixing effect are accounted. The Hamiltonian (neglecting the CM motion and the electron spin) can be written as:

$$H_{ex}(\mathbf{p}) = H^{LK}_{6\times 6}(\mathbf{p}) + [E_0 + \frac{p^2}{2m_e} - \frac{e^2}{4\pi\varepsilon_b r}]\mathbf{I}, \tag{4.1}$$

where $H^{LK}_{6\times 6}$ describe the hole kinetic energy near k=0 with the relative electron-hole momentum $\mathbf{p}$, and r is the distance of a electron and a hole. The second part of Eq. (4.1) is a 6×6 diagonal matrix including the band-edge energy E_0, the electron kinetic energy and the Coulomb interaction. For the diamond structure, Eq. (4.1) can be represented in a matrix [57]

$$\begin{pmatrix} P+Q & L^\dagger & M & 0 & (i/\sqrt{2})L & -(i/\sqrt{2})M \\ L^\dagger & P-Q & 0 & M & -(i/\sqrt{2})Q & i(\sqrt{3/2})L \\ M^\dagger & 0 & P-Q & -L & -i(\sqrt{3/2})L^\dagger & -(i/\sqrt{2})Q \\ 0 & M^\dagger & -L^\dagger & P+Q & -(i/\sqrt{2})M^\dagger & -(i/\sqrt{2})L^\dagger \\ -(i/\sqrt{2})L^\dagger & (i/\sqrt{2})Q & i(\sqrt{3/2})L & (i/\sqrt{2})M & P+\Delta_{so} & 0 \\ (i/\sqrt{2})M^\dagger & -i(\sqrt{3/2})L^\dagger & (i/\sqrt{2})Q & (i/\sqrt{2})L & 0 & P+\Delta_{so} \end{pmatrix}, \tag{4.2}$$

and can be separated as

$$H_{ex}(\mathbf{p}) = H_s + H_d, \tag{4.3}$$

where

$$H_s = \begin{pmatrix} P & 0 & 0 & 0 & 0 & 0 \\ 0 & P & 0 & 0 & 0 & 0 \\ 0 & 0 & P & 0 & 0 & 0 \\ 0 & 0 & 0 & P & 0 & 0 \\ 0 & 0 & 0 & 0 & P+\Delta_{so} & 0 \\ 0 & 0 & 0 & 0 & 0 & P+\Delta_{so} \end{pmatrix}, \tag{4.4a}$$

and

$$H_d = \begin{pmatrix} Q & L^\dagger & M & 0 & (i/\sqrt{2})L & -(i/\sqrt{2})M \\ L^\dagger & -Q & 0 & M & -(i/\sqrt{2})Q & i(\sqrt{3/2})L \\ M^\dagger & 0 & -Q & -L & -i(\sqrt{3/2})L^\dagger & -(i/\sqrt{2})Q \\ 0 & M^\dagger & -L^\dagger & Q & -(i/\sqrt{2})M^\dagger & -(i/\sqrt{2})L^\dagger \\ -(i/\sqrt{2})L^\dagger & (i/\sqrt{2})Q & i(\sqrt{3/2})L & (i/\sqrt{2})M & 0 & 0 \\ (i/\sqrt{2})M^\dagger & -i(\sqrt{3/2})L^\dagger & (i/\sqrt{2})Q & (i/\sqrt{2})L & 0 & 0 \end{pmatrix}, \tag{4.4b}$$

with Δ_{so} being the spin-orbit splitting, and the coefficients

$$P = \frac{p^2}{2\mu} - \frac{e^2}{4\pi\varepsilon_b r}\ (s\text{-like}), \tag{4.5a}$$

$$Q = \frac{p_x^2 + p_y^2 - 2p_z^2}{2\mu_1}\ (d\text{-like}), \tag{4.5b}$$

$$L = -i\frac{(p_x - ip_y)p_z}{2\mu_2}\ (d\text{-like}), \tag{4.5c}$$

$$M = \sqrt{3}\frac{p_x^2 - p_y^2}{2\mu_1} - i\frac{p_x p_y}{2\mu_2}\ (d\text{-like}). \tag{4.5d}$$

The masses μ, μ_1, and μ_2 are related to the Luttinger parameters $(\gamma_1, \gamma_2, \gamma_3)$ as follows

$$\frac{1}{\mu} = \frac{1}{m_e} + \frac{\gamma_1}{m_0}, \tag{4.6a}$$

$$\frac{1}{\mu_1} = \frac{\gamma_2}{m_0}, \tag{4.6b}$$

$$\frac{1}{\mu_2} = 2\sqrt{3}\frac{\gamma_3}{m_0}, \tag{4.6c}$$

where m_0 is the free-electron mass. Equations (4.4a) and (4.4b) represent the exciton Coulomb interaction formed by the electron-isotropic hole and the electron-anisotropic hole respectively. The separation of the full Hamiltonian to the s-like and d-like parts renders the perturbation of it being possible. Because μ is much smaller than μ_1 and μ_2 ($m_e \ll m_0$), equation (4.5a) is more important than Eqs. (4.5b), (4.5c), and (4.5d). Therefore, we can treat the anisotropic part H_d as a perturbation of the hydrogen-atom-like part H_s. This represents that the exciton is just like a hydrogen atom with a small distortion. For Zinc-Blende structures, the Hamiltonian (4.3) should be added another contribution from inversion-asymmetry. However, this effect is small and negligible.

4.1.2 One-Band Model

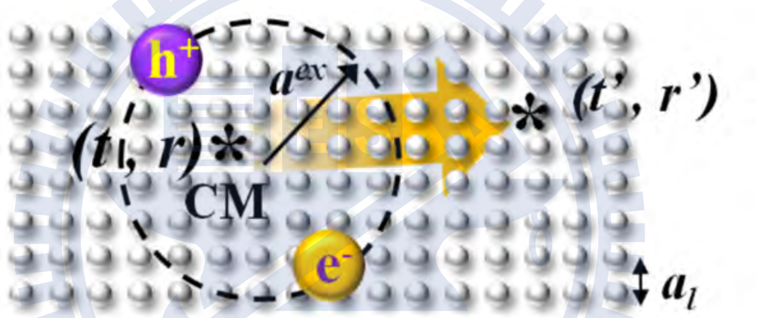

FIGURE 4.1: Diagram of a exciton propagating in semiconductor. It moves from r to r' during the time t to t'.

From 4.1.1, we know that the exciton is like a hydrogen atom with a small distortion (Fig. 4.1). Hence, in this subsection, we use one-band effective mass Schrödinger equation

$$[E_0 + \frac{p_e^2}{2m_e} + \frac{p_h^2}{2m_h} - \frac{e^2}{4\pi\varepsilon_b\,|\mathbf{r}_e - \mathbf{r}_h|}]\psi(\mathbf{r}_e, \mathbf{r}_h) = E\psi(\mathbf{r}_e, \mathbf{r}_h), \tag{4.7}$$

as a good approximation to describe the exciton. Where $\mathbf{r}_e$, $\mathbf{r}_h$, p_e, p_h, m_h, E_0, E and $\psi(\mathbf{r}_e, \mathbf{r}_h)$ are the electron coordinate, hole coordinate, electron momentum, hole momentum, hole effective mass, band edge energy, exciton energy, and exciton (envelope) wave function, respectively. Equation (4.7) can be rewritten as

$$[\frac{P^2}{2M_{ex}} + \frac{p^2}{2\mu} - \frac{e^2}{4\pi\varepsilon_b r}]\psi(\mathbf{r}, \mathbf{R}) = (E - E_0)\psi(\mathbf{r}, \mathbf{R}), \tag{4.8}$$

using the relative coordinate

$$\mathbf{r} = \mathbf{r}_e - \mathbf{r}_h, \tag{4.9a}$$

and the center-of-mass coordinate

$$\mathbf{R} = \frac{m_e\mathbf{r}_e + m_h\mathbf{r}_h}{M_{ex}}, \tag{4.9b}$$

where

$$\mathbf{P} = -i\hbar\nabla_{\mathbf{R}}, \tag{4.9c}$$

$$\mathbf{p} = -i\hbar\nabla_{\mathbf{r}}, \tag{4.9d}$$

$$M_{ex} = (m_e + m_h), \tag{4.9e}$$

$$\mu = \frac{m_e m_h}{M_{ex}}, \tag{4.9f}$$

The exciton wave function can be found from Eq. (4.8), which is independent of $\mathbf{R}$, and written in the form

$$\psi(\mathbf{r}, \mathbf{R}) = \exp(i\mathbf{q}_{ex} \cdot \mathbf{R})\phi(\mathbf{r}), \tag{4.10}$$

where $\mathbf{q}_{ex} = \mathbf{P}/\hbar$. Substituting Eq. (4.10) into Eq. (4.8) yields a hydrogen-atom-like equation [1]

$$[\frac{p^2}{2\mu} - \frac{e^2}{4\pi\varepsilon_b r}]\phi(\mathbf{r}) = (E - E_0 - \frac{\hbar^2 q_{ex}^2}{2M_{ex}})\phi(\mathbf{r}), \tag{4.11}$$

whose energy levels are

$$E_n = -\frac{R^{ex}}{n^2}, \tag{4.12a}$$

where the exciton Rydberg energy

$$R^{ex} = \frac{\mu e^4}{2(4\pi\varepsilon_b)^2\hbar^2}, \tag{4.12b}$$

and the exciton Bohr radius

$$a^{ex} = \frac{4\pi\varepsilon_b\hbar^2}{\mu e^2}. \tag{4.12c}$$

To define the relative strength of the Coulombic and magnetic terms, we define

$$\begin{aligned} \gamma &= \frac{\hbar\omega_c}{2R^{ex}} \\ &= \frac{\hbar e B}{2R^{ex}\mu}. \end{aligned} \tag{4.12d}$$

---

[1] Actually, just like the diagonal terms of H_s in Eq. (4.5a.)

Thus, the exciton energy

$$\begin{aligned} E &= E_0 + E_n + \frac{\hbar^2 q_{ex}^2}{2M_{ex}}, \text{ or} && (4.12\text{e}) \\ \hbar\omega_0 &= \hbar\omega_T + \frac{\hbar^2 q_{ex}^2}{2M_{ex}}, && (4.12\text{f}) \end{aligned}$$

where $\hbar\omega_T$ is the energy to create a motionless exciton.

4.2 Excitons in Magnetic Fields

4.2.1 One-Band Excitons in Magnetic Fields

We first consider the simple one-band excitons in a magnetic field [58], equation (4.7) becomes

$$[E_0 + \frac{(\boldsymbol{p}_e - e\boldsymbol{A})^2}{2m_e} + \frac{(\boldsymbol{p}_h - e\boldsymbol{A})^2}{2m_h} - \frac{e^2}{4\pi\varepsilon_b\left|\mathbf{r}_e - \mathbf{r}_h\right|}]\psi(\mathbf{r}_e, \mathbf{r}_h) = E\psi(\mathbf{r}_e, \mathbf{r}_h), \quad (4.13)$$

where $\boldsymbol{A}$ is the vector potential. Using the relative and CM coordinates, Eq. (4.13) can be rewritten as

$$\begin{aligned} [\frac{p^2}{2\mu} &+ e(\frac{1}{m_h} - \frac{1}{m_e})\boldsymbol{A}\cdot\boldsymbol{p} + \frac{e^2}{2\mu}\boldsymbol{A}\cdot\boldsymbol{A} - \frac{e^2}{4\pi\varepsilon_b r} && (4.14) \\ &- \frac{2e\hbar}{M_{ex}}\mathbf{q}_{ex}\cdot\boldsymbol{A} + \frac{P^2}{2M_{ex}}]\phi(\mathbf{r}) = (E - E_0)\phi(\mathbf{r}). \end{aligned}$$

When the Lorentz gauge

$$\boldsymbol{A} = \frac{1}{2}\boldsymbol{B}\times\mathbf{r} \quad (4.15)$$

is applied, Eq. (4.14) becomes

$$\begin{aligned} [\frac{p^2}{2\mu} &+ \frac{e}{2}(\frac{1}{m_h} - \frac{1}{m_e})\boldsymbol{B}\cdot\boldsymbol{L} + \frac{e^2}{8\mu}\left|\boldsymbol{B}\times\mathbf{r}\right|^2 - \frac{e^2}{4\pi\varepsilon_b r} && (4.16) \\ &- \frac{e\hbar}{M_{ex}}(\mathbf{q}_{ex}\times\boldsymbol{B}\cdot\mathbf{r}) + \frac{P^2}{2M_{ex}}]\phi(\mathbf{r}) = (E - E_0)\phi(\mathbf{r}), \end{aligned}$$

where $\boldsymbol{L}$ is the angular momentum, the second term is the Zeeman term[2], the third term is the diamagnetic operator, the fifth and sixth terms depend upon the

---

[2] Electron and hole spins are not considered here, their contribution to the Zeeman term is $g_e\mu_B\boldsymbol{S}_e\cdot\boldsymbol{B}+g_h\mu_B\boldsymbol{S}_h\cdot\boldsymbol{B}$.

exciton motion and are usually neglected due to their small values. If only the s-states are considered, the Eq. (4.16) becomes

$$[\frac{p^2}{2\mu} - \frac{e^2}{4\pi\varepsilon_b r} + \frac{e^2B^2}{8\mu}(x^2+y^2)]\phi(\mathbf{r}) = (E-E_0)\phi(\mathbf{r}), \tag{4.17}$$

for B applied parallel to the z direction.

4.2.2 Multi-Band Excitons in Magnetic Fields

For considering the band mixing of excitons in magnetic fields, we discuss the theory developed by K. Cho *et al.* [59] for zinc-blend crystals in this subsection. The effective Hamiltonian in a magnetic field was obtained by considering the symmetry of invariant terms [59] and was compared to the result obtained by perturbation method done by Altarelli and Lipari [60]. The Hamiltonian is given by [59]

$$\begin{aligned} H \;=\; & E_b + \widetilde{\Delta}_1\mathbf{J}\cdot\vec{\sigma} + \widetilde{\Delta}_2(\sigma_x J_x^3 + \sigma_y J_y^3 + \sigma_z J_z^3) + \widetilde{g}_c\mu_B\vec{\sigma}\cdot\mathbf{B} \\ & -2\mu_B[\widetilde{\kappa}\mathbf{J}\cdot\mathbf{B} + \widetilde{q}(B_xJ_x^3 + B_yJ_y^3 + B_zJ_z^3)] \\ & +(\frac{ea^{ex}}{2c})^2\frac{1}{\mu_0}[c_1B^2 + c_2(\mathbf{J}\cdot\mathbf{B})^2 + c_3(B_xB_y\{J_xJ_y\} + B_yB_z\{J_yJ_z\} + B_zB_x\{J_zJ_x\})], \end{aligned} \tag{4.18}$$

where $\vec{\sigma}$ and $\mathbf{J}$ are the effective spin operator for the electron and hole respectively, $\{J_xJ_y\} = (J_xJ_y + J_yJ_x)/2$ etc., the axes x, y, z refer to three $\langle 001\rangle$ axes of the crystal, and the nine parameters: $E_b, \widetilde{\Delta}_1, \widetilde{\Delta}_2, \widetilde{g}_c, \widetilde{\kappa}, \widetilde{q}, c_{1,}c_2, c_3$, which determine the exciton energies, can be expressed in terms of more fundamental material parameters by comparing to the perturbative expression [60]. The second and third terms in Eq. (4.18) stand for the exchange interaction, the fourth and fifth terms are the Zeeman terms, and the latest term accounts for the diamagnetic shift. The coefficients $\widetilde{\Delta}_2$, $\widetilde{q}$, and c_3 are the sources of the anisotropy.

For analysing the splitting patterns, we can express Eq. (4.18) as a matrix and select the quantization axis of the basis along the direction of the magnetic field $\mathbf{B}$ in the ζ axis. We choice the basis $\left|J^t, J_\zeta^t\right\rangle$ that can diagonalize the second term in Eq. (4.18), where

$$\mathbf{J}^t = \mathbf{J} + \vec{\sigma} \;\; (J^t = 2 \text{ or } 1). \tag{4.19}$$

The relation between $\left|J^t, J^t_\zeta\right\rangle$ and $\left|\frac{1}{2}, \pm\frac{1}{2}\right\rangle \times |J, J_\zeta\rangle$ is [59]

$$|2,2\rangle = \left|\frac{3}{2},\frac{3}{2}\right\rangle \left|\frac{1}{2},\frac{1}{2}\right\rangle, \tag{4.20a}$$

$$|2,1\rangle = \frac{\sqrt{3}}{2}\left|\frac{3}{2},\frac{1}{2}\right\rangle \left|\frac{1}{2},\frac{1}{2}\right\rangle + \frac{1}{2}\left|\frac{3}{2},\frac{3}{2}\right\rangle \left|\frac{1}{2},\frac{-1}{2}\right\rangle, \tag{4.20b}$$

$$|2,0\rangle = \frac{1}{2}\left|\frac{3}{2},\frac{-1}{2}\right\rangle \left|\frac{1}{2},\frac{1}{2}\right\rangle + \frac{1}{\sqrt{2}}\left|\frac{3}{2},\frac{1}{2}\right\rangle \left|\frac{1}{2},\frac{-1}{2}\right\rangle, \tag{4.20c}$$

$$|2,-1\rangle = \frac{1}{2}\left|\frac{3}{2},\frac{-3}{2}\right\rangle \left|\frac{1}{2},\frac{1}{2}\right\rangle + \frac{\sqrt{3}}{2}\left|\frac{3}{2},\frac{-1}{2}\right\rangle \left|\frac{1}{2},\frac{-1}{2}\right\rangle, \tag{4.20d}$$

$$|2,-2\rangle = \left|\frac{3}{2},\frac{-3}{2}\right\rangle \left|\frac{1}{2},\frac{-1}{2}\right\rangle, \tag{4.20e}$$

$$|1,1\rangle = \frac{-1}{2}\left|\frac{3}{2},\frac{1}{2}\right\rangle \left|\frac{1}{2},\frac{1}{2}\right\rangle + \frac{\sqrt{3}}{2}\left|\frac{3}{2},\frac{3}{2}\right\rangle \left|\frac{1}{2},\frac{-1}{2}\right\rangle, \tag{4.20f}$$

$$|1,0\rangle = \frac{1}{\sqrt{2}}\left|\frac{3}{2},\frac{-1}{2}\right\rangle \left|\frac{1}{2},\frac{1}{2}\right\rangle - \frac{1}{\sqrt{2}}\left|\frac{3}{2},\frac{1}{2}\right\rangle \left|\frac{1}{2},\frac{-1}{2}\right\rangle, \tag{4.20g}$$

$$|1,-1\rangle = \frac{\sqrt{3}}{2}\left|\frac{3}{2},\frac{-3}{2}\right\rangle \left|\frac{1}{2},\frac{1}{2}\right\rangle - \frac{1}{2}\left|\frac{3}{2},\frac{-1}{2}\right\rangle \left|\frac{1}{2},\frac{-1}{2}\right\rangle. \tag{4.20h}$$

The states $|1,1\rangle$, $|1,0\rangle$, and $|1,-1\rangle$ are dipole active for σ_+, π, and σ_- polarizations[3] respectively. If the magnetic field (ζ axis) is applied along $\langle 001\rangle$ directions of the crystal (see Fig. 4.2), the matrix can be expressed as

$$\left(\begin{array}{ccccccccc}
 & |2,2\rangle & |2,-2\rangle & |2,1\rangle & |1,1\rangle & |2,-1\rangle & |1,-1\rangle & |2,0\rangle & |1,0\rangle \\
|2,2\rangle & I_{11} & I_{12} & 0 & 0 & 0 & 0 & 0 & 0 \\
|2,-2\rangle & I_{21} & I_{22} & 0 & 0 & 0 & 0 & 0 & 0 \\
|2,1\rangle & 0 & 0 & II_{11} & II_{12} & 0 & 0 & 0 & 0 \\
|1,1\rangle & 0 & 0 & II_{21} & II_{22} & III_{11} & III_{12} & 0 & 0 \\
|2,-1\rangle & 0 & 0 & 0 & 0 & III_{21} & III_{22} & 0 & 0 \\
|1,-1\rangle & 0 & 0 & 0 & 0 & 0 & 0 & 0 & 0 \\
|2,0\rangle & 0 & 0 & 0 & 0 & 0 & 0 & IV_{11} & IV_{12} \\
|1,0\rangle & 0 & 0 & 0 & 0 & 0 & 0 & IV_{21} & IV_{22}
\end{array}\right) \tag{4.21}$$

---

[3] σ_+, and σ_- are the right-handed and left-handed circular polarizations in the Faraday configuration; and π is the linear polarization with **E** parallel to **B** in the Voigt configuration.

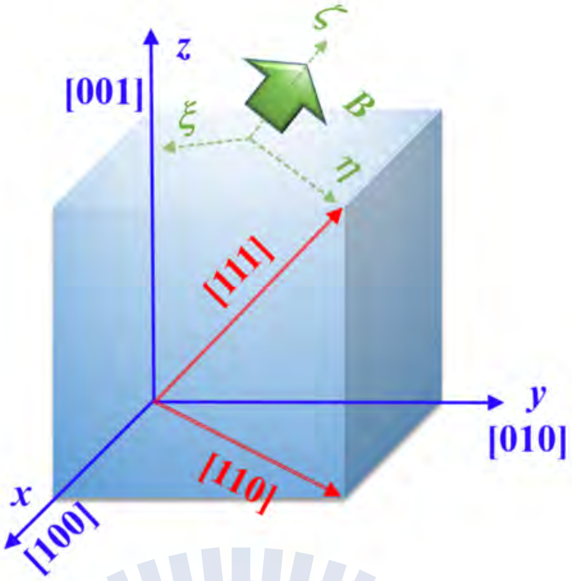

FIGURE 4.2: Diagram of the directions of the applied magnetic field **B** and the crystal. The axes x, y, and z are the crystal lattice coordinate; and the axis ζ is the coordinate of the applied magnetic field.

where

$$\begin{aligned} I \;=\; & (E_b+\bar{c})\begin{pmatrix}1 & 0\\ 0 & 1\end{pmatrix} + (\frac{3}{4}\widetilde{\Delta}_1+\bar{c}_2)\begin{pmatrix}1 & 0\\ 0 & 1\end{pmatrix} + (\frac{1}{2}\bar{g}_c-3\bar{\kappa})\begin{pmatrix}1 & 0\\ 0 & -1\end{pmatrix} \\ & +\frac{1}{16}\begin{pmatrix}27(\widetilde{\Delta}_2-4\bar{q}) & 12\widetilde{\Delta}_2\\ 12\widetilde{\Delta}_2 & 27(\widetilde{\Delta}_2+4\bar{q})\end{pmatrix}, \end{aligned} \tag{4.22a}$$

$$\begin{aligned} II \;=\; & (E_b+\bar{c}-2\bar{\kappa})\begin{pmatrix}1 & 0\\ 0 & 1\end{pmatrix} + \frac{1}{4}\widetilde{\Delta}_1\begin{pmatrix}3 & 0\\ 0 & -5\end{pmatrix} \\ & +\frac{1}{4}(\bar{g}_c+2\bar{\kappa}-2\bar{c}_2)\begin{pmatrix}1 & -\sqrt{3}\\ -\sqrt{3} & -1\end{pmatrix} \\ & +\frac{1}{16}\begin{pmatrix}15(\widetilde{\Delta}_2-2\bar{q}) & -26\sqrt{3}\bar{q}\\ -26\sqrt{3}\bar{q} & -41(\widetilde{\Delta}_2+2\bar{q})\end{pmatrix}, \end{aligned} \tag{4.22b}$$

$$\begin{aligned} III \quad = \quad & (E_b + \overline{c} - 2\overline{\kappa}) \begin{pmatrix} 1 & 0 \\ 0 & 1 \end{pmatrix} + \frac{1}{4}\widetilde{\Delta}_1 \begin{pmatrix} 3 & 0 \\ 0 & -5 \end{pmatrix} \\ & -\frac{1}{4}(\overline{g}_c + 2\overline{\kappa} + 2\overline{c}_2) \begin{pmatrix} 1 & -\sqrt{3} \\ -\sqrt{3} & -1 \end{pmatrix} \\ & +\frac{1}{16} \begin{pmatrix} 15(\widetilde{\Delta}_2 + 2\overline{q}) & 26\sqrt{3}\overline{q} \\ 26\sqrt{3}\overline{q} & -41(\widetilde{\Delta}_2 - 2\overline{q}) \end{pmatrix}, \end{aligned} \tag{4.22c}$$

$$\begin{aligned} IV \quad = \quad & (E_b + \overline{c}) \begin{pmatrix} 1 & 0 \\ 0 & 1 \end{pmatrix} + \begin{pmatrix} \frac{3}{4}\widetilde{\Delta}_1 - \overline{c}_2 & \overline{\kappa} + \frac{1}{2}\overline{g}_c \\ \overline{\kappa} + \frac{1}{2}\overline{g}_c & \frac{-5}{4}\widetilde{\Delta}_1 - \overline{c}_2 \end{pmatrix} \\ & +\frac{1}{16} \begin{pmatrix} 39\widetilde{\Delta}_2 & 4\overline{q} \\ 4\overline{q} & -41\widetilde{\Delta}_2 \end{pmatrix}, \end{aligned} \tag{4.22d}$$

where the magnetic field related parameters are

$$\overline{g}_c = \widetilde{g}_c \mu_B B, \tag{4.22e}$$

$$\overline{q} = \widetilde{q} \mu_B B, \tag{4.22f}$$

$$\overline{\kappa} = \widetilde{\kappa} \mu_B B, \tag{4.22g}$$

$$\overline{c} = \frac{1}{2}\gamma^2 R^{ex}(c_1 + \frac{5}{4}c_2), \tag{4.22h}$$

$$\overline{c}_2 = \frac{1}{2}\gamma^2 R^{ex} c_2. \tag{4.22i}$$

The existence of the exchange interaction ($\widetilde{\Delta}_1$, $\widetilde{\Delta}_2$) splits the degenerate states, and the applied magnetic field leads coupling between diploe active and inactive states as shown in Eqs. (4.22b), (4.22c), and (4.22d). Thus, the dark (diploe inactive) states are observable under high magnetic fields.

4.3 Exciton-Polariton with Spatial Dispersion

4.3.1 Isotropic

For phenomenologically understanding the spectra of ellipsometry measurements near an excitonic transition, we consider the exciton-polariton model with spatial dispersion and in general, both p and s polarization in arbitrary incidence. When the displacement and electric fields vary with time t and position r, the connection between the displacement field and the electric field can be expressed as [56, 61]

$$\overrightarrow{D}(\mathbf{r},t) = \int d^3\mathbf{r}' \int dt' \varepsilon(\mathbf{r},\mathbf{r}',t-t')\overrightarrow{E}(\mathbf{r}',t'). \tag{4.23}$$

For infinite and homogeneous media, i.e. $\varepsilon(\mathbf{r},\mathbf{r}',t-t') = \varepsilon(\mathbf{r}-\mathbf{r}',t-t')$, the above Eq. (4.23) can be transformed to be represented as the wavevector $\mathbf{q}$ and the angular frequency ω as

$$\overrightarrow{D}(\mathbf{q},\omega) = \varepsilon(\mathbf{q},\omega)\overrightarrow{E}(\mathbf{q},\omega). \tag{4.24}$$

In general, $\varepsilon(\mathbf{q},\omega)$ can be a tensor. We assume the wavevector- and frequency-dependent dielectric response ε based on a coupled harmonic oscillator model[4] can be written as [33, 61]

$$\varepsilon(\mathbf{q},\omega) = \varepsilon_b + \frac{\omega_p^2}{\omega_T^2 + Dq^2 - \omega^2 - i\nu\omega}. \tag{4.25}$$

Where ε_b is the background dielectric constant, ω_p^2 is the strength of the transition, ω_T is the transition frequency, ν is a phenomenon damping constant and the parameter $D = \hbar\omega_T/M_{ex}$, which describes the spatial non-locality due to exciton CM motion. The wavevector $\mathbf{q}$ also satisfies the Maxwell's equation [56, 61]

$$\mathbf{q} \times (\mathbf{q} \times \mathbf{E}) - \frac{\omega^2}{c^2}\varepsilon(\mathbf{q},\omega)\mathbf{E} = 0, \tag{4.26}$$

within a homogeneous media. Where $\mathbf{E}$ is the electric field in the medium, and c is the speed of light. Hence, the wavevector $\mathbf{q}$ has more than one solutions [33, 61].

$$q^2 = \frac{1}{2}(\Gamma_0^2 + \varepsilon_b\frac{\omega^2}{c^2}) \pm \frac{1}{2}[(\Gamma_0^2 - \varepsilon_b\frac{\omega^2}{c^2})^2 + \frac{4\omega^2\omega_p^2}{Dc^2}]^{1/2} \tag{4.27a}$$

for two transverse modes (labeled q_1 and q_2), and

$$q^2 = \Gamma_0^2 - \frac{\omega_p^2}{D\varepsilon_b} \tag{4.27b}$$

---

[4] Replacing ω_0 in Eq. (4.12f) with $q_{ex} = q$ into a non-spatial dispersive harmonic dielectric response function yields Eq. (4.25).

for one longitudinal mode (labeled q_3). Where

$$\Gamma_0 \equiv \frac{(\omega^2 + i\nu\omega - \omega_T^2)}{D}. \tag{4.28}$$

The dispersion relations are illustrated in Fig. 4.3 without dissipation ($\nu = 0$). To obtain the ellipsometric parameters, we can calculate the reflection coefficients for s (two transverse modes) and p (two transverse modes and one longitudinal mode) polarization in a oblique incidence configuration respectively and use the generalized additional boundary condition (ABC) [36]. And, we can obtain Ψ and Δ using Eq. (2.3).

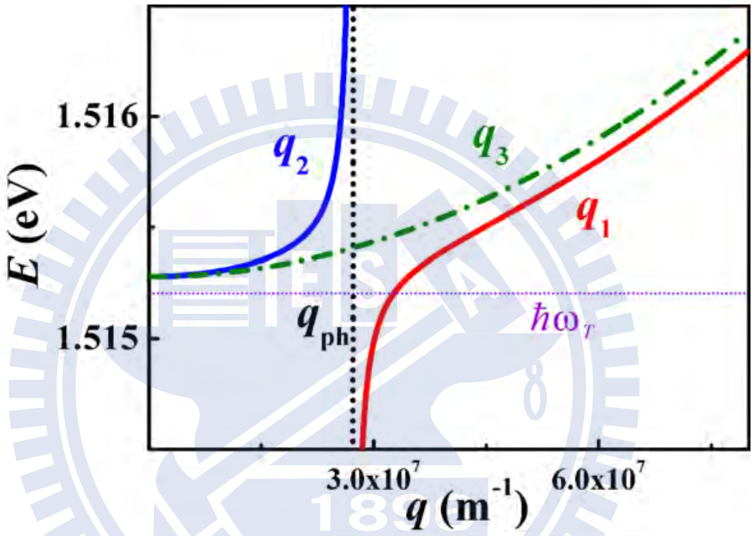

FIGURE 4.3: Schematic dispersion relation $E = \hbar\omega$ vs. real part of q of the two transverse modes q_1 and q_2, and the single longitudinal mode q_3 of spatial dispersive exciton-polariton in the absence of dissipation $\nu = 0$. $q_{\mathrm{ph}} = \omega\sqrt{\varepsilon_b}/c$ is the wavevector of photons.

4.3.2 Anisotropic Exciton Effective Mass

If the exciton effective mass is anisotropic, i.e. the exciton motion depends on the moving direction. For instance, if we assume the exciton effective mass in the x-y plane is a function of the external magnetic field B, equation (4.25) can be rewritten as

$$\varepsilon(Q, q_z, \omega) = \varepsilon_b + \frac{\omega_p^2}{\omega_T^2 + [D'(B)Q^2 + Dq_z^2] - \omega^2 - i\nu\omega}; \tag{4.29}$$

where Q is the wavevector in the x-y plane, q_z is the wavevector in the z direction, (Fig. 4.4), and

$$D'(B) = \frac{\hbar\omega_T}{M_{ex}(B)}, \tag{4.30a}$$

with

$$D'(0) = D. \tag{4.30b}$$

Thus, similar to the isotropic ones, the transverse mode wavevectors satisfying Eq. (4.26) yields

$$q^2 = \frac{\omega^2}{c^2}\varepsilon(Q, q_z, \omega), \tag{4.31a}$$

and the longitudinal mode wavevector satisfies

$$\varepsilon(Q, q_z, \omega) = 0. \tag{4.31b}$$

4.4 Oblique Incidence of s & p Polarized Light

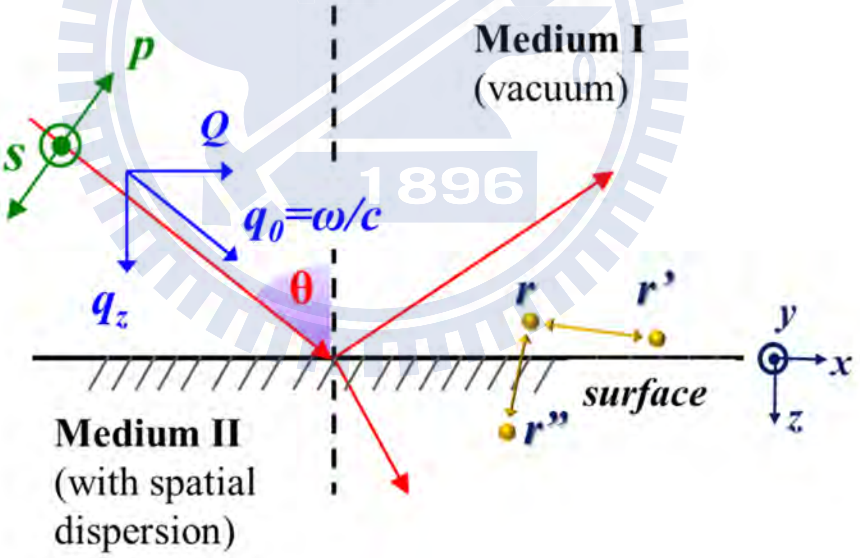

FIGURE 4.4: Diagram of light incident to a surface separating vacuum and spatial dispersive medium .

Figure 4.4 is a diagram of light incident with a wavevector q_0 and a incident angle θ from medium I into spatial dispersive medium II. Q is the projection of the wavevector in the x direction[5] and remains the same value $q_0 \sin\theta$ for all

---

[5] We assume the incidence plane is parallel to the x direction.

interfaces due to the conservation of momentum. To analyse the response of non-local polariton for an arbitrary polarized light, we derive the electric field, magnetic field, and excitonic polarization in the medium II for s- and p- polarized components respectively.

4.4.1 s-polarized

For the s- polarized component, there is no longitudinal mode. The transmitted electric field can be written as (see Fig. 4.4)

$$E_y(z) = \sum_{n=1}^{2}(E_n^+ e^{iq_n z} + E_n^- e^{-iq_n z})e^{i(Qx-\omega t)}, \tag{4.32}$$

where q_n is the z- component of the wavevector for $n = 1$ and 2 indicating two transverse modes respectively. We can then use the Maxwell equation

$$\nabla \times \overrightarrow{E} = -\frac{1}{c}\frac{\partial \overrightarrow{H}}{\partial t} = \frac{i\omega}{c}\overrightarrow{H}, \tag{4.33}$$

and neglect the term Exp$[i(Qx - \omega t)]$ for convenience to obtain the magnetic field component

$$\begin{aligned} H_x(z) &= \frac{-ic}{\omega}\frac{\partial E_y}{\partial z} \qquad (4.34)\\ &= \frac{-i}{q_0}\sum_{n=1}^{2}(iq_n E_n^+ e^{iq_n z} - iq_n E_n^- e^{-iq_n z}) \\ &= \sum_{n=1}^{2}\frac{q_n}{q_0}(E_n^+ e^{iq_n z} - E_n^- e^{-iq_n z}) \\ &= \sum_{n=1}^{2} Y_n^s (E_n^+ e^{iq_n z} - E_n^- e^{-iq_n z}), \end{aligned}$$

where $Y_n^s = q_n/q_0$ is the admittance for the s-component. To obtain the polarization $\overrightarrow{\mathcal{P}}$ induced by excitons, we use a linear constitutive relation connecting the displacement field $\overrightarrow{\mathcal{D}}$ and the electric field $\overrightarrow{E}$.

$$\begin{cases} \overrightarrow{\mathcal{D}}(\overrightarrow{q},\omega) = \overrightarrow{E}(\overrightarrow{q},\omega) + 4\pi\overrightarrow{\mathcal{P}}(\overrightarrow{q},\omega); \\ \overrightarrow{\mathcal{P}}(\overrightarrow{q},\omega) = \chi(\overrightarrow{q},\omega)\overrightarrow{E}(\overrightarrow{q},\omega). \end{cases} \tag{4.35}$$

The electric susceptibility of the medium

$$\begin{aligned}\chi(\overrightarrow{q},\omega) &= \frac{\varepsilon-1}{4\pi} \\ &= \frac{\varepsilon_b-1}{4\pi}+\frac{\omega_p^2}{4\pi D}\chi_n,\end{aligned} \tag{4.36}$$

where $\Gamma=(\omega^2+i\upsilon\omega-\omega_T^2)/D-Q^2$, $\chi_n=1/(q_n^2-\Gamma^2)$, and the last term of Eq. (4.36) is the excitonic polarization associated with the excitonic transition.

4.4.2 *p*-polarized

For the *p*- polarized component, there are two transverse ($n=1,2$) and one longitudinal ($n=3$) modes. The transmitted electric field in the x direction neglecting Exp$[i(Qx-\omega t)]$ can be expressed as

$$E_x(z)=\sum_{n=1}^{3}(E_n^+e^{iq_nz}+a_nE_n^-e^{-iq_nz}); a_{1,2}=-1, a_3=1. \tag{4.37}$$

We can get the magnetic field through

$$\nabla\times\overrightarrow{E}=\widehat{x}(\frac{\partial E_z}{\partial y}-\frac{\partial E_y}{\partial z})+\widehat{y}(\frac{\partial E_x}{\partial z}-\frac{\partial E_z}{\partial x})+\widehat{z}(\frac{\partial E_y}{\partial x}-\frac{\partial E_x}{\partial y})=\frac{i\omega}{c}\overrightarrow{H}. \tag{4.38}$$

Thus, the magnetic field component

$$\begin{aligned}H_y(z) &= \frac{-ic}{\omega}(\frac{\partial E_x}{\partial z}-\frac{\partial E_z}{\partial x}) \\ &= \frac{-i}{q_0}(\frac{\partial E_x}{\partial z}-iQE_z) \\ &= \frac{-i}{q_0}\sum_{n=1}^{2}iq_n(E_n^+e^{iq_nz}+E_n^-e^{-iq_nz})+\frac{iQ^2}{q_n}(E_n^+e^{iq_nz}+E_n^-e^{-iq_nz}) \\ &= \sum_{n=1}^{2}\frac{\varepsilon_nq_0}{q_n}(E_n^+e^{iq_nz}+E_n^-e^{-iq_nz}) \\ &= \sum_{n=1}^{2}Y_n^p(E_n^+e^{iq_nz}+E_n^-e^{-iq_nz}).\end{aligned} \tag{4.39}$$

We use $E_z=(-Q/q_n)E_x=-D_nE_x$ for $n=1,2$, $E_z=(q_3/Q)E_x=-D_3E_x$, and Y_n^p= ε_nq_0/q_n is the admittance for the *p*-component. It should be mentioned that only two components are exist for H_y.

4.5 Transfer Matrix for Non-Spatial Dispersive Material

The transfer matrix for a common material[6] can be found in general optics textbooks [62]. We follow several important issues here. The electric field components traveling in $+z$ and $-z$ directions (Fig. 4.5) can be related to the total electric field E and magnetic field H by a 2×2 matrix $\mathbf{G}_I$,

$$\begin{bmatrix} E \\ H \end{bmatrix} = \mathbf{G}_I \begin{bmatrix} E^+ e^{iq_I z} \\ E^- e^{-iq_I z} \end{bmatrix}; \tag{4.40a}$$

$$\mathbf{G}_I = \begin{bmatrix} 1 & 1 \\ Y_I & -Y_I \end{bmatrix}. \tag{4.40b}$$

The admittance Y_I equals to q_I/q_0 for s-polarized light and $\varepsilon_b q_0/q_I$ for p-polarized light. Where q_I is the z-component of the wavevector inside the material with background dielectric constant ε_b. The transfer matrix can be obtained through connecting the fields at the left boundary z^L and the right boundary $z^R = z^L + d^I$

$$\begin{bmatrix} \mathbf{E} \\ \mathbf{H} \end{bmatrix}_{z^R} = \mathbf{G}_I \mathbf{T}(d^I) \mathbf{G}_I^{-1} = \begin{bmatrix} \mathbf{E} \\ \mathbf{H} \end{bmatrix}_{z^L} \equiv \mathbf{M}_I \begin{bmatrix} \mathbf{E} \\ \mathbf{H} \end{bmatrix}_{z^L} \tag{4.41}$$

with the transfer matrix

$$\mathbf{M}_I = \begin{bmatrix} \cos(q_I d^I) & -i\frac{1}{Y_I}\sin(q_I d^I) \\ -iY_I \sin(q_I d^I) & \cos(q_I d^I) \end{bmatrix}, \tag{4.42}$$

where $\mathbf{T}(z) = \mathrm{diag}(\mathrm{e}^{iq_I z}, e^{-iq_I z})$[7].

---

[6] Exciton-free and non-spatial dispersive material.

[7] diag(...) is a diagonal matrix constructor.

4.6 Transfer Matrix for Spatial Dispersive Material

If the sample considered consists of several layers of spatial dispersive and non-dispersive materials, it is efficient to construct transfer matrixes to calculate the resulted reflection coefficients of the overall system by matrix multiplication [63–66]. In this section, we describe in detail how to construct a transfer matrix of a spatial dispersive material and to reduce its dimension by applying general ABCs [36] for both *s*- and *p*- polarized components.

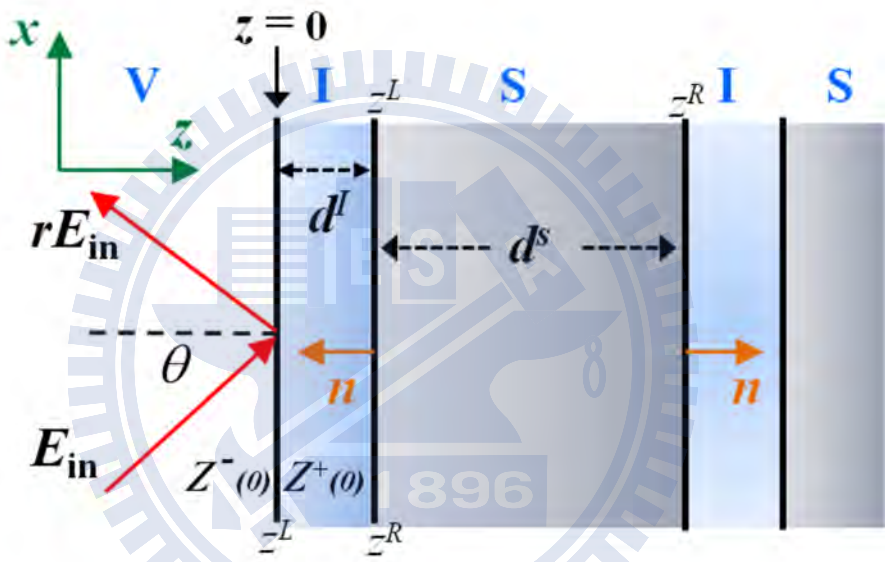

FIGURE 4.5: Diagram of a multi-layer system. "V" represents vacuum, "I"represents insulator, and "S"represents semiconductor with spatial dispersion.

4.6.1 *s*-polarized

For the *s*-component, there are two transverse modes in $+z$ and $-z$ directions respectively (Fig. 4.5). We can use a 4×4 matrix $\mathbf{G}_s$ to connect the four electric field components and the 4×1 vector formed by the electric field E_y, magnetic field H_x, excitonic polarization $\mathcal{P}$, and the derivative of the excitonic polarization to the normal direction n ($+z$ or $-z$).

$$\begin{bmatrix} E_y \\ H_x \\ \mathcal{P} \\ \partial_n\mathcal{P} \end{bmatrix} = \mathbf{G}_s \begin{bmatrix} E_1^+ e^{iq_1 z} \\ E_1^- e^{-iq_1 z} \\ E_2^+ e^{iq_2 z} \\ E_2^- e^{-iq_2 z} \end{bmatrix}, \tag{4.43}$$

where,

$$\mathbf{G}_s = \begin{bmatrix} 1 & 1 & 1 & 1 \\ Y_1^s & -Y_1^s & Y_2^s & -Y_2^s \\ \chi_1 & \chi_1 & \chi_2 & \chi_2 \\ iq_1\chi_1 & -iq_1\chi_1 & iq_2\chi_2 & -iq_2\chi_2 \end{bmatrix}. \tag{4.44}$$

Each component of $\mathbf{G}_s$ (Eq. (4.44)) can be derived from Eqs. (4.34) and (4.36). And we can relate the fields at the left boundary z^L and the right boundary $z^R = z^L + d^s$ through

$$\begin{bmatrix} \mathbb{F}_s \\ \mathcal{P} \\ \partial_n\mathcal{P} \end{bmatrix}_{z^R} = \mathbf{N}_T^s \begin{bmatrix} \mathbb{F}_s \\ \mathcal{P} \\ \partial_n\mathcal{P} \end{bmatrix}_{z^L}. \tag{4.45}$$

The field vector $\mathbb{F}_s = (E_y, H_x)^T$, and the transfer matrix

$$\mathbf{N}_T^s = \mathbf{G}_s\mathbf{T}(d^s)\mathbf{G}_s^{-1}, \tag{4.46}$$

where $\mathbf{T}(z) = \mathrm{diag}(\mathrm{e}^{iq_1 z}, e^{-iq_1 z}, e^{iq_2 z}, e^{-iq_2 z})$. To reduce the dimension of $\mathbf{N}_T^s$, we apply the generalized ABC [36]

$$\alpha_{yy}\mathcal{P} + \partial_n\mathcal{P} = 0, \tag{4.47a}$$

to both interface of the left boundary z^L and the right boundary z^R. α_{yy} can be written as

$$\alpha_{yy} = i\Gamma\frac{1 - U_y}{1 + U_y}, \tag{4.47b}$$

and some of its values that represents different types of ABCs are listed in Table 4.1.

Then Eqs. (4.46) and (4.47b) yield

$$\mathcal{P}(z^R) = M_{pf}\mathbb{F}_s(z^L) + M_{pp}\mathcal{P}(z^L) + M_{pp'}\alpha_{yy}\mathcal{P}(z^L), \tag{4.48a}$$

TABLE 4.1: Special cases of ABC for s polarized light.

ABC	U_y	Excitonic polarization
Pekar	-1	$\mathcal{P}_y(0) = 0$
Fuchs-Kliewer	1	$\partial_n \mathcal{P}_y(0) = 0$
Agarnal *et al.*	0	$i\Gamma \mathcal{P}_y(0) + \partial_n \mathcal{P}_y(0) = 0$

$$-\alpha_{yy}\mathcal{P}(z^R) = M_{p'f}\mathbb{F}_s(z^L) + M_{p'p}\mathcal{P}(z^L) + M_{p'p'}\alpha_{yy}\mathcal{P}(z^L), \tag{4.48b}$$

where $M_{ff} = \{(N^s_{11}, N^s_{12}), (N^s_{21}, N^s_{22})\}^{\mathrm{T}}$, $M_{fp} = \{N^s_{13}, N^s_{23}\}^{\mathrm{T}}$, $M_{fp'} = \{N^s_{14}, N^s_{24}\}^{\mathrm{T}}$, $M_{pf} = \{N^s_{31}, N^s_{32}\}$, $M_{p'f} = \{N^s_{41}, N^s_{42}\}$, $M_{pp} = N^s_{33}$, $M_{pp'} = N^s_{34}$, $M_{p'p} = N^s_{43}$, and $M_{p'p'} = N^s_{44}$[8]. $\mathcal{P}(z^L)$ can be solved by the associated Eqs. (4.48a) and (4.48b),

$$\mathcal{P}(z^L) = -\mathbb{S}^{-1}(\alpha_{yy}M_{pf} + M_{p'f})\mathbb{F}_s(z^L), \tag{4.49}$$

where $\mathbb{S} = \alpha_{yy}M_{pp} + \alpha_{yy}M_{pp'}\alpha_{yy} + M_{p'p} + M_{p'p'}\alpha_{yy}$. The relation between $\mathbb{F}_s(z^R)$ and $\mathbb{F}_s(z^L)$ can be written as

$$\mathbb{F}_s(z^R) = \mathbf{M}^s_T\mathbb{F}_s(z^L), \tag{4.50}$$

where

$$\mathbf{M}^s_T = M_{ff} - (M_{fp} + M_{fp'}\alpha_{yy})\mathbb{S}^{-1}(\alpha_{yy}M_{pf} + M_{p'f}) \tag{4.51}$$

is a 2 × 2 transfer matrix for s- polarized component.

4.6.2 p-polarized

It is more complex to construct a transfer matrix for the p-component than that for the s-component. There are two transverse modes and a longitudinal mode in $+z$ and $-z$ directions respectively (Fig. 4.5). Thus a 6 × 6 matrix $\mathbf{G}_p$ similar to $\mathbf{G}_s$(Eq. (4.44)) can be constructed to relate the six electric field components and the electric field E_x, magnetic field H_y, excitonic polarization $\mathcal{P}_x$, $\mathcal{P}_z$ and their

---

[8] N^s_{ab} is the matrix element at row a and column b of the matrix N^s_T.

normal derivatives.

$$\begin{bmatrix} E_x \\ H_y \\ \mathcal{P}_x \\ \mathcal{P}_z \\ \partial_z \mathcal{P}_x \\ \partial_z \mathcal{P}_z \end{bmatrix} = \mathbf{G}_p \begin{bmatrix} E_1^+ e^{iq_1 z} \\ E_1^- e^{-iq_1 z} \\ E_2^+ e^{iq_2 z} \\ E_2^- e^{-iq_2 z} \\ E_3^+ e^{iq_3 z} \\ E_3^- e^{-iq_3 z} \end{bmatrix}, \tag{4.52}$$

where

$$\mathbf{G}_p = \begin{bmatrix} 1 & -1 & 1 & -1 & 1 & 1 \\ Y_1^p & Y_1^p & Y_2^p & Y_2^p & 0 & 0 \\ \chi_1 & -\chi_1 & \chi_2 & -\chi_2 & \chi_3 & \chi_3 \\ -D_1\chi_1 & -D_1\chi_1 & -D_2\chi_2 & -D_2\chi_2 & D_3\chi_3 & -D_3\chi_3 \\ iq_1\chi_1 & iq_1\chi_1 & iq_2\chi_2 & iq_2\chi_2 & iq_3\chi_3 & -iq_3\chi_3 \\ -iq_1 D_1\chi_1 & iq_1 D_1\chi_1 & -iq_2 D_2\chi_2 & -iq_2 D_2\chi_2 & iq_3 D_3\chi_3 & iq_3 D_3\chi_3 \end{bmatrix}. \tag{4.53}$$

The elements of $\mathbf{G}_p$ are defined as in Eqs. (4.36) and (4.39). The fields at the left boundary z^L and the right boundary $z^R = z^L + d^s$ can be related through

$$\begin{bmatrix} \mathbb{F}_p \\ \mathbb{P}_p \\ \partial_n \mathbb{P}_p \end{bmatrix}_{z^R} = \mathbf{N}_T^p \begin{bmatrix} \mathbb{F}_p \\ \mathbb{P}_p \\ \partial_n \mathbb{P}_p \end{bmatrix}_{z^L}, \tag{4.54}$$

where $\mathbb{F}_p = (E_x, H_y)^T$, $\mathbb{P}_p = (\mathcal{P}_x, \mathcal{P}_z)^T$and the transfer matrix

$$\mathbf{N}_T^p = \mathbf{G}_p \mathbf{T}(d^s) \mathbf{G}_p^{-1} = \begin{bmatrix} \mathbf{N}_{11} & \mathbf{N}_{12} & \mathbf{N}_{13} \\ \mathbf{N}_{21} & \mathbf{N}_{22} & \mathbf{N}_{23} \\ \mathbf{N}_{31} & \mathbf{N}_{32} & \mathbf{N}_{33} \end{bmatrix}. \tag{4.55}$$

We conduct the generalized ABC [36],

$$\mathbf{t}\mathbb{P} + \partial_n \mathbb{P} = \mathbf{0} \tag{4.56a}$$

with

$$\mathbf{t} = \begin{bmatrix} \alpha_{xx} & 0 \\ 0 & \alpha_{zz} \end{bmatrix}, \tag{4.56b}$$

TABLE 4.2: Special cases of ABC for p polarized light.

ABC	U_x	U_z	Excitonic polarization
Pekar	-1	-1	$\mathcal{P}_x(0)=0,\ \mathcal{P}_z(0)=0$
Rimbey-Mahan	-1	1	$\mathcal{P}_x(0)=0,\ \partial_n\mathcal{P}_z(0)=0$
Fuchs-Kliewer	1	-1	$\partial_n\mathcal{P}_x(0)=0,\ \mathcal{P}_z(0)=0$
Ting *et al.*	1	1	$\partial_n\mathcal{P}_x(0)=\partial_n\mathcal{P}_z(0)=0$
Agarnal *et al.*	0	0	$i\Gamma\mathcal{P}_x(0)+\partial_n\mathcal{P}_x(0)=i\Gamma\mathcal{P}_z(0)+\partial_n\mathcal{P}_z(0)=0$

to the boundaries at z^R and z^L. α_{xx} and α_{zz} can be written as

$$\alpha_{xx}=i\Gamma\frac{1-U_x}{1+U_x}, \tag{4.57a}$$

$$\alpha_{zz}=i\Gamma\frac{1-U_z}{1+U_z}, \tag{4.57b}$$

and some specific values of the parameters U_x and U_z that represent different types of ABCs are listed in Table 4.2. Then Eqs. (4.54) and (4.55) can be written as

$$\begin{cases} \mathbb{P}(z^R)=\mathbf{N}_{21}\mathbb{F}(z^L)+\mathbf{N}_{22}\mathbb{P}(z^L)+\mathbf{N}_{23}\mathbf{t}\ \mathbb{P}(z^L), \\ -\mathbf{t}\ \mathbb{P}(z^R)=\mathbf{N}_{31}\mathbb{F}(z^L)+\mathbf{N}_{32}\mathbb{P}(z^L)+\mathbf{N}_{33}\mathbf{t}\ \mathbb{P}(z^L). \end{cases} \tag{4.58}$$

Thus the relation

$$\mathbb{P}(z^L)=-\mathbf{S}^{-1}(\mathbf{t}\mathbf{N}_{21}+\mathbf{N}_{31})\mathbb{F}(z^L) \tag{4.59}$$

can be solved by Eq. (4.58) using the same way as introduced in 4.6.1 with $\mathbf{S}=\mathbf{t}\mathbf{N}_{22}+\mathbf{t}\mathbf{N}_{23}\mathbf{t}+\mathbf{N}_{32}+\mathbf{N}_{33}\mathbf{t}$. Finally, we can obtain the relation of the fields at the right boundary and the left boundary,

$$\mathbb{F}(z^R)=[\mathbf{N}_{11}-(\mathbf{N}_{11}+\mathbf{N}_{13}\mathbf{t})\mathbf{S}^{-1}(\mathbf{t}\mathbf{N}_{21}+\mathbf{N}_{31})]\mathbb{F}(z^L)=\mathbf{M}_T^p\mathbb{F}(z^L). \tag{4.60}$$

$\mathbf{M}_T^p$ is the 2×2 transfer matrix for p- polarized component.

4.7 Calculation of Reflection Coefficients

To calculate the reflection coefficient of a multi-layer system (Fig. 4.5 as an example), we can use the property of the impedance[9] match on the surface, i.e. to match the impedance $Z^+(0)$ of the multi-layer system obtained from the transfer

---

[9] Impedance is the ratio of the electric and magnetic fields, and its reciprocal is the admittance.

matrix methods and the surface impedance $Z^-(0)$ of vacuum. The electric field and magnetic field at vacuum can be written as (see Fig. 4.5)

$$E^v(z) = (E_{in}e^{iq_0z} + rE_{in}e^{iq_0z})e^{-i\omega t}; \tag{4.61a}$$

$$H^v(z) = \frac{1}{Z^v}(E_{in}e^{iq_0z} - rE_{in}e^{iq_0z})e^{-i\omega t}. \tag{4.61b}$$

Thus, the surface impedance

$$Z^-(0) = \frac{E^v(0)}{H^v(0)} = \frac{Z^v(1+r)}{(1-r)} = Z^+(0). \tag{4.62}$$

If we have already obtained the surface impedance $Z^+(0) = Z_s$ and $Z^+(0) = Z_p$ for s- and p- polarized component respectively, the reflection coefficients yield

$$r_s = \frac{Z_s - Z_s^v}{Z_s + Z_s^v} \tag{4.63a}$$

for s-polarized component, and

$$r_p = \frac{Z_p - Z_p^v}{Z_p + Z_p^v} \tag{4.63b}$$

for p-polarized component. where $Z_s^v = 1/\cos\theta$, and $Z_p^v = \cos\theta$.

Chapter 5

Discussion

We discuss the ellipsometry measurement results of the GaAs substrate and epitaxial layer respectively in this chapter. For the GaAs substrate, the result is relatively simple, and we use simple model in 4.2.1 to fit the energy shift of the spectra. For the GaAs epitaxial layer, however, the result is much more complicated and has not been reported before. Therefore, we will pay more attention on the discussion of the result of the GaAs epitaxial layer in the following.

5.1 GaAs Substrate

The effects of external magnetic fields on the ellipsometry spectra of the GaAs substrate were investigated. The curves in Figs. 3.2(a) and 3.2(b) shift to higher energy and become stronger as magnetic fields increases. This can be explained by the diamagnetic effect of excitons and the increased oscillator strength due to the magnetic confinement [67]. The amount of diamagnetic shift depends on the radius of the magneto-excitons in the plane perpendicular to the magnetic field (Eq. (4.17)), and can be obtained by solving the Schrödinger equation (4.17) with a magnetic field along the z axis [58]. The calculated magnetic field dependent ground state energy is shown in Fig. 5.1 and compared with the experimental data. The reduced effective mass μ and the dielectric constant ε_b used are 0.05 m_e [68] and 12.8 [69]. However, we should mention that the calculation was only performed with the simple two band hydrogen-like (s-states) exciton in a magnetic field [58]; the Zeeman term, the motion of the exciton, and the electron-hole exchange interaction are neglected.

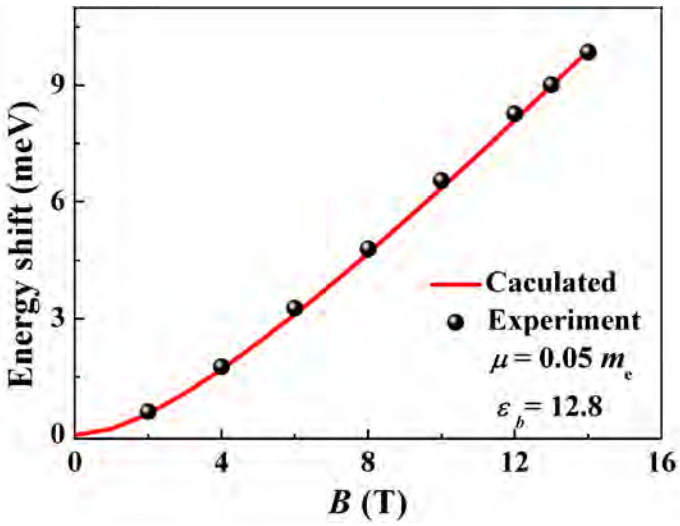

FIGURE 5.1: Measured peak energy (black points) versus magnetic field. The line is fitted by the result of Eq. (4.17) with a reduced effective mass $\mu = 0.05$ m_e and a dielectric constant $\varepsilon_b = 12.8$.

5.2 GaAs Epitaxial Layer

Unlike the results of the GaAs substrate, for the GaAs epitaxial layer, there exists several fine structures even at 0 T, and an extra dip appears when the magnetic field is larger than 6 T in the ellipsometry spectra. In the following, we will discuss the magneto-optical response of the dips A, B; and the leading cause of the dips C, D and their behavior under magnetic fields respectively.

5.2.1 Dips A and B

Figure 5.2 shows the energy shift of the dips A and B as functions of the magnetic field. The dips, which are similar to the results of the GaAs substrate, shift to higher energies due to the diamagnetic effect when the magnetic field is increased. The separation of the two dips is proportional to the magnetic field value as shown in the inset of Fig. 5.2. The behavior of the two dips A and B is similar to what has been reported by F. Willmann, *et al.* (the conventional normal reflectance measurement [52].) The same authors assigned them to be the exciton σ_{-1} states, $\left|J^t, J^t_\zeta\right\rangle = |2,-1\rangle$ and $|1,-1\rangle$, with the component of the total spin angular momentum along the magnetic field direction being equal to -1 [59]. The dip A, a dark state with $J^t = 2$, becomes optically active when it couples to the bright state, dip B (with $J^t = 1$), by the electron-hole exchange interaction and strong magnetic field ($\geq$ 6 T) (see 4.2.2). It should be mentioned that when the angle between the direction of the magnetic field and the exciton CM motion is arbitrary the two states discussed here are no longer good eigenstates (this effect was neglected in Ref. [59]). Although a more precise theory should be constructed for the oblique configuration, we obtained almost the same result as in the Farady configuration [52]. It means, for the energy consideration, the contribution from the exciton CM motion is very small. However, as we show below, the exciton CM motion has an enormous impact on the shape of the ellipsometry spectra.

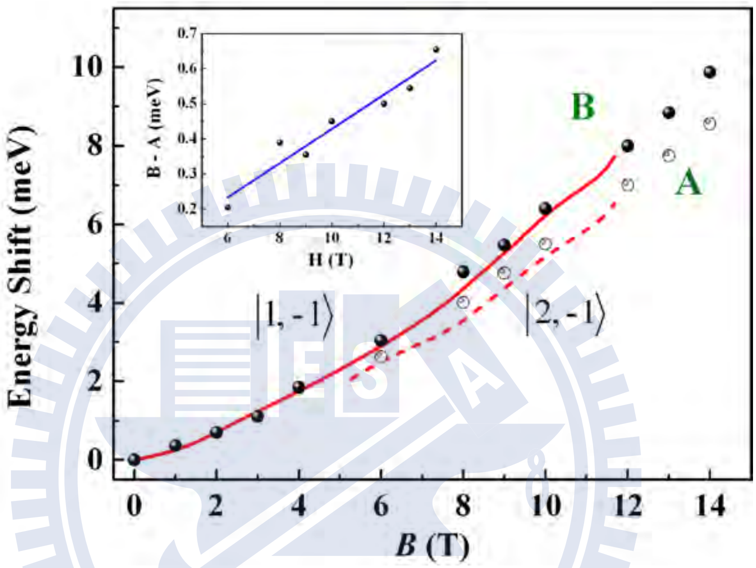

FIGURE 5.2: The measured energy shift of the dips A (circles) and B (solid points) as functions of magnetic fields; lines ($|1,-1\rangle$ solid line, $|2,-1\rangle$ short-dash line) are the reflectance measured data in the Farady configuration (σ_{-1}) from F. Willmann, *et al.* [52] The inset shows the energy difference of the dips B and A with a straight fitting line.

5.2.2 Dips C and D

To understand the behavior of the dips C and D, which have not been reported before, we consider phenomenologically the exciton-polariton model with spatial dispersion for both p- and s- polarizations mentioned in Chapter 4. To determine the ellipsometric parameters, we have to calculate the reflection coefficients of s- (two transverse modes) and p- (two transverse modes and one longitudinal mode) polarization components with an oblique (60°) incident angle and use the generalized ABC [36]. We can then obtain Ψ and Δ using Eq. (2.3) taking into account appropriate transitions between the exciton energy states.

While the dips A and B observed in our experiment are identified as the exciton states reported earlier [52]; the dips C and D, which are present at 0 T, have never been reported and identified before [47–52]. For a rather thick sample (substrate plus epitaxy $\sim$ 0.35 mm), it is difficult to observe such energy splitting from the thermal mismatch between a sample and its mounting [47, 50–52]. The separations between the dips (B, C and C, D) are much smaller than the separations of the exciton levels predicted by the simple hydrogen model (Eq. (4.12)). Another possibility is due to the exchange interaction between the electrons and holes, which can result in separation of states with different angular momentum. But the separations reported earlier ($10^{-2} \sim 10^{-1}$ meV) [70] are too small for what are observed in this work. If the excitons are trapped at the Morse potential [71, 72] near the semiconductor surface, the energy separations obtained between states become larger for higher energy states. The result is still quite different from what is observed in our experiment.

To explain the experimental result that can not be interpreted by the models provided in the previous studies, we propose our original model. We assume that an exciton-free region exists at the interface between the GaAs substrate and the epitaxial layer in addition to the sample surface, because a high concentration of carbon impurity is generated at the interface during MBE process (see Fig. 5.3 (b)) [73]. A diagram of the model is shown in Fig. 5.3 (a). In the model, d_1 and d_2 are the width of the dead (exciton-free) layers, which simply describe the potential due to the interaction of an exciton with the surface and the growth interface respectively [33, 61]. And, we assume the background dielectric constant in the region containing carbon impurity is the same as in other regions. We use the transfer matrix method with spatial dispersion (Section 4.6) and the wavevector obtained from Eq. (4.27) to determine the ellipsometric parameters of this multilayer system.

The modulation of the calculated Δ spectra with various parameters: d_1, d_2, l, and ABC are shown in Fig. 5.4 . The shape of the spectra are more sensitive to the width of the dead layer d_1 at the surface than to the width of the dead layer d_2 at the growth interface. Because the length of the epitaxial layer is known ($\sim$ 1 μm), there are only the parameters d_1, d_2 (not as important as d_1) and the choice of ABC can be changed to determine the shape of the spectra. However, without losing the physical meaning, the dead layer width d_1 should not be less than two times of the GaAs exciton Bohr radius ($\sim$ 24 nm) [70], and the dead layer width d_2

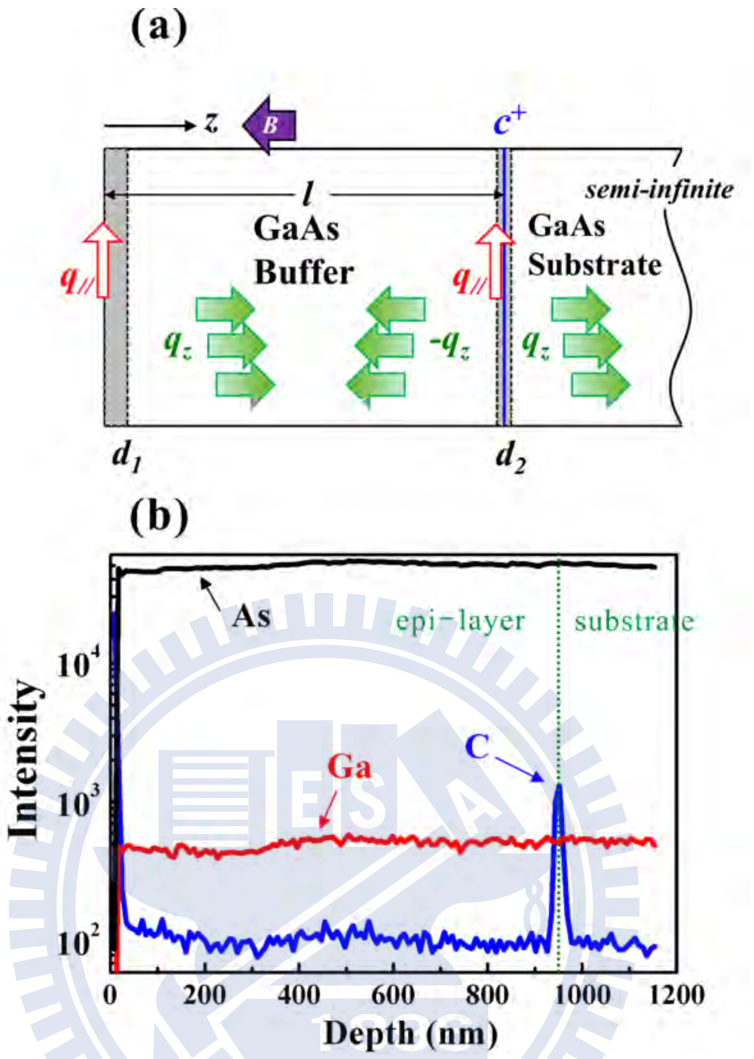

FIGURE 5.3: Diagram of the purposed model (a) and measured SIMS data (b). In (a), c^+ represents carbon impurities at the growth interface. We assume that d_1, d_2 are the dead layer widths at the surface and the growth interface respectively, and l is the epitaxial layer thickness. (b) The measured SIMS data for Ga, As, and C. The depth is counted from the surface and can just be a reference because its accuracy and resolution ($\sim$ 10 nm) is not very well.

is supposed to be smaller than d_1. In addition, recent studies [10–12] showed that the results of using Pekar's ABC is more close to the results obtained by microscopic calculations than using other ABCs. Therefore, we choice the parameters d_1=33 nm, d_2=8 nm, and Pekar's ABC to fit the experimental results. The calculated ellipsometry spectra and normal-incidence reflectance spectrum are shown in Fig. 5.5 (a), (b), and (c) respectively. The shapes of the calculated spectra are quite similar to the experimental results shown in the insets. In comparison to the calculated ellipsometry spectra, the reflectance spectrum, which is obtained by using the same model and parameters except the transition energy, shows very

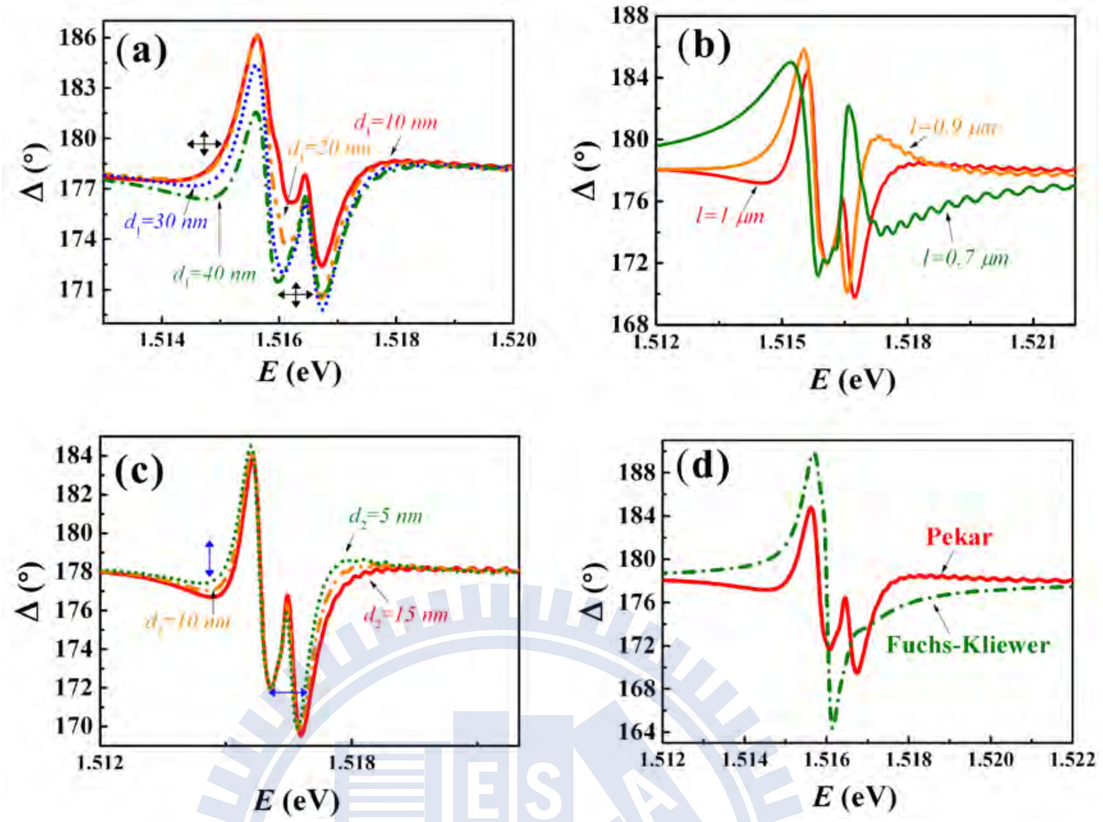

Figure 5.4: Calculated Δ spectra for various d_1 (a), d_2(c), l(b), and different types of ABCs (d).

faint fine structures. This explains why the fine structure is difficult to be observed using normal-incidence reflection measurements. The fine structures in the calculated spectra are due to the interference of multi-polariton waves reflecting back and forth from the two boundaries as shown in Fig. 5.5. The reason that such detailed interference patterns can be observed in this work is the unique configuration of the ellipsometry system. It measures the reflectivity ratio of the p- and s- components in an oblique configuration, which provides a large wave-vector component parallel to the interfaces. This makes it more sensitive to the interfaces than the conventional normal-incidence reflection measurements.

The phenomenological model used here treats the exciton as a solid sphere. It cannot describe the distortion of electron- and hole- wavefunctions respectively near the boundaries and the internal motion of the exciton [10–12]. This may result in some dissatisfies between the calculated and the experimental results. First, the separation between the two dips C and D from the calculation (0.69 meV) is slightly smaller than the experimental data (0.87 meV). Second, discrepancies

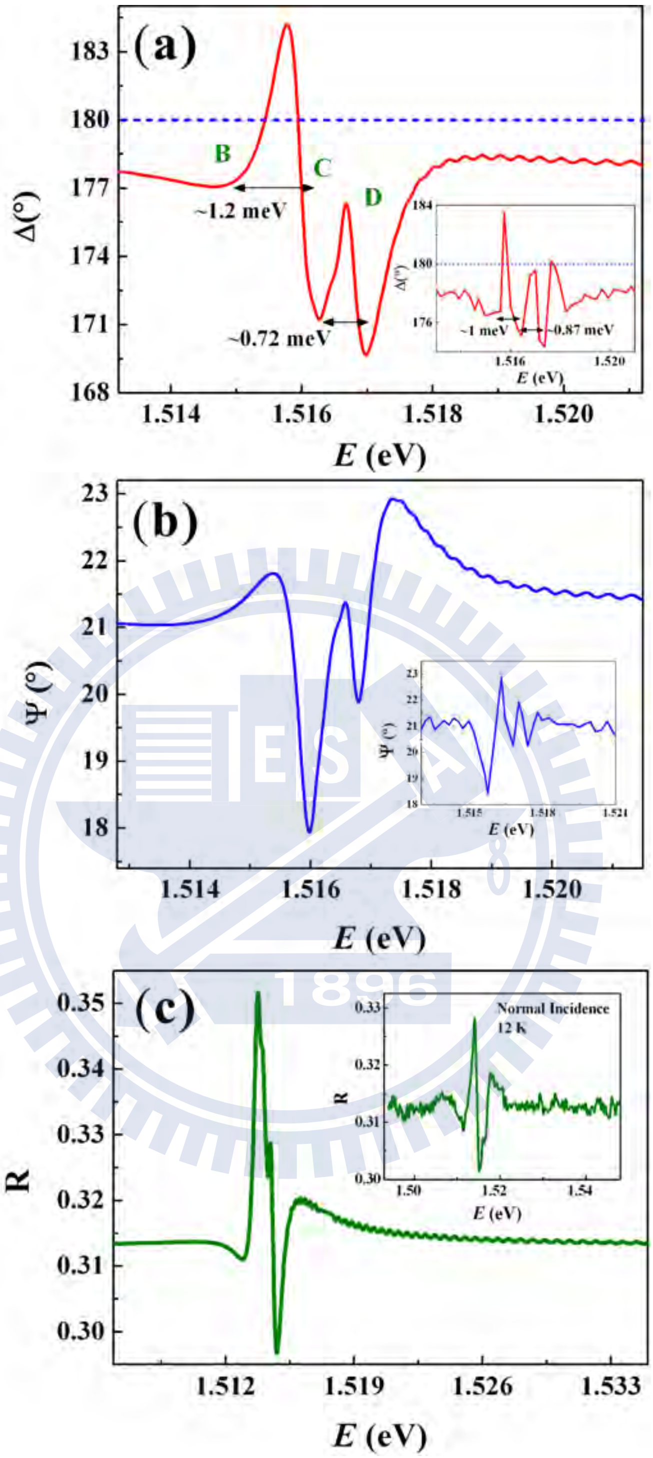

FIGURE 5.5: (a), (b) Calculated spectra of Δ and Ψ at 0 T with parameters: d_1=33 nm, d_2=8 nm, l=1 μm, $\hbar\nu$=0.32 meV, $\hbar\omega_p$=0.055 eV, M_{ex}=0.22 m_0 [45, 46], and Pekar's ABC [32, 36]. The insets are the experimental data measured at 4.2 K, 0 T. (c) Calculated normal-incidence reflectance spectrum using the same model and parameters as in (a), (b) except for the transition energy. The inset is the experimental data of normal-incidence reflectance measured at 12 K, 0 T.

exist in the shapes at energy around 1.518 eV in the spectra, and to fit the shapes and the relative amplitudes of the peaks and dips in the Ψ and Δ spectra well simultaneously is difficult. Another thing, which is difficult to explain, is why the separation between the two dips becomes different when the magnetic field is changed. Because the dips C and D are caused by the interferences among the polariton waves bounced between the two boundaries and are not due to other excitonic states, their relative position should stay the same under magnetic fields.

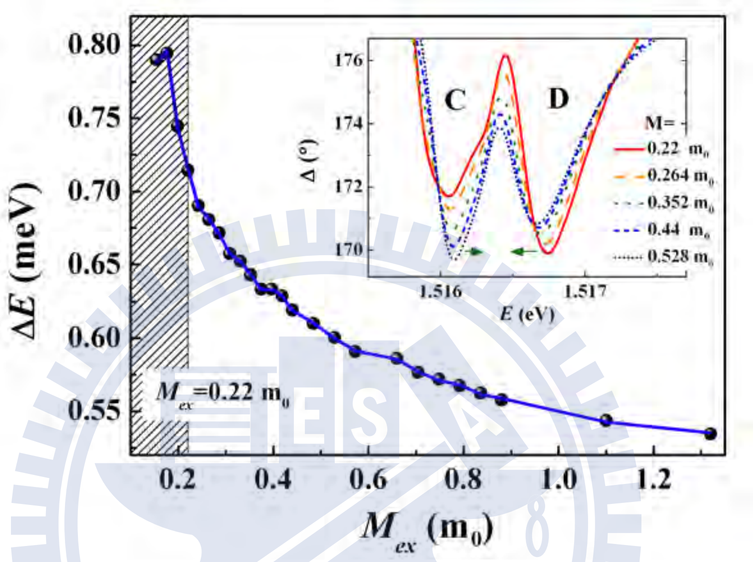

FIGURE 5.6: Calculated energy difference (ΔE) of the dips C and D as a function of exciton effective mass M_{ex} in units of the free electron mass m_0. The inset is the calculated spectra of Δ for different M_{ex}s (0.22 m_0 solid line, 0.264 m_0 dash line, 0.352 m_0 dot line, 0.44 m_0 short-dash line, and 0.528 m_0 short-dot line). The exciton effective mass M_{ex} used in the study at 0 T is 0.22 m_0 [45, 46].

To explain the behaviour of the dips C and D in magnetic fields shown in Fig. 3.6 and considering a large excitonic momentum component perpendicular to the direction of the magnetic field [45, 46], we allow the exciton effective mass to be changed due to the magnetically induced exciton effective mass enhancement effect [45, 46] in the non-local polariton model Eq. (4.29). The separation of the two dips (ΔE) was calculated as a function of the exciton effective mass (M_{ex}) and the result is shown in Fig. 5.6. The calculated Δ spectra for different masses are shown in the inset. It is clear that the shapes of the spectra and the separation between the two dips are modified for various exciton effective masses. And to observe more detailed structures change with various exciton effective masses, we show the spectra of the small damping 0.5 ν in comparison to that of 1 ν with exciton effective masses M_{ex} and $2M_{ex}$ respectively in Fig. 5.7. The detailed fine structures change their relative amplitude when the exciton effective mass is changed.

The reason for the changes of the spectra and ΔE is that the M_{ex} changes the wavevector of the polariton and then influences the interference. The separation ΔE, which decreases first and the decrease becomes moderate as M_{ex} increases, is similar to the behaviour of the measured dips C and D in magnetic fields. The amount of change of the separation ΔE, however, is smaller compared to the experimental result in a reasonable enhancement range of M_{ex} [45, 46]. But, we need to bear in mind that we are facing subtle fine structures in magnetic fields. Some details such as the influences from other exciton levels and microscopic mechanisms may also play a role. Nevertheless, the enhancement of the exciton effective mass gives a plausible explanation to the changes of the ellipsometry spectra under magnetic fields.

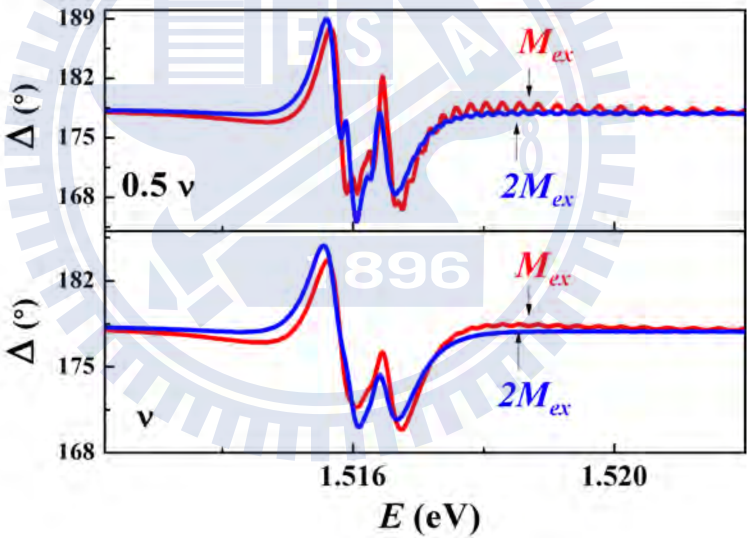

FIGURE 5.7: Calculated Δ spectra for various exciton effective mass M_{ex} and $2M_{ex}$ with different damping ν and 0.5ν.

Chapter 6

Conclusion

6.1 Low Temperature and High Magnetic Field Ellipsometry System

In conclusion, we have demonstrated an ellipsometry system that can be fitted into a long-neck He-dewar with a high-field superconducting magnet. The functionality and the precision of the system were systematically analyzed. Its random error was found to be dominated by the light intensity fluctuation. To demonstrate the system's capability, we have measured the ellipsometry spectra of GaAs samples with and without an epilayer near the band edge in magnetic fields up to 14 Tesla. Fine structures from the high quality GaAs epilayer were clearly observed in the spectra and they varied with the magnetic field. The lower energy dips (A and B) evolved with magnetic fields in a fashion similar to the previous results obtained in Faraday configuration and were identified as the two σ_{-1} magneto-exciton states with the dip B being the bright state and the dip A being the dark state. For the fine structures at higher transitions that have not been reported, we proposed a model taking into account of the non-local polariton with dead layers and Pekar's ABC introduced at the surface and the interface of the epilayer and the substrate. Using the model, we can give a interpretation of the measured ellipsometry spectra, and explain why the fine structures are difficult to be observed at normal-incidence reflectance spectra. To explain the behaviour of the ellipsometry spectra under magnetic fields, we considered the magnetically induced exciton effective mass enhancement effect and introduced it into the spatial dispersive polariton model. The result showed changes of both the shapes and the separation of the dips C and D with various exciton effective mass. The simple model proposed here can predict that the separation of the two dips decreases with increasing magnetic field but failed to match the experimental result quantitatively. The fine structure of the magneto-polariton observed in the ellipsometry spectra is intricate in magnetic fields, and the exact model may require considerations of thorough physical mechanisms in addition to the ones used here. With its unique capability, this system provide us an innovated way to study the magneto-optical response of exciton-polariton in semiconductors under high magnetic fields at low temperatures. We hope that the obtained results and the proposed explanations can be a descriptive bases for further research.

6.2 Recommendations for Future Research

- **Extra Functionality of the Equipment**
  Conducting ellipsometry measurements in low temperatures and high magnetic fields is still very much in the developing stage and more has yet to be done. There is still room for improvements of the accuracy, precision, operation speed, spectra resolution, and additional functions of the instrument. We would recommend for instance using photo-elastic modulators (PEMs) to replace the mechanical rotation elements to reduce the vibration of the long insert. PEMs can be operated very fast and hence can improve the precision by averaging a large mount of measurement data. In addition, the full Muller matrix can be measured once the PEMs and other polarization elements are arranged appropriately [2]. This could extend the applications of the instrument to measure the depolarization of the light reflected from sample at high magnetic fields. And many interesting topics such as the magneto-optical coupling constants and magnetization of material [18, 74, 75], the polarization selection rules for carriers in quantum regimes [76] or for excitons can also be explored using our ellipsometer.

- **Microscopic Theory of Polariton Propagation in Magnetic Field**
  There is a continuing need for an adequate theoretical basis for the polariton propagation in magnetic fields, especially when the configuration is not simply the Voigt ($\mathbf{B} \perp \mathbf{q}_{ex}$) or Farady ($\mathbf{B} \parallel \mathbf{q}_{ex}$) geometries. Although, the

microscopic treatments are free from using ABC approximations, the complexity of the polariton problems limits them to the specific geometry and to further simplifications [10–12]. When the magnetic field induced mixing of other states to the $1s$ state [43, 44] is taking into account, the problem becomes more complicated. And no theoretical works in this direction have been published previously.

- **An Idea to Measure Field-controlled Exciton Effective Mass**
  Despite Butov *et al.* [45, 46] has observed magnetically induced exciton effective mass enhancement by fitting the measured dispersion relation of a magnetoexciton in GaAs double QWs, it does have some limitations. "The dispersions become so flat that the scattering of the experimental points does not allow precise determination of that mass which becomes very large" [45]. Thus, there were just three experimental determined values of exciton effective mass for the magnetic fields smaller than 4 T. But, as our study has demonstrated, more also needs to be determined about the exciton translational effective mass in high magnetic fields.

  We share an idea that might be able to measure exciton effective mass in high magnetic fields. The diagram of the idea is shown in Fig. 6.1. We propose a GaAs wide QW sample structure with length l about 200 $\sim$ 300 nm. The quantization of the exciton CM motion will lead discrete energies

  $$E_n = \frac{\hbar^2 \pi^2 n^2}{2M_{ex} l}. \tag{6.1}$$

  If the quality of the sample is good enough, the discrete energy levels will show clearly in a reflectance spectrum [44]. One can obtain the exciton effective mass from Eq. (6.1) by fitting multi-peaks in the reflectance spectrum. When the magnetic field is applied perpendicular to the exciton CM motion direction, the magnetically induced exciton effective mass enhancement can be obtained. Moreover, if side gates like in Fig. 6.1 can be processed, the effective mass enhancement can be measured as a function of various dipole length of the electron-hole pair, which is controlled by bias voltages.

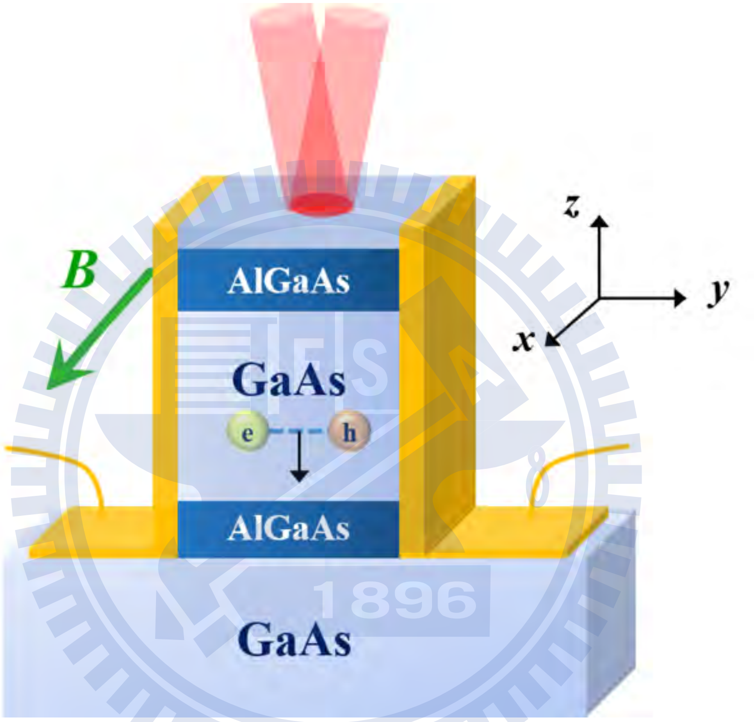

FIGURE 6.1: Diagram of the ideal to measure exciton translational effective mass in various electric and magnetic fields. The circular polarized light is incident in the z direction; the electric field and magnetic field are applied in the y and x directions respectively. That is, the directions of the exciton CM motion, the electric field, and the magnetic field are mutually perpendicular.

Part II

Well-thickness Dependent Electron Transport Effective Mass and Mobility in Low Bandgap Quantum Wells

Chapter 7

Introduction

The electron transport effective mass and the scattering time are the fundamental factors that determine the transport properties of electrons in semiconductor quantum wells (QWs) [77]. The electron effective mass typically becomes larger at higher energies because of the non-parabolic dispersion of the band structure [78]. Thus in QWs, the electron effective mass usually increases as the well width is reduced. Not only that, the reduced well width also causes an increase in the interface roughness scattering (IRS), which dominantly contributes to the degradation of the electron mobility in thin quantum wells [79]. Gold [79] has theoretically predicted that for QWs with large barrier heights (infinite QW model), the electron mobility followed the law $\mu \propto l^6$ (l being the well thickness), which was later confirmed experimentally [80–82]. For QWs with small barrier height, the reduction in mobility is not as drastic as in the infinite QW model , but the mobility still goes down with decreasing well thickness [83].

It would be much more desirable if one could design a QW, which can confine the electrons at higher energies while keeping the mobility high at the same time. Recently, pursuing for higher electron mobility and stronger spin-orbit interaction, more attention is being given to the Sb-based compounds [84–86] for their narrow bandgaps. In this part of the thesis, we discuss the transport properties of QWs at low temperature regime from a theoretical perspective and compare four structures that have different transport properties. To calculate the electron transport effective mass we use the one-band effective Hamiltonian, which includes the non-parabolic dispersion relation for the conduction bands and includes the effects of the barrier properties by considering the distribution of the electron wavefuntion.

It was found that the electron transport effective mass and the confinement energy behave differently depending on the combination of the barrier and the QW materials when the QW thickness is changed. In calculation of the impacts of various scattering mechanisms on the electronic transport characteristics, the first Born approximation was considered. The results indicate that the electron mobility can become higher even when the well thickness is reduced.

Chapter 8

Theory & Calculation Methods

8.1 The Basic Idea

Figure 8.1 illustrates the basic idea of designing a QW that could have smaller transport effective mass when the well thickness is reduced. It is based on a type-II heterostructure, where the electrons are confined in the middle well with the barriers provided by a narrower bandgap semiconductor, which has a smaller electron effective mass. In this structure, when the well width is reduced, the electron wavefunction of the well will penetrate more into the barriers and "feel" a smaller effective mass m_B. However, the electron effective mass of the QW (m_{QW}) will also increase because of the non-parabolic dispersion of the band when the width of the QW is reduced. Is it possible that the wavefunction penetration effect is more serious than the non-parabolic effect to result in a smaller electron transport effective mass ? And, how does it influence the scattering mechanisms and whether a thinner QW can have higher mobility ? In the following, we derive the calculation methods and compare four structures with different well/barrier combinations and demonstrate that it is indeed possible to achieve a lower electron transport effective mass and higher mobility when the well width is reduced.

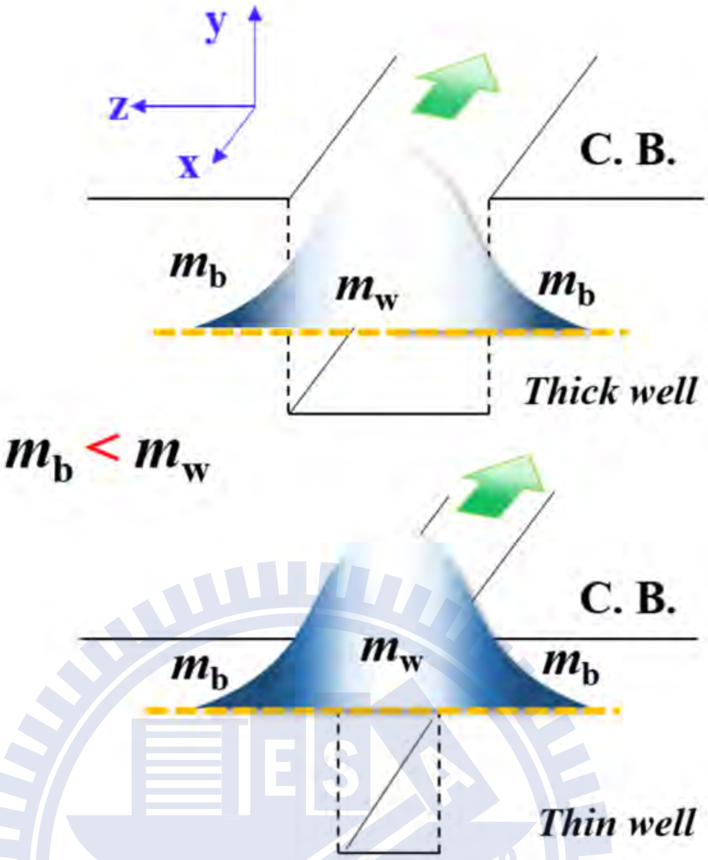

FIGURE 8.1: Conduction band diagram to illustrate the basic idea. The electron wavefunction confined in the z-direction of the thinner well (lower one) penetrates more into the barriers than the thicker well (upper one), and "feels" a smaller effective mass m_B.

8.2 Electron Transport Effective Mass

For 2D degenerated electronic gas[1] in the first Born approximation for elastic scattering, the transport scattering time τ is given by (see e.g. Refs. [79, 83, 87–89])

$$\frac{1}{\tau} = \frac{A}{4\pi^2}\frac{2\pi}{\hbar}\int S_C\,|M|^2\,(1-\cos\theta)\delta(E_k - E_{k'})d^2k'. \tag{8.1}$$

In this equation: k (k') and E_k ($E_{k'}$) stand for the in-plane wave vectors before (after) scattering and the corresponding in-plane components of the electronic energy ($E_k = E_{k'}$ for the elastic scattering); θ denotes the scattering angle between k and k' ; M is the scattering matrix element; A is the sample area; S_C is the screening factor which is given by $[q/(q+q_s)]^2$, where

---

[1] The electrons can move only in the xy plane and are confined in the z-direction; only one lowest sub-band is occupied

$$q = |\mathbf{q}| = |\mathbf{k} - \mathbf{k}'| = \sqrt{2k^2(1-\cos\theta)}, \tag{8.2}$$

for elastic scattering, and

$$q_s = [\frac{me^2}{2\pi\varepsilon\hbar^2}] \int |\varphi(z)|^2 \int |\varphi(z')|^2 \, e^{-q|z-z'|} dz' dz. \tag{8.3}$$

For small q, we use the Thomas-Fermi approximation and the Thomas-Fermi wavevector $q_{\mathrm{TF}} = 2/a^{ex}$, where a^{ex} is the effective Bohr radius in a semiconductor, to replace q_s [83].

Within the conventional approach [87–89] the three-dimensional scattering processes in 2D quantum channels can be described by the effective (adiabatic) 2D Hamiltonian

$$\hat{H}_\rho = \int\limits_{-\infty}^{+\infty} dz \varphi^*(z) \hat{H} \varphi(z), \tag{8.4}$$

where

$$\hat{H} = -\frac{\hbar^2}{2} \nabla_{\mathbf{r}} [\frac{1}{m(E,z)}] \nabla_{\mathbf{r}} + V(z) + V_{sc}(\mathbf{r}), \tag{8.5}$$

is the three-dimensional system Hamiltonian, $\mathbf{r} = \{x, y, z\} \equiv \{\rho, z\}$ is the three-dimensional radius vector, $\nabla_{\mathbf{r}}$ stands for the spatial gradient, $V(z)$ represents the potential profile in the structure along z-direction, $V_{sc}(\mathbf{r})$ stands for the scattering potential, $m(E,z)$ is the energy (E) and position (z) dependent electron effective mass [78, 88],

$$\frac{1}{m(E,z)} = \frac{2P^2}{3\hbar^2} [\frac{2}{E + E_g(z) - V(z)} + \frac{1}{E + E_g(z) - V(z) + \Delta_{so}(z)}], \tag{8.6}$$

where $E_g(z)$ and $\Delta_{so}(z)$ stand for the position dependent bandgap and the spin-orbit splitting in the valence band, and P is the momentum matrix element. The z-component of the envelop wavefunction $\varphi(z)$ represents the solution confined in the QW for the lowest energy subband. The component can be obtained from the appropriate one dimensional non-linear Schrödinger equation:

$$[-\frac{\hbar^2}{2} \frac{d}{dz} \frac{1}{m(E_0,z)} \frac{d}{dz} + V(z)] \varphi(z) = E_0 \varphi(z), \tag{8.7}$$

where E_0 refers to the bottom energy of the first electronic subband in the well. After the averaging (Eq. (8.4)) along the z-direction, the adiabatic quasi-2D

Schrödinger equation (which describes quasi-2D scattering processes) is given by

$$\hat{H}_\rho \psi_k = [-\frac{\hbar^2}{2}\frac{1}{m_t(E)}\nabla_\rho^2 + \widetilde{V}_{sc}(\rho)]\psi_k = E_k\psi_k. \tag{8.8}$$

In this equation, therefore, the electron 2D transport energy dependent effective mass is

$$\begin{aligned} \frac{1}{m_t(E)} &= \int_{-\infty}^{+\infty} dz \varphi^*(z)\frac{1}{m(E,z)}\varphi(z) \qquad (8.9)\\ &= \int_{\mathrm{QW}} \varphi^*(z)\frac{1}{m_{\mathrm{w}}(E)}\varphi(z)dz + \int_{\mathrm{Barrier}} \varphi^*(z)\frac{1}{m_{\mathrm{b}}(E)}\varphi(z)dz, \end{aligned}$$

and

$$\widetilde{V}_{sc}(\rho) = \int_{-\infty}^{+\infty} dz \varphi^*(z)V_{sc}(\mathbf{r})\varphi(z) \tag{8.10}$$

is the quasi-2D scattering potential, $E = E_0 + E_k$, $m_{\mathrm{w}}(E)$ and $m_{\mathrm{b}}(E)$ stand for the electron effective mass at energy E in the QW and barrier regions correspondingly. It is clear from the equations above that the energy dispersion relation and its non-parabolicity for the electrons confined in the well is represented by

$$E = E_0 + \frac{\hbar^2 k^2}{2m_t(E)} \tag{8.11}$$

and, consequently, in a very standard manner, the transport effective mass $m_t(E)$ goes into all simulations of conduction characteristics of electrons in the well (scattering time, mobility, etc.) [79, 83, 87–89].

8.3 Material Parameters

Four different cases representing different combinations of barrier/QW/barrier structures are compared in our simulation: (i) GaAs/ $\mathrm{GaIn_{0.25}As}$/ GaAs, (ii) $\mathrm{GaAsSb_{0.49}}$/ $\mathrm{GaAsSb_{0.22}}$/ $\mathrm{GaAsSb_{0.49}}$, (iii) $\mathrm{InAsSb_{0.25}}$/ InAs/ $\mathrm{InAsSb_{0.25}}$, and (iv) $\mathrm{Ga_{0.3}InSb_{0.9}P}$/ $\mathrm{Ga_{0.2}InSb_{0.8}P}$/ $\mathrm{Ga_{0.3}InSb_{0.9}P}$. The lattice mismatch between the barriers and QWs for these cases is small than 2%. The deformation potential is used to simulate the band parameters and the band lineups $V(z)$ of the strained interfaces [90, 91]. Because of the large separation of L- and X-point to Γ-point of the four cases considered, only the Γ valley is included in the simulation.

Table 8.1: **k·p** band parameters for III-V semiconductors. a_{lc} is the lattice constant, E_g^Γ is the energy gap at Γ-point, m_{e} is the electron effective mass at Γ-point, VBO is the valence band offset, a_c and a_v are the hydrostatic deformation potential for conduction band and valence band respectively, b is the shear deformation potential, ε is the static dielectric constant, and c_{11}, c_{12}, c_{44} are the elastic constants.

parameters	GaAs	InAs	GaSb	AlSb	InSb	InP	GaP
a_{lc} (Å)	5.653	6.058	6.096	6.136	6.479	5.87	5.451
E_g^Γ (eV)	1.519	0.417	0.812	2.386	0.235	1.424	2.886
Δ_{so} (eV)	0.341	0.39	0.76	0.676	0.81	0.108	0.08
$m_{\mathrm{e}}(m_0)$	0.067	0.026	0.039	0.14	0.0135	0.08	0.13
VBO (eV)	-0.80	-0.59	-0.03	-0.41	0	-0.94	-1.27
a_c (eV)	-7.17	-5.08	-7.5	-4.5	-6.94	-6.0	-8.2
a_v (eV)	1.16	1.00	0.8	1.4	0.36	0.6	1.7
b (eV)	-2.0	-1.8	-2.0	-1.35	-2.0	-2.0	-1.6
c_{11} (GPa)	1221	832.9	884.2	876.9	684.7	1011	1405
c_{12} (GPa)	566	452.6	402.6	434.1	373.5	561	620.3
c_{44} (GPa)	600	395.9	432.2	407.6	311.1	456	703.3
ε (static)[92]	12.9	15.15	15.7	12.04	16.8	12.5	11.1

The basic **k·p** band parameters [90] of common III-V semiconductor used in the study are shown in Table 8.1. For ternary alloys, the dependence of the band parameters on alloy composition can be described approximately in the simple form [90]

$$G(\mathrm{A}_{1-\alpha}\mathrm{B}_\alpha) = (1-\alpha)G(\mathrm{A}) + \alpha G(\mathrm{B}) - \alpha(1-\alpha)C, \tag{8.12}$$

where G is either of the band parameters, and C is the bowing parameter accounting for the deviation from a linear-relation between the two binaries A and B. The bowing parameters for several III-V ternary compounds are listed in Table 8.3 [90].

Table 8.2: Bowing parameters for III-V ternary compounds.

parameters	InGaAs	AlGaSb	GaAsSb	InAsSb	InPSb
E_g^Γ (eV)	0.477	$-0.044 + 1.22x$	1.43	0.67	1.9
Δ_{so} (eV)	0.15	0.3	0.6	1.2	0.75
$m_{\mathrm{e}}^*(\Gamma)$	0.0091	0	0	0.035	0
VBO (eV)	-0.38	0	-1.06	0	0
a_c (eV)	2.61	0	0	0	0

For most commonly encountered quaternary compounds of the $A_xB_{1-x}C_yD_{1-y}$ type, we use the method introduced by Glisson *et al.* [90, 93] to derive quaternary alloy band parameters. The parameter

$$
\begin{aligned}
G''_{ABCD}(x,y) &= \frac{x(1-x)[(1-y)G'_{ABD}(x)+yG'_{ABC}(x)]}{x(1-x)+y(1-y)} \\
&+ \frac{y(1-y)[(1-x)G'_{BCD}(y)+xG'_{ACD}(y)]}{x(1-x)+y(1-y)},
\end{aligned}
\tag{8.13}
$$

where the ternary parameters G'_{ABD}, G'_{ABC}, G'_{BCD}, and G'_{ACD} are given by Eq. (8.12).

8.3.1 Strain

The valence-band edge of a strained semiconductor can be written as [90, 91]

$$E_v = \mathrm{VBO} + \frac{\Delta_{\mathrm{so}}}{3} + \Delta E_v^{\mathrm{hy}} + \max(\Delta E_{\mathrm{hh}}^{\mathrm{sh}}, \Delta E_{\mathrm{lh}}^{\mathrm{sh}}), \tag{8.14a}$$

and the conduction-band edge is based on the valence-band position with the form

$$E_c = \mathrm{VBO} + \frac{\Delta_{\mathrm{so}}}{3} + E_g + \Delta E_c^{\mathrm{hy}}. \tag{8.14b}$$

The band shifts are induced by the hydrostatic deformation potential effects ΔE_v^{hy} and ΔE_c^{hy} for the valence-band and the conduction-band correspondingly; and the shear deformation potential effect $\Delta E_{\mathrm{hh}}^{\mathrm{sh}}$ and $\Delta E_{\mathrm{lh}}^{\mathrm{sh}}$ for the heavy-hole and light-hole bands respectively. The energy shifts induced by hydrostatic deformation potential effect are given by

$$\Delta E_v^{\mathrm{hy}} = a_v(2\epsilon_\parallel + \epsilon_\perp) \tag{8.15a}$$

for the valence-band, and

$$\Delta E_c^{\mathrm{hy}} = a_c(2\epsilon_\parallel + \epsilon_\perp) \tag{8.15b}$$

for the conduction-band. $\epsilon_\parallel$ and $\epsilon_\perp$ are the strain tensor components parallel and perpendicular to the plane of the interface :

$$\epsilon_\parallel = \frac{a_\parallel}{a_{\mathrm{lc}}} - 1, \tag{8.15c}$$

and

$$\epsilon_\perp = \frac{a_\perp}{a_{\mathrm{lc}}} - 1 \tag{8.15d}$$

with the deformed lattice constant parallel[2]

$$a_{\parallel} \rightarrow a_0; \tag{8.15e}$$

and perpendicular to the plane of the interface

$$a_{\perp} = a_{\mathrm{lc}}[1 - D_i(\frac{a_{\parallel}}{a_{\mathrm{lc}}})], \tag{8.15f}$$

where a_0 is the lattice constant of the host material (ex. substrate), a_{lc} is the lattice constant when the material is unstrained (bulk value), and the constant D depends on the elastic constants as

$$D_{001} = 2\frac{c_{12}}{c_{11}} \tag{8.15g}$$

for the strain along [001] direction. And the shear deformation potential effect for the strain along [001] direction leads energy shift

$$\Delta E_{\mathrm{hh}}^{\mathrm{sh}} = -\frac{1}{2}\delta E_{001}^{\mathrm{sh}} \tag{8.16a}$$

for the heavy-hole band,

$$\Delta E_{\mathrm{lh}}^{\mathrm{sh}} = -\frac{1}{2}\Delta_{\mathrm{so}} + \frac{1}{4}\delta E_{001}^{\mathrm{sh}} + \frac{1}{2}[\Delta_{\mathrm{so}}^2 + \Delta_{\mathrm{so}}\delta E_{001}^{\mathrm{sh}} + \frac{9}{4}(\delta E_{001}^{\mathrm{sh}})^2]^{1/2} \tag{8.16b}$$

for the light-hole band, and

$$\Delta E_{\mathrm{so}}^{\mathrm{sh}} = \frac{1}{2}\Delta_{\mathrm{so}} + \frac{1}{4}\delta E_{001}^{\mathrm{sh}} - \frac{1}{2}[\Delta_{\mathrm{so}}^2 + \Delta_{\mathrm{so}}\delta E_{001}^{\mathrm{sh}} + \frac{9}{4}(\delta E_{001}^{\mathrm{sh}})^2]^{1/2} \tag{8.16c}$$

for the split-off band. In these equations,

$$\delta E_{001}^{\mathrm{sh}} = 2b(\epsilon_{\perp} - \epsilon_{\parallel}). \tag{8.16d}$$

Values of the deformation potential b for various materials are listed in Table 8.1.

---

[2] When the thickness of the host material is very large.

8.3.2 Parameters of Selected Cases

8.3.2.1 InGaAs system

The band lineup of GaAs/GaIn$_{0.25}$As is shown in Fig. 8.2, and some calculated parameters obtained by the method introduced in 8.3.1. These parameters, demanded to calculate the confinement energy and transport effective mass (see Section 8.2), are listed in Table 8.3.

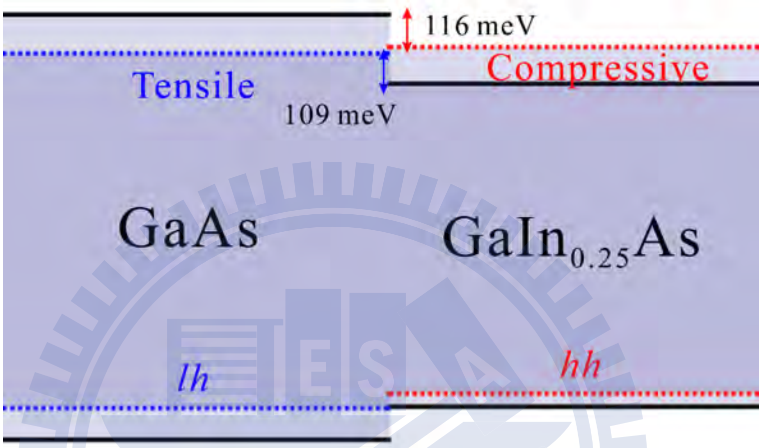

FIGURE 8.2: Band lineup diagram of GaAs/GaIn$_{0.25}$As. Solid lines are unstrained band alignment, and dash lines stand for the alignment being strained. *hh* and *lh* represent heavy-hole and light-hole band respectively. The conduction band discontinuous is 116 meV for the situation of compressive strained well (GaIn$_{0.25}$As), and 109 meV for tensile strained barrier (GaAs).

TABLE 8.3: Parameters of GaAs/GaIn$_{0.25}$As band alignment. The positive and negative signs in front of the percentages in the row a_{lc} represent tensile and compressive strain respectively.

parameters	GaAs(unst.)	GaIn$_{0.25}$As(st.)	GaAs(st.)	GaIn$_{0.25}$As(unst.)
E_g^Γ (eV)	1.519	1.239	1.268	1.154
Δ_{so} (eV)	0.341	0.403	0.476	0.325
$m_{\mathrm{e}}^*(\Gamma)$	0.067	0.0596	0.0578	0.055
ϵ	12.9	13.46	12.9	13.46
a_{lc} (Å)	5.653	5.755(-1.8%)	5.653(1.8%)	5.755
ΔE_c (meV)	116	0	109	0

8.3.2.2 GaAsSb system

For the purpose to choice GaAsSb ternary compound material that can comprise a combination of a smaller electron effective mass barrier and a larger mass well, we show the conduction band edge (Eq. (8.14b)) and electron effective mass for variety Sb concentration x of GaAsSb in different strain situation in Fig. 8.3. In (a) and (b), the $x-$axis is the Sb concentration for the strained-layer, and the $y-$axis is the Sb concentration difference between the unstrained-layer (white mesh) and the strained-layer (black mesh); while the roles of the strained and unstrained layers are in reverse order in (c) and (d). We can find in (a) and (b) that the well is the strained layer with lower concentration and smaller electron effective mass than the barrier (unstrained layer). In (c) and (d), the well is the unstrained-layer and has larger effective mass than the barrier (strained-layer).

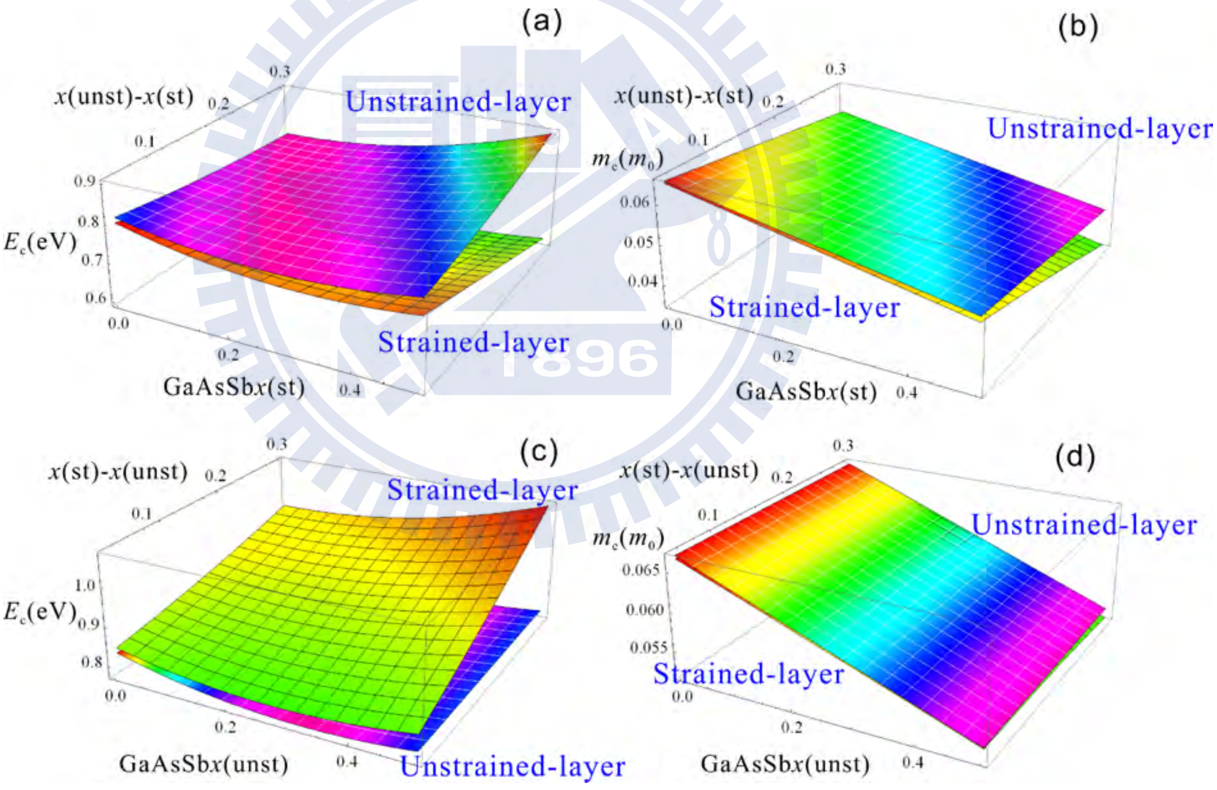

FIGURE 8.3: Conduction band edge E_c (a), (c) and electron effective mass m_e (b), (d) for different Sb concentration x of GaAsSb. “st”and “unst”represent strained and unstrained layers respectively.

Therefore, we choice the combination GaAsSb$_{0.49}$/ GaAsSb$_{0.22}$ as an example, and show the parameters and band lineup of it in Table 8.4 and Fig. 8.4 respectively.

TABLE 8.4: Parameters of GaAsSb$_{0.49}$/ GaAsSb$_{0.22}$ band alignment. The positive and negative signs in front of the percentages in the row a_{lc} represent tensile and compressive strain respectively.

parameters	GaAsSb$_{0.49}$(unst.)	GaAsSb$_{0.22}$(st.)	GaAsSb$_{0.49}$(st.)	GaAsSb$_{0.22}$(unst.)
E_g^{Γ} (eV)	0.815	0.823	0.92	1.118
Δ_{so} (eV)	0.396	0.493	0.488	0.33
$m_{\text{e}}^*(\Gamma)$	0.0533	0.0473	0.0606	0.0608
ϵ	14.27	13.52	14.27	13.52
a_{lc} (Å)	5.87	5.751(2%)	5.87(-2%)	5.751
ΔE_c (meV)	172	0	171	0

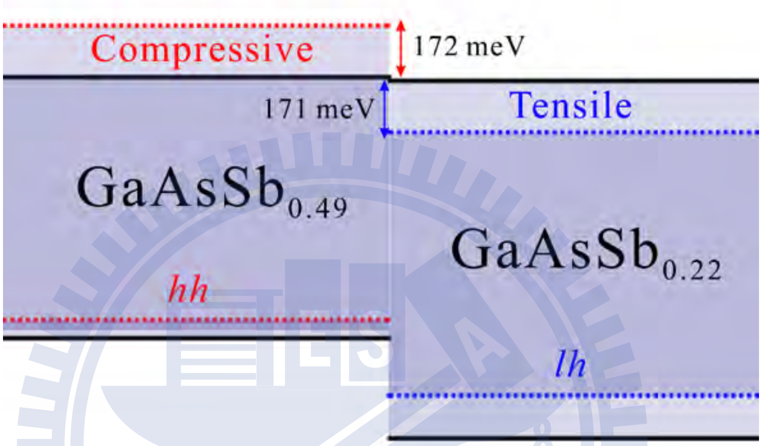

FIGURE 8.4: Band lineup diagram of GaAsSb$_{0.49}$/GaAsSb$_{0.22}$. Solid lines are unstrained band alignment, and dash lines stand for the alignment being strained. *hh* and *lh* represent heavy-hole and light-hole band respectively. The conduction band discontinuous is 172 meV for the situation of tensile strained well (GaAsSb$_{0.22}$), and 171 meV for compressive strained barrier (GaAsSb$_{0.49}$).

8.3.2.3 InAsSb system

Similar to the GaAsSb system discussed in 8.3.2.2, we show the conduction band edge (Eq. 8.14b) and electron effective mass for variety Sb concentration x of InAsSb in different strain situation in Fig. 8.5. However, there exists a region (indicated by an arrow in (a)) that the strained layer with lower Sb concentration has higher conduction band edge E_c , and a region (indicated by an arrow in (b)) that the electron effective mass of the strained layer is larger than the unstrained layer for specific Sb concentrations of strained and unstrained layers. If we want the strain on the well material having larger electron effective mass in comparison to the barrier, we need to choice the difference of the arrow indicated regions in

(b) and in (a). But, for considering reasonable large ΔE_c, we select the combination InAsSb$_{0.25}$/ InAs to be discussed. The parameters and band lineup of the combination are shown in Table 8.5 and Fig. 8.6 respectively. Although, the unstrained InAsSb$_{0.25}$ as a barrier has slightly larger electron effective mass than strained InAs well, we can still achieve our purpose and the results will be shown in Chapter 9.

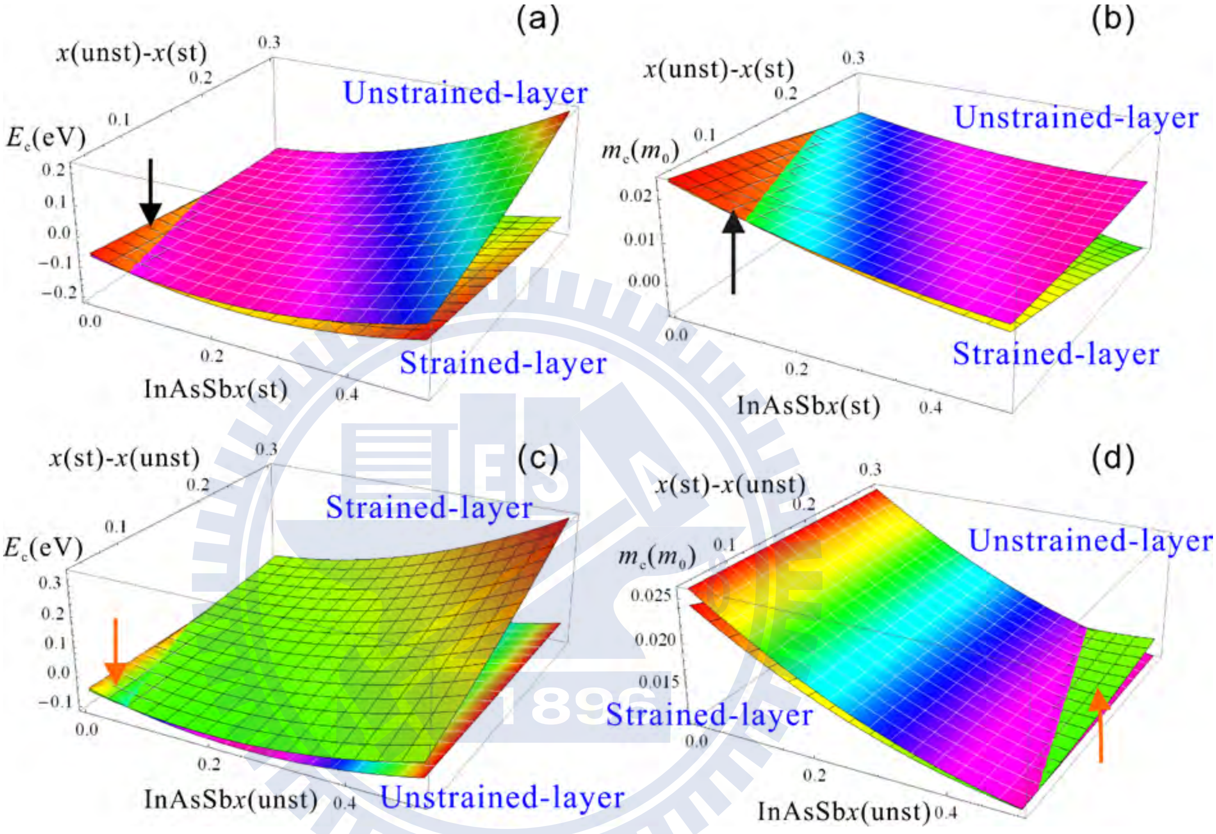

FIGURE 8.5: Conduction band edge E_c (a), (c) and electron effective mass m_e (b), (d) for different Sb concentration x of InAsSb. "st" and "unst"represent strained and unstrained layer. The arrows show the regions with different relative values of strained and unstrained layers in comparison to other regions.

8.3.2.4 GaInPSb system

For quaternary compound material, we have large degree of freedom to select a combination to achieve the purpose. The band lineup and parameters of Ga$_{0.3}$InSb$_{0.9}$P/ Ga$_{0.2}$InSb$_{0.8}$P as an example are shown in Fig. 8.7 and in Table 8.6 respectively. Whether the strain is on the well or on the barrier, the electron effective mass of the barrier is smaller than that of the well (Table 8.6).

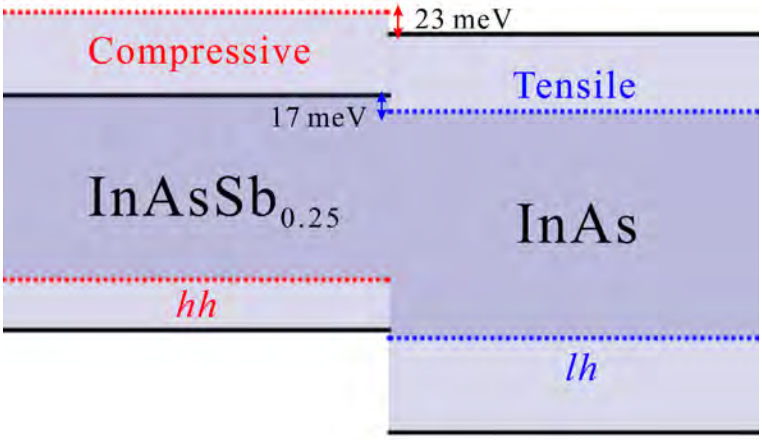

FIGURE 8.6: Band lineup diagram of $InAsSb_{0.25}/InAs$. Solid lines are unstrained band alignment, and dash lines stand for the alignment being strained. *hh* and *lh* represent heavy-hole and light-hole band respectively. The conduction band discontinuous is 17 meV for the situation of tensile strained well (InAs), and 23 meV for compressive strained barrier ($InAsSb_{0.25}$).

TABLE 8.5: Parameters of $InAsSb_{0.25}$/ InAs band alignment. The positive and negative signs in front of the percentages in the row a_{lc} represent tensile and compressive strain respectively.

parameters	$InAsSb_{0.25}$(unst.)	InAs(st.)	$InAsSb_{0.25}$(st.)	InAs(unst.)
E_g^Γ (eV)	0.246	0.237	0.279	0.417
Δ_{so} (eV)	0.27	0.507	0.359	0.39
$m_{\mathrm{e}}^*(\Gamma)$	0.0163	0.0161	0.0188	0.026
ϵ	15.56	15.15	15.56	15.15
a_{lc} (Å)	6.163	6.058(1.7%)	6.163(-1.7%)	6.058
ΔE_c (meV)	17	0	23	0

TABLE 8.6: Parameters of $Ga_{0.3}InSb_{0.9}P$ (Barrier)/ $Ga_{0.2}InSb_{0.8}P$ (Well) band alignment. The positive and negative signs in front of the percentages in the row a_{lc} represent tensile and compressive strain respectively.

parameters	Barrier(unst.)	Well(st.)	Barrier(st.)	Well(unst.)
E_g^Γ (eV)	0.431	0.38	0.444	0.422
Δ_{so} (eV)	0.698	0.624	0.711	0.606
$m_{\mathrm{e}}^*(\Gamma)$	0.0265	0.0287	0.0273	0.0314
ϵ	16.03	15.71	16.03	15.71
a_{lc} (Å)	6.302	6.279(0.4%)	6.302(-0.4%)	6.279
ΔE_c (meV)	158.3	0	159.2	0

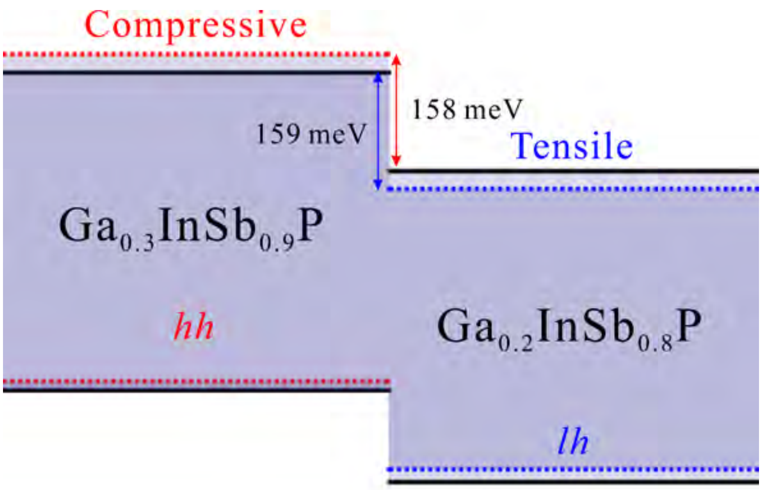

FIGURE 8.7: Band lineup diagram of Ga$_{0.3}$InSb$_{0.9}$P/Ga$_{0.2}$InSb$_{0.8}$P. Solid lines are unstrained band alignment, and dash lines stand for the alignment being strained. *hh* and *lh* represent heavy-hole and light-hole band respectively. The conduction band discontinuous is 158 meV for the situation of tensile strained well (Ga$_{0.2}$InSb$_{0.8}$P), and 159 meV for compressive strained barrier (Ga$_{0.3}$InSb$_{0.9}$P).

8.4 Scattering Mechanisms

In this work we study the low temperature regime based on the first Born approximation (Eq. (8.1)) when scattering mechanisms depending on the well thickness are taken into consideration [79, 83]. The scattering mechanisms considered are interface roughness scattering (8.4.1), alloy disorder scattering (8.4.2), and ionized impurity scattering (8.4.3).

8.4.1 Interface Roughness Scattering (IRS)

The interface roughness causes a modification in the well width and can be expressed as [80, 87]

$$\langle \Delta(\mathbf{r})\Delta(\mathbf{r}')\rangle = \Delta_r^2 \exp(-\frac{|\mathbf{r}-\mathbf{r}'|^2}{\Lambda_r^2}), \tag{8.17}$$

where $\langle ... \rangle$ represents an average, Δ_r stands for the mean height of roughness, and Λ_r is the correlation length of the Gaussion fluctuation. The well width modification leads a energy fluctuation

$$\delta E(\mathbf{r}) = \frac{\partial E}{\partial l}\Delta_r(\mathbf{r}). \tag{8.18}$$

Thus the square of the matrix element from k state to k' state can be expressed as [79, 83, 94]

$$|M|^2 = \frac{\pi\Delta_r^2\Lambda_r^2}{A}(\frac{\partial E}{\partial l})^2\exp(-\frac{\Lambda_r^2 q^2}{4}), \tag{8.19}$$

and the transport relaxation time τ form Eq. (8.1) is given by[3]

$$\begin{aligned} \frac{1}{\tau} &= \frac{\Delta_r^2\Lambda_r^2}{2\hbar}(\frac{\partial E}{\partial l})^2\int S_C\exp(-\frac{\Lambda_r^2 q^2}{4})(1-\cos\theta)\delta(E_k - E_{k'})d^2k' && \text{(8.20a)} \\ &= \frac{m_t(E)\Delta_r^2\Lambda_r^2}{2\hbar^3}(\frac{\partial E}{\partial l})^2 F(\Lambda_r, k), && \text{(8.20b)} \end{aligned}$$

where

$$F(\Lambda_r, k) = \int_0^{2\pi} S_C\exp[\frac{-\Lambda_r^2 k^2(1-\cos\theta)}{2}](1-\cos\theta)d\theta. \tag{8.20c}$$

8.4.2 Alloy Disorder Scattering (ADS)

The random potential of the alloy disorder scattering is expressed as [83]

$$\langle|U_{\text{alloy}}(q)|^2\rangle = \frac{1}{A}\Omega\alpha(1-\alpha)(\Delta V)^2\int_{\text{alloy}}|\varphi(z)|^4\,dz. \tag{8.21}$$

Substituting Eq. (8.21) into Eq. (8.1) for $|M|^2$ yields

$$\frac{1}{\tau} = \frac{m_t(E)}{2\pi\hbar^3}\Omega\alpha(1-\alpha)(\Delta V)^2\int_{\text{alloy}}dz\,|\varphi(z)|^4\int_0^{2\pi}S_C(1-\cos\theta)d\theta. \tag{8.22}$$

In the equation, Ω stands for the volume of the alloy primitive unit cell[4], α is the concentration of the alloy $\mathrm{A}_\alpha\mathrm{B}_{1-\alpha}\mathrm{C}$, and ΔV is the conduction band energy difference between AC and BC. For quaternary compounds, we use

$$\begin{aligned} & \frac{x(1-x)[(1-y)(\Delta V_{ABD}(x))^2 + y(\Delta V_{ABC}(x))^2]}{x(1-x)+y(1-y)} \\ + \; & \frac{y(1-y)[(1-x)(\Delta V_{BCD}(y))^2 + x(\Delta V_{ACD}(y))^2]}{x(1-x)+y(1-y)}. \end{aligned} \tag{8.23}$$

through Eq. (8.13) to replace $\alpha(1-\alpha)(\Delta V)^2$ in Eq. (8.22).

---

[3] We change the variable: $d^2k' \rightarrow k'dk'd\theta \rightarrow k'(dE'/dk')^{-1}dE'd\theta$, and use the dispersion relation (Eq. 8.11).

[4] It has one quarter the volume of the conventional cubic cell for face-centered cubic Bravais lattice.

8.4.3 Ionized Impurity Scattering

The random potential for Coulomb scattering is [79, 83, 94]

$$\langle| U(q)|^2\rangle = (\frac{e^2}{2\varepsilon\varepsilon_0 q})^2 \int n_i(z)F(q,z)^2 dz, \tag{8.24a}$$

where

$$F(q,z) = \int |\varphi(z')|^2 \, e^{-q|z-z'|} dz', \tag{8.24b}$$

$n_i(z)$ is the impurity concentration, and ε is the dielectric constant of the host material. If there is a 2D sheet impurity[5] with density N_i located at a distance z_i from the boundary of a QW (see Fig. 9.7), the random potential (Eq. (8.24a)) becomes

$$\langle| U(q)|^2\rangle = (\frac{e^2}{2\varepsilon\varepsilon_0 q})^2 N_i F(q,z_i)^2. \tag{8.24c}$$

For background impurity scattering (BIS), we assume the background impurity concentration is a constant N_B inside and outside the QW. The electron scattering time satisfies

$$\frac{1}{\tau} = \frac{m_t(E)}{2\hbar^3} \int_0^{2\pi} (\frac{e^2}{2\varepsilon\varepsilon_0 q})^2 N_B S_C (1-\cos\theta) F(q,z_i)^2 d\theta. \tag{8.24d}$$

The electron scattering time τ and mobility $\mu = e\tau/m_t$ determined by these mechanisms can be obtained using the rectangular finite barrier QW model [83] with a mismatch in the effective mass at the heterojunctions [78, 95] (see Appendix D). In our calculation, we assume that all the scattering events are involved with the electrons only at the Fermi-level, and independent of temperatures.

---

[5] In usual, it is called remote impurity and is doped on purpose.

Chapter 9

Results & Discussion

In Figs. 9.1 to 9.4 we present the calculated electron transport effective mass m_t, the confinement energy E_0, and the electron transport mobility μ of the four selective cases as functions of the QW thickness l . The scattering mechanisms including interface roughness scattering, alloy disorder scattering, and impurity scattering (Section 8.4) are applied to calculate the transport scattering time τ.

9.1 Electron Transport Effective Mass

For the case (i) in Fig. 9.1, where the structure is formed by a type-I heterojunction (Fig. 8.2), both the effective mass and the confinement energy increase as the well thickness is reduced whether the strain is on the well (Fig. 9.1 (a)) or on the barrier (Fig. 9.1 (c)). In contrast, the cases (ii), (iii) and (iv), which are type-II band alignments, behave differently. For the strained barrier situation of the case (ii) as shown in Fig. 9.2 (c), the electron transport effective mass has a well recognized maximum when the thickness of the QW is close to 5 nm. The cases (iii) and (iv), even more, show totally opposite dependencies of the electron transport effective mass and the confinement energy on the QW thickness regardless of strained well or strained barrier. While the confinement energy increases as expected, the electron transport effective mass, however, becomes smaller for thinner well thickness.

The dependencies between the electron transport effective mass and the confinement energy of the different cases rely on how the QWs are constructed. In the case (i), and all other type-I band lineups, which the bandgaps of the barriers are

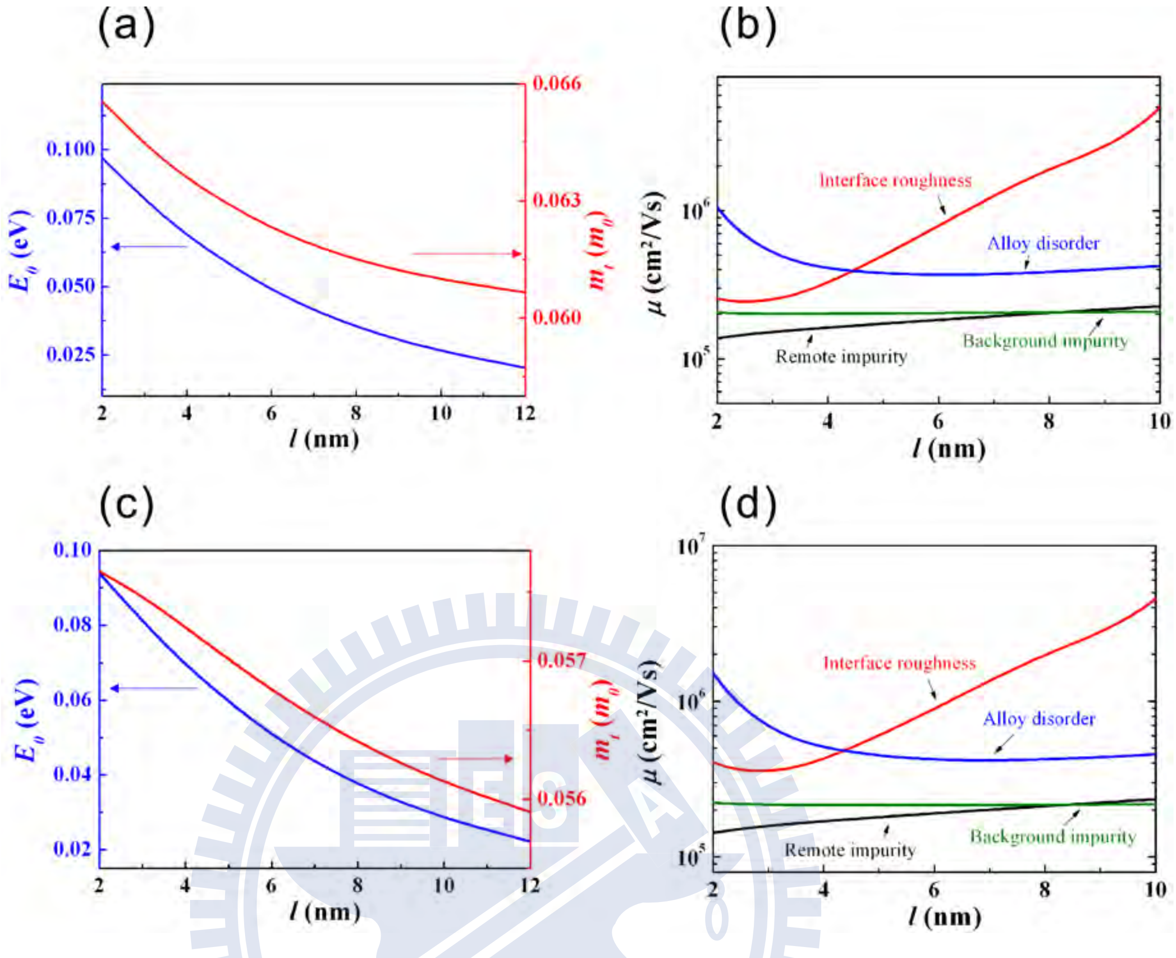

FIGURE 9.1: Calculation results of the electron transport effective mass m_t, the confinement energy E_0, and the transport mobility μ as functions of the well width l for the strain on the well (a), (b) and on the barrier (c), (d) of the case GaAs/GaIn$_{0.25}$As. The used parameters: the background impurity concentration $N_B = 1 \times 10^{15}\text{cm}^{-3}$, the remote delta doping concentration $N_i = 3 \times 10^{10}\text{cm}^{-2}$ at a distance 20 nm below the lower edge of the well, the electron density in the channel $n_0 = N_i$, and the interface roughness parameters $\Delta_r = 0.1$ nm, and $\Lambda_r = 15$ nm [96].

larger than that of the wells, the electron effective mass in the barrier regions is larger than that in the QWs. Both the effects of the band non-parabolicity (Eq. (8.6)) and the wavefunction penetrating into the barriers (Eq. (8.9)) result in an increase of the electron transport effective mass as the QW thickness is reduced. However, for the cases that the electron effective mass of the barrier is smaller than or comparable to that of the QW; when the well thickness is reduced, although the non-parabolicity effect will cause the electron transport effective mass to increase, the increasing of wavefunction penetration into the barriers will lead to the electron transport effective mass to decrease. The competition of the two mechanisms can be seen clearly in the cases (ii), (iii), and (iv). In the strained

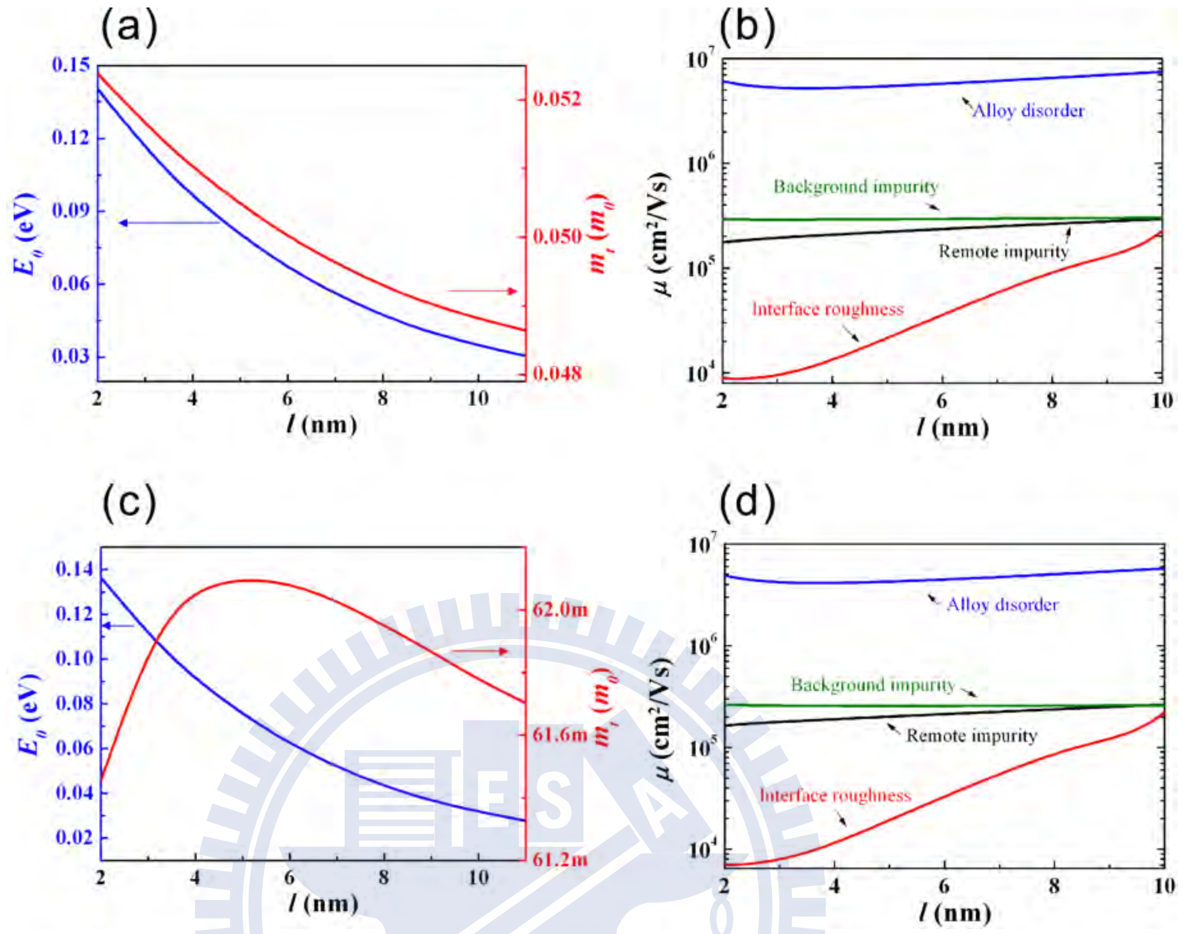

FIGURE 9.2: Calculation results of the electron transport effective mass m_t, the confinement energy E_0, and the transport mobility μ as functions of the well width l for the strain on the well (a), (b) and on the barrier (c), (d) of the case GaAsSb$_{0.49}$/GaAsSb$_{0.22}$. The used parameters: the background impurity concentration $N_B = 1 \times 10^{15}\text{cm}^{-3}$, the remote delta doping concentration $N_i = 4 \times 10^{10}\text{cm}^{-2}$ at a distance 20 nm below the lower edge of the well, the electron density in the channel $n_0 = N_i$, and the interface roughness parameters $\Delta_r = 0.3$ nm, and $\Lambda_r = 20$ nm [97].

barrier situation of the case (ii), the electron transport effective mass has a maximum in its dependence on the well width. The 0.17 eV conduction band offset and not very small electron effective mass of GaAsSb$_{0.22}$ (Table 8.4) contribute to strong localized electrons. In addition, the effective mass difference between the well and the barrier in this case is small compared to the case (iv). These lead to a smaller influence of the barriers than that of the non-parabolicity effect when the QW thickness is larger than 5 nm. However, when the QW thickness is further reduced, the contribution from the small mass barriers becomes stronger than the non-parabolicity effect. As a result, the electron transport effective mass begins to go down. In contrast, although the barrier effective mass is slightly larger than well

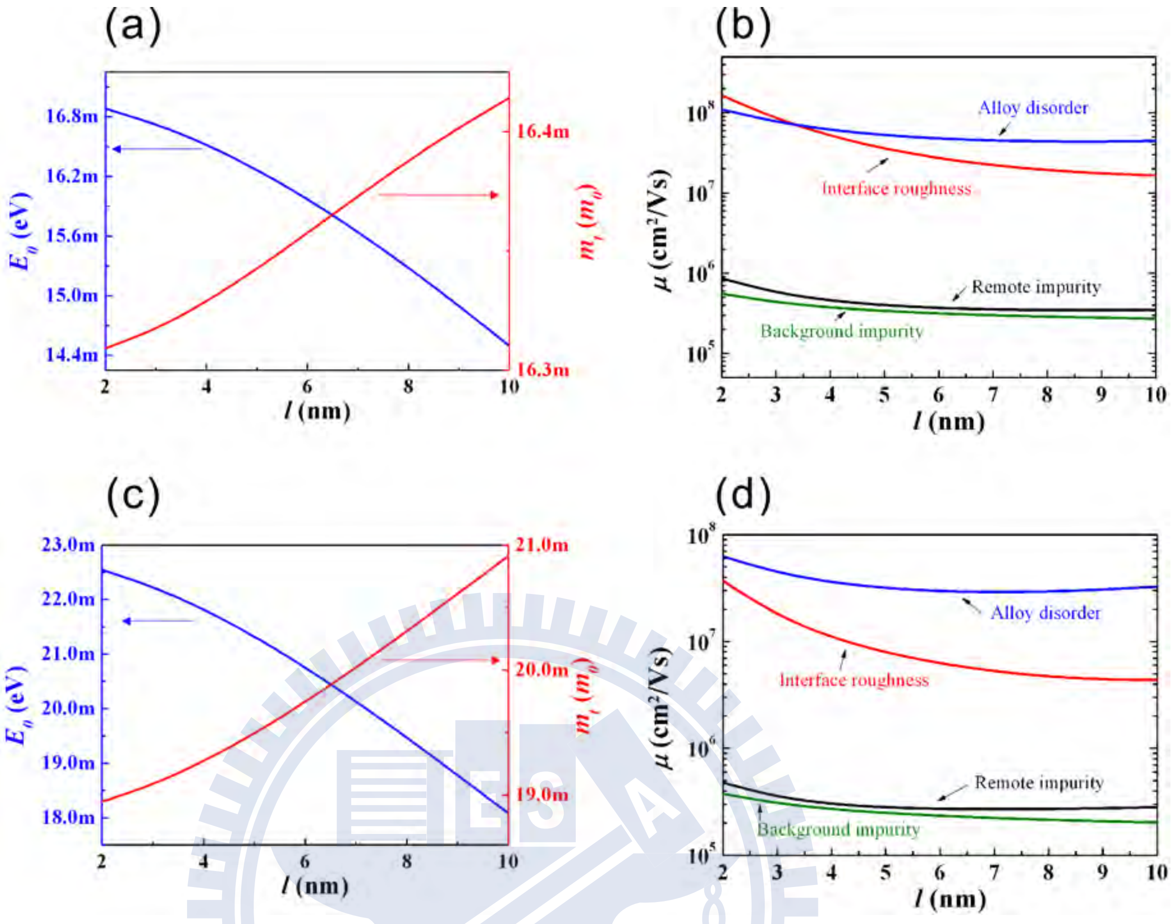

FIGURE 9.3: Calculation results of the electron transport effective mass m_t, the confinement energy E_0, and the transport mobility μ as functions of the well width l for the strain on the well (a), (b) and on the barrier (c), (d) of the case InAsSb$_{0.25}$/InAs. The used parameters: the background impurity concentration $N_B = 1 \times 10^{15}\text{cm}^{-3}$, the remote delta doping concentration $N_i = 1 \times 10^{10}\text{cm}^{-2}$ at a distance 20 nm below the lower edge of the well, the electron density in the channel $n_0 = N_i$, and the interface roughness parameters $\Delta_r = 0.68$ nm, and $\Lambda_r = 20$ nm [98].

effective mass in the strained well situation of the case (iii), the electron transport effective mass goes down continuously for the well thickness less than 10 nm. For the very low bandgap material, because of the strong non-parabolicity effect, the electron effective mass of the well becomes larger than the barrier effective mass even for a small confined energy. This together with the very small effective mass (0.0161 m_0) of the electron and the shallow confinement of the barrier give rise to a dominant contribution from the penetration effect. In short, if type-II QWs are properly designed, the penetration effect of the electron wavefunction can become dominant and bring about a situation that the electron transport effective mass goes down while the confinement energy goes up in thin QWs.

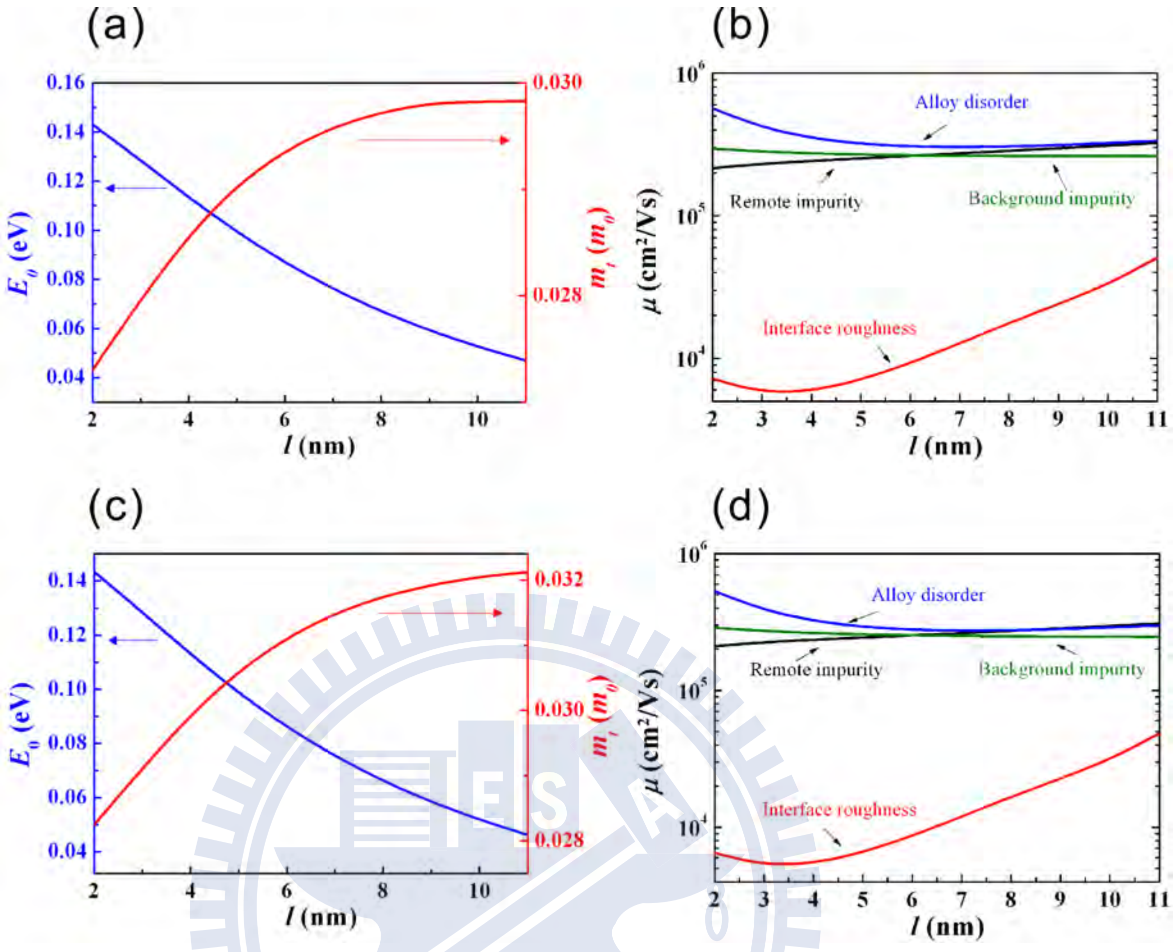

FIGURE 9.4: Calculation results of the electron transport effective mass m_t, the confinement energy E_0, and the transport mobility μ as functions of the well width l for the strain on the well (a), (b) and on the barrier (c), (d) of the case $Ga_{0.3}InSb_{0.9}P/Ga_{0.2}InSb_{0.8}P$. The used parameters: the background impurity concentration $N_B = 1 \times 10^{15}\mathrm{cm}^{-3}$, the remote delta doping concentration $N_i = 1 \times 10^{11}\mathrm{cm}^{-2}$ at a distance 20 nm below the lower edge of the well, the electron density in the channel $n_0 = N_i$, and the interface roughness parameters $\Delta_r = 0.68$ nm, and $\Lambda_r = 20$ nm [98].

9.2 Electron Transport Mobility

The electron transport in semiconductors depends not only on the transport effective mass m_t but also on the scattering time τ. For thin QWs, the various scattering mechanisms except for the background impurity scattering are usually high correlation functions of the well thickness. Using Eqs. (8.20), (8.22), and (8.24), we calculated the scattering times for IRS, ADS, BIS, and remote impurity scattering (RIS), and then calculated the mobility contributed by these mechanisms as a function of the QW thickness respectively. The electron transport effective mass obtained from Section 9.1 also enters the scattering time calculation due to the use of the E-k relationship (8.11) in the integral (8.1). In our simulations of the electron mobility, the carrier density n_0 is set such that the Fermi-level is $\sim$1 meV above the bottom energy of the first electronic sub-band in the well. And we assume that the concentration of the remote delta doping N_i is the same as n_0. Because the experimental data of the interface roughness parameters for some of the cases in our calculation is not available in the literatures so far, we use the parameters of similar combinations of materials in Refs. [96–98]. It should be mentioned that the tendency of the mobility to the QW thickness is not influenced by using different roughness parameters for IRS calculations.

Figures 9.1 to 9.4 show the calculated mobilities caused by different scattering mechanisms as functions of the QW thickness l for the strained well (in (b)) and barrier (in (d)) situations of the four cases respectively. We can find that, for the thin QWs in the cases (i), (ii), and (iv), the interface roughness scattering (IRS) is strongly correlated to the well thickness similar to the previously published results that the electron mobility goes down as the QW thickness decreases [83]. It is, however, possible, as in the case (iii), the mobilities due to the four different mechanisms increase when the QW thickness is reduced.

The reason that the mobility determined by IRS increases as the QW thickness decreases is the scattering time (Eq. (8.20)) at the Fermi-energy inversely proportional to the transport effective mass m_t and the squared differential of the energy to the QW thickness $(\partial E/\partial l)^2$. Figure 9.5 shows the amplitude of the differential $|\partial E_0/\partial l|$ as a function of the QW thickness l for the four different cases. The amplitude of the derivative $|\partial E_0/\partial l|$ (see Eq. (D.6)) is a complex function of the material parameters such as the band discontinuity (V_0), the electron effective mass of the barrier and well (m_B and m_{QW}), and their differentiation etc. The distinctive band lineup constructed by a proper conduction band discontinuity with small electron effective mass of the barrier and the well of the case (iii) result in a decrease of the derivative $|\partial E_0/\partial l|$ with reducing well thickness. Therefore, as the QW thickness decreases, the transport scattering time and mobility determined by IRS increase.

Not only that, the mobility determined by the alloy disorder scattering (ADS) also increases as the well thickness deceases in the case (iii). It seems to know intuitively that the scattering should be stronger when more electron wavefunction penetrates into a region constructed by an alloy. However, we need to keep in mind that

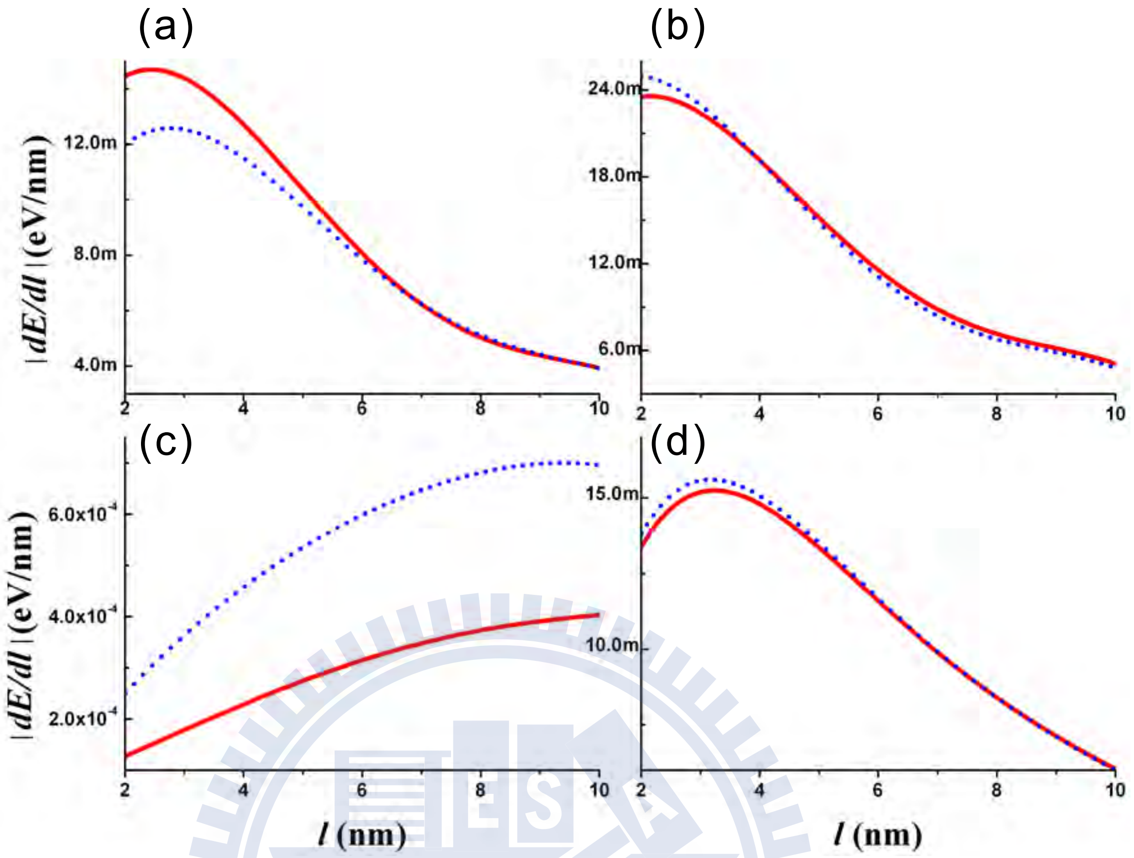

FIGURE 9.5: Absolute value of the differentiation of the energy to the QW thickness for the cases (i) (a), (ii) (b), (iii) (c), and (iv) (d) in the strained well (solid line) and strained barrier (dot line) situations.

the alloy disorder scattering time is determined by $\int_{\text{alloy}} |\varphi(z)|^4 \, dz$ in Eq. (8.22). Therefore, we show the results of the integrations $\int |\varphi(z)|^2 \, dz$ and $\int |\varphi(z)|^4 \, dz$ in the barrier and well regions of the cases (ii) and (iii) in Fig. 9.6. Figure 9.6 shows that $\int |\varphi(z)|^4 \, dz$ is not just proportional to $\int |\varphi(z)|^2 \, dz$. In Fig. 9.6 (b), the integration $\int |\varphi(z)|^4 \, dz$ in the well increases as the well thickness decreases for the thickness $5 \sim 11$ nm, although the probability of finding the electron ($\int |\varphi(z)|^2 \, dz$) in the QW is reduced when the well thickness decreases in Fig. 9.6 (a). On the other hand, in Fig. 9.6 (d), although the probability of finding the electron ($\int |\varphi(z)|^2 \, dz$)) in the barrier increases when the well thickness decreases (Fig. 9.6 (c)), the integration $\int |\varphi(z)|^4 \, dz$ in the barrier becomes smaller as the well thickness decreases (Fig. 9.6 (d)). The integration $\int |\varphi(z)|^4 \, dz$ determines the degree of localization of a wavefunction. For the case of $\text{InAsSb}_{0.25}/\text{InAs}$, the spreading of the wavefunction in the barrier region becomes more serious ($\int |\varphi(z)|^4 \, dz$ decreases) for thinner well thickness. The random potential of the disordered alloy, hence, is "diluted" for a spreading wavefunction compared to a

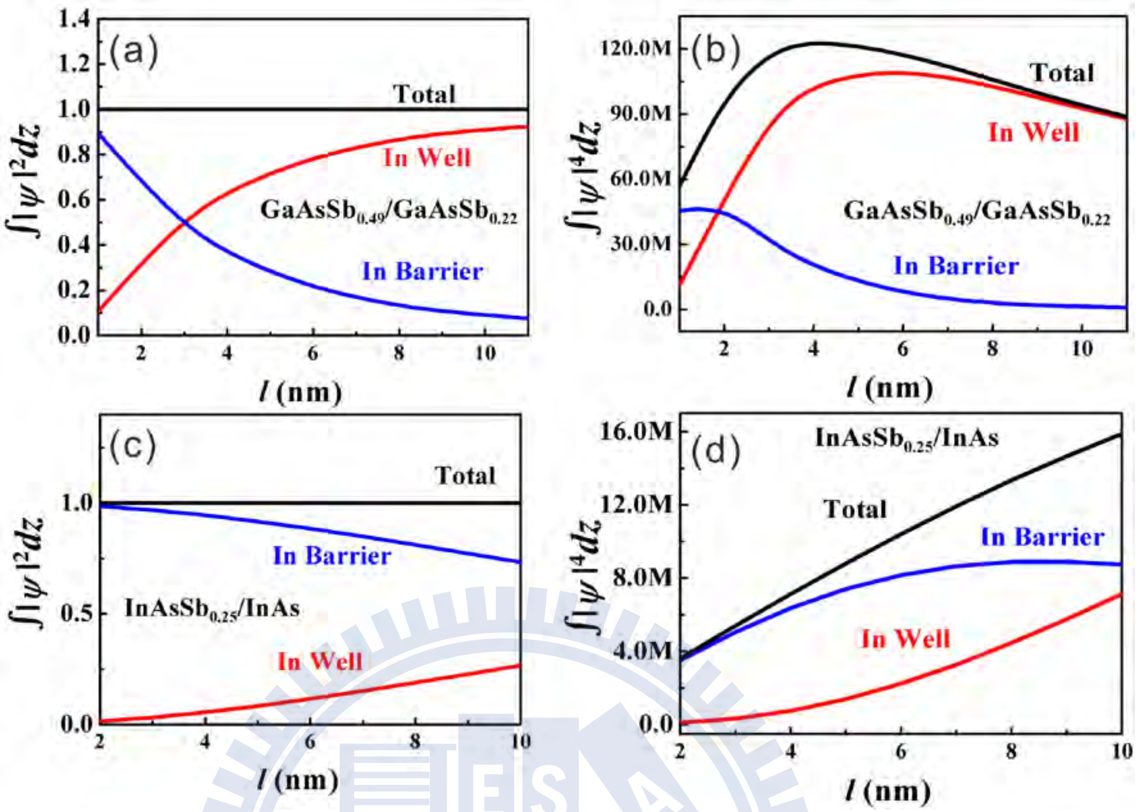

FIGURE 9.6: Integration of the wavefunction absolute value square $\int |\psi|^2 \, dz$ and to the fourth $\int |\psi|^4 \, dz$ of GaAsSb$_{0.49}$/GaAsSb$_{0.22}$ (a), (b) and InAsSb$_{0.25}$/InAs (c), (d) in the strained well situation respectively.

localized wavefunction. This gives rise to a increase of ADS determined mobility even for a larger probability of finding electrons in a alloy region when the well thickness decreases.

For the remote impurity scattering (RIS), the mobility is determined by the Coulomb interaction between the transport carriers and doping impurities, i.e. by the average distance between them. Thus, in usual, RIS determined mobility will decrease as the QW thickness decreases[1] such as in the cases (i), (ii), and (iv). But, in the case (iii), the result is opposite. To illustrate the special case, we show the diagram of the electron wavefunction and the mobility determined by RIS with different doping distance z_i of the case (iii) in Fig. 9.7. The diagram in (a) can illustrate that a lot of wavefunction in this case penetrates into the barrier even for the 10 nm thickness well, and it expands rapidly when the well thickness deceases. If the delta remote impurity is doped near the well, the expanding wavefunction becomes far from the doping instead of close to it like in usual cases when the

---

[1] The distance between the remote doping and the boundary of the QW remains the same.

QW thickness is reduced. However, when the delta doping is situated away from the QW, the mobility behaves more like in the cases (i), (ii), and (iv). This can be clearly seen in Fig. 9.7 (b) showing the dependency of the mobility to the well thickness gradually modified when the doping distance z_i is changed from 10 nm to 80 nm. Hence, in this case, the tendency of RIS determined mobility to the QW thickness is dependent on the doping distance z_i.

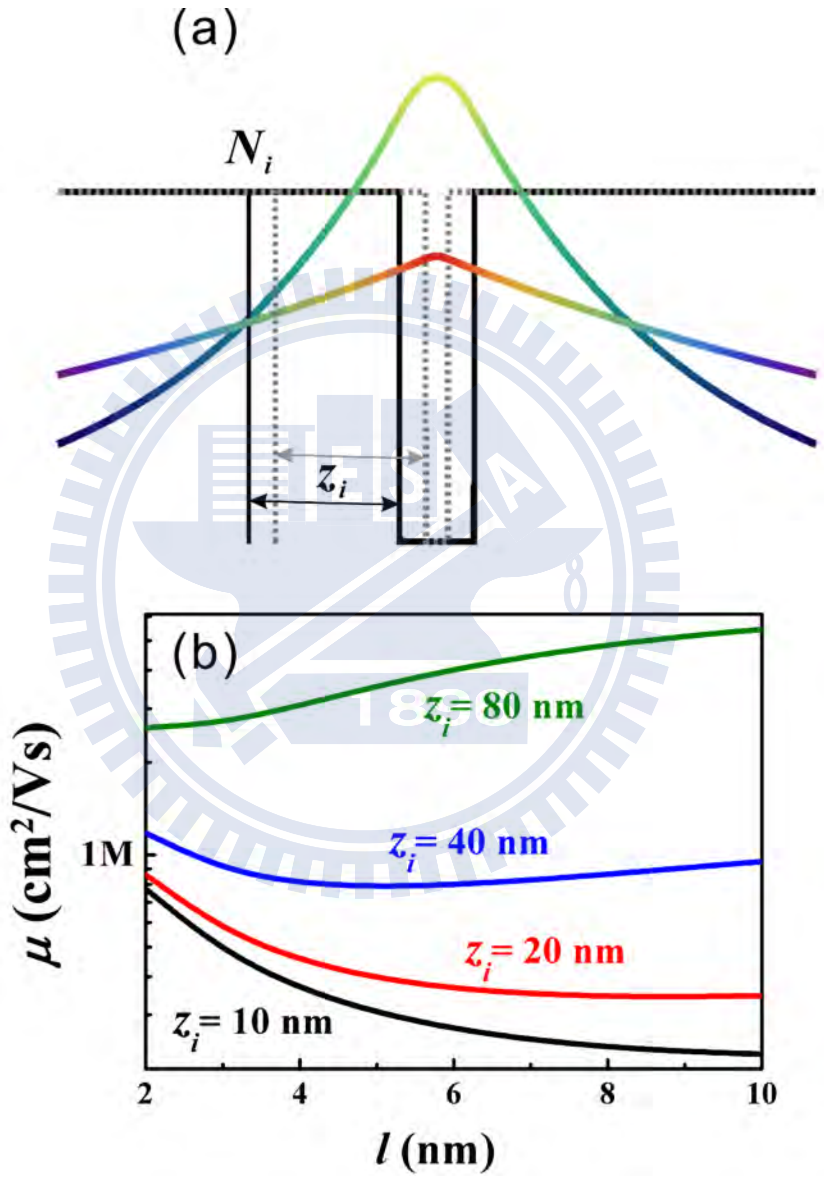

FIGURE 9.7: (a) Illustration diagram of the electron wavefunction for the well thickness 10 nm and 2 nm. (b) Mobility determined by the remote impurity scattering as functions of the well thickness for the distance of the delta doping to the bottom of the QW z_i =10 nm, 20 nm, 40nm, and 80nm of InAsSb$_{0.25}$/InAs in the strained well situation.

Chapter 10

Conclusion

10.1 Well-thickness Dependent Electron Transport Effective Mass and Mobility

In conclusion, we presented theoretical results on the transport property of quantum wells at zero temperature. We processed a method to simulate the quantum well electron transport effective mass including both the band nonparabolicity and spread wavefunction effects especially for low bandgap materials. Four mechanisms including the interface roughness, alloy disorder, background impurity, and remote impurity scatterings were used to determine the electron transport mobility. With a proper combination of barrier and well materials in a type-II heterostructure, we managed to achieve the “inverse”transport properties that the electron transport effective mass decreases and the mobility increases as the well thickness decreases. Although our simulation was performed at the low temperature limit, the results can be potentially useful for further device applications.

10.2 Recommendations for Future Research

Based on the calculation results of this study, further research on measuring the effective mass and mobility of electrons in QWs is therefore warranted. We suggest to perform experiments such as the Hall and Shubnikov de Haas oscillation measurements [99] on the InAsSb/InAs system at low temperatures. Although the measured result is not exactly the “transport” effective mass and mobility, it is worthy to obtained the tendency of theses measured properties to the QW thickness.

Appendix A

Kerr Measurement & Generalized Ellipsometry

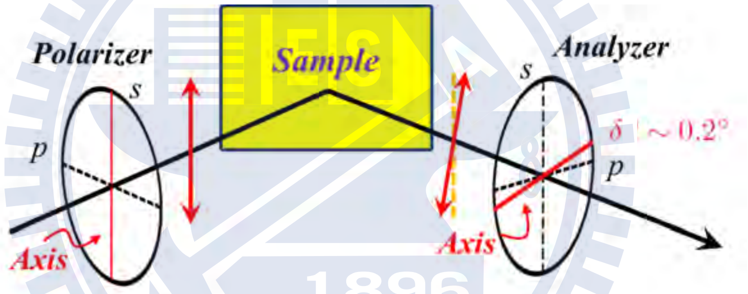

FIGURE A.1: Diagram of the Kerr measurement.

The complex amplitude of the reflected electric field after a analyzer with a azimuthal angle A can be expressed as

$$\begin{aligned} E_A &= \begin{pmatrix} 1 & 0 \\ 0 & 0 \end{pmatrix} \begin{pmatrix} \cos A & \sin A \\ -\sin A & \cos A \end{pmatrix} \begin{pmatrix} r_{pp} & r_{sp} \\ r_{ps} & r_{ss} \end{pmatrix} \begin{pmatrix} \cos \Pi \\ \sin \Pi \end{pmatrix} E_{in} \\ &= E_{in} r_{ss} \cos \Pi [(R_{pp} + R_{sp} \tan \Pi) \cos A + (R_{ps} + \tan \Pi) \sin A]. \end{aligned} \tag{A.1}$$

Where E_{in} is the complex amplitude of the electric field before a polarizer and other quantities are defined as in Section 2.2. Taking the square of the absolute value of (A.1), The measured intensity of the light after an analyzer is

$$\begin{aligned} I(A) &= |E_{in}|^2 |r_{ss}|^2 \cos^2 \Pi \, |(R_{pp} + R_{sp} \tan \Pi) \cos A + (R_{ps} + \tan \Pi) \sin A|^2 \\ &= I_0 (1 + \alpha \cos 2A + \beta \sin 2A), \end{aligned} \tag{A.2}$$

where

$$\alpha = \frac{|R_{pp} + R_{sp}\tan\Pi|^2 - |R_{ps}R_{pp} + \tan\Pi|^2}{|R_{pp} + R_{sp}\tan\Pi|^2 + |R_{ps}R_{pp} + \tan\Pi|^2}, \tag{A.3a}$$

and

$$\beta = \frac{2Re\{(R_{pp} + R_{sp}\tan\Pi)(R_{sp}R_{pp} + \tan\Pi)\}}{|R_{pp} + R_{sp}\tan\Pi|^2 + |R_{ps}R_{pp} + \tan\Pi|^2}. \tag{A.3b}$$

To measure R_{sp} and R_{ps}, we can choose several polarizer azimuthal settings Π [16, 53] or use the experimental set up in Fig. A.1, which is similar to the Kerr measurement [100]. The p- and s- components of the electric field after the analyzer (E_A^p, E_A^s) and the polarizer (E_P^p, E_P^s) can be related by

$$\begin{pmatrix} E_A^p \\ E_A^s \end{pmatrix} = \begin{pmatrix} r_{pp} & r_{sp} \\ r_{ps} & r_{ss} \end{pmatrix} \begin{pmatrix} E_P^p \\ E_P^s \end{pmatrix}. \tag{A.4}$$

If we let $E_P^p = 0$, i.e. only s- component is incident to the sample, Eq. (A.4) becomes

$$\begin{pmatrix} E_A^p \\ E_A^s \end{pmatrix} = \begin{pmatrix} r_{sp}E_P^s \\ r_{ss}E_P^s \end{pmatrix}. \tag{A.5}$$

Takeing the ratio of the two components of the vector in Eq. (A.5), we obtain

$$\frac{E_A^p}{E_A^s} = \frac{r_{sp}}{r_{ss}} = R_{sp} = \phi_s' + i\phi_s'', \tag{A.6}$$

where ϕ_s' and ϕ_s'' are usually called Kerr rotation and ellipticity. Thus, to obtain ϕ_s' and ϕ_s'' , we can use the configuration shown in Fig. A.1 with a small analyzer angle $\delta \sim 0.2°$ instead of 0° that effectively determine the small p- component of the reflected light [100]. The light intensity after the analyzer is

$$\begin{aligned} I_{Kerr} &= |E_A^p\cos\delta\ + E_A^s\sin\delta|^2 \\ &\approx |E_A^p + E_A^s\delta|^2 \\ &= |E_A^s|^2\,|\delta + \phi_s' + i\phi_s''|^2 \end{aligned} \tag{A.7a}$$

If ϕ_s' and ϕ_s'' are small,

$$\begin{aligned} I_{Kerr} &\approx |E_A^s|^2\,(\delta^2 + 2\delta\phi_s') \\ &\equiv I_{zero}(1 + \frac{2\phi_s'}{\delta}). \end{aligned} \tag{A.7b}$$

Where I_{zero} is the intensity at zero Kerr rotation. To measure ϕ''_s, we placed a quarter-wave plate in front of the analyzer, Eq. (A.7b) becomes

$$I_{zero}(1+\frac{2\phi''_s}{\delta}). \tag{A.7c}$$

Replacing the measurement results of α, β, ϕ'_s, and ϕ''_s (assume $r_{sp} \sim r_{ps}$) into Eqs. (A.3a), (A.3b), we can obtain R_{pp} ($\tan\Psi_{pp}$ and Δ_{pp}).

We evaluate the effect from the off-diagonal terms by comparing the results with and without R_{sp} and R_{ps} . We show the results of a MBE-grown GaAs sample at 12 T as an example in Fig. A.2. We can find that the difference between the two different treatments is small and does not affect the interpretation of the data. Thus, we neglect the effect of the off-diagonal terms on the diagonal terms of the GaAs sample in this work.

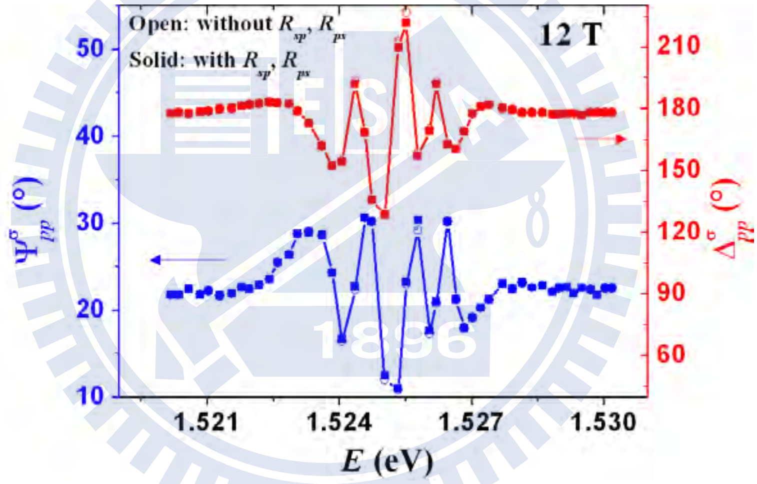

FIGURE A.2: Comparison of Ψ^{σ}_{pp} (left-axis) and Δ^{σ}_{pp} (right-axis) spectra of GaAs epitaxial layer at 12 T with (solid) and without (open) the contribution of R_{sp} and R_{ps} .

Appendix B

Error Analysis of Ellipsometry Parameters

The small fluctuations $d\Psi_{pp}^{\mathrm{eff}}$ and $d\Delta_{pp}^{\mathrm{eff}}$ can be obtained from the derivative of Eqs. (2.11a) and (2.11b).

$$d\Psi_{pp}^{\mathrm{eff}} = [\frac{\cos^2\Psi_{pp}^{\mathrm{eff}}(\tan^2 P + \tan^2\Psi_{pp}^{\mathrm{eff}})^2}{4\tan\Psi_{pp}^{\mathrm{eff}}\tan^2 P}]d\alpha, \tag{B.1a}$$

and

$$d\Delta_{pp}^{\mathrm{eff}} = \frac{1}{\sin\Delta_{pp}^{\mathrm{eff}}(1-\alpha^2)^{3/2}}[(\alpha^2-1)d\beta - (\alpha\beta)d\alpha]. \tag{B.1b}$$

As $P \sim \Psi_{pp}^{\mathrm{eff}}$ and $\Delta_{pp}^{\mathrm{eff}} \sim 90^\circ$($\alpha$ and $\beta \sim 0$ from Eqs. (2.11a) and (2.11b)), both $d\Psi_{pp}^{\mathrm{eff}}$ and $d\Delta_{pp}^{\mathrm{eff}}$ are minimized. That is, for a rotating-analyzer ellipsometer, a better precision can be achieved if the light before the rotating analyzer is nearly circular polarized, i.e. $P \sim \Psi_{pp}^{\mathrm{eff}}$ and $\Delta_{pp}^{\mathrm{eff}} \sim 90^\circ$.

The small fluctuations of the Fourier coefficients $d\alpha$ and $d\beta$ can be derived from Eq. (2.10). The Fourier coefficients α', β' and the average intensity I_D' with small fluctuations of the intensities dI_i and the analyzer angles dA_i ($i = 1, 2, 3, ...N$) can be written as

$$\alpha' = \frac{2}{I_D' N}\sum_{i=1}^{N}(I_i + dI_i)\cos[2(A_i + dA_i)], \tag{B.2a}$$

and

$$\beta' = \frac{2}{I_D' N}\sum_{i=1}^{N}(I_i + dI_i)\sin[2(A_i + dA_i)]. \tag{B.2b}$$

We assume that the fluctuations of intensities and analyzer angles are both constants, i.e. $dI_i = dI_D = dI$ and $dA_i = dA$, for each analyzer angle A_i when α, β are small ($I_i \sim I_D$). By expanding the equations above and dropping the smallest terms, we can obtain

$$d\alpha = \frac{-\delta}{1+\delta}\alpha + \frac{-\sin 2dA}{1+\delta}\beta + \frac{\delta}{1+\delta}\frac{2}{N}\sum_{i=1}^{N}\cos 2A_i, \tag{B.3a}$$

and

$$d\beta = \frac{-\delta}{1+\delta}\beta + \frac{-\sin 2dA}{1+\delta}\alpha + \frac{\delta}{1+\delta}\frac{2}{N}\sum_{i=1}^{N}\sin 2A_i, \tag{B.3b}$$

where δ is defined as dI/I_D. If A_i are chosen symmetrically (i.e. A_i and $A_i + 180°$ for $A_i < 90°$), the last term in both Eqs. (B.3a) and (B.3b) becomes zero. The related parameters causing the error of the Fourier coefficients are the intensity fluctuation δ, the random error of the analyzer angle dA, the random choice of the analyzer angles (the last summation terms of Eqs. (B.3a) and (B.3b)) and the choice of the polarizer angle Π.

Appendix C

Extreme Value and Its Corresponding Analyzer angle of a RAE Intensity Distribution

To find out the maximum/minimum intensity of an ellipse and the corresponding analyzer angle A_c, we differentiate Eq. (2.9a) with respect to A. The angle A_c satisfies the relation

$$\tan(2A_c) = \frac{\beta}{\alpha}. \tag{C.1}$$

Substituting Eqs. (C.1), (2.11a) and (2.11b) into Eq. (2.9a) and analyzing the sign of Eq. (2.9a) (see Table C.1), we can find that the maximum intensity will be in the first and the third quadrants if $0^\circ \leqslant \Delta_{pp} < 90^\circ(\beta \geqslant 0)$, and in the second and the fourth quadrants if $90^\circ \leqslant \Delta_{pp} \leqslant 180^\circ(\beta \leqslant 0)$.

Because the domain of Δ_{pp} is in the range of 0° to 180° for $\cos\Delta_{pp}$ in Eq. (2.11b), we cannot distinguish whether Δ_{pp} is larger than 180° or not. For example, $\Delta_{pp} = 150^\circ$ and $\Delta_{pp} = 210^\circ(-150^\circ)$ show exactly the same elliptical intensity distribution for an identical Ψ_{pp}. However,we can determine the handedness of the polarisation state of the reflected light or the sign of Δ_{pp} with the help of using a quarter-wave plate before the rotating analyser. if a quarter-wave plate is added in front of a rotating analyzer, the maximum intensities will be in different quadrants, and thus the Δ_{pp} values can be identified. (see Fig. C.1).

Table C.1: Maximum and minimum values of the elliptical intensity distribution for A_c in different domains.

Domain	β/α	**Maximum** $(\beta \geqslant 0)$	**Minimum** $(\beta \leqslant 0)$
$0^\circ \leqslant 2A_c < 90^\circ$	$\geqslant 0$	$1 + \alpha \cos 2A_c + \beta \sin 2A_c$	$1 - \lvert\alpha\rvert \cos 2A_c - \lvert\beta\rvert \sin 2A_c$
$90^\circ \leqslant 2A_c \leqslant 180^\circ$	$\leqslant 0$	$1 + \lvert\alpha\rvert\, \lvert\cos 2A_c\rvert + \beta \sin 2A_c$	$1 - \alpha\, \lvert\cos 2A_c\rvert - \lvert\beta\rvert \sin 2A_c$

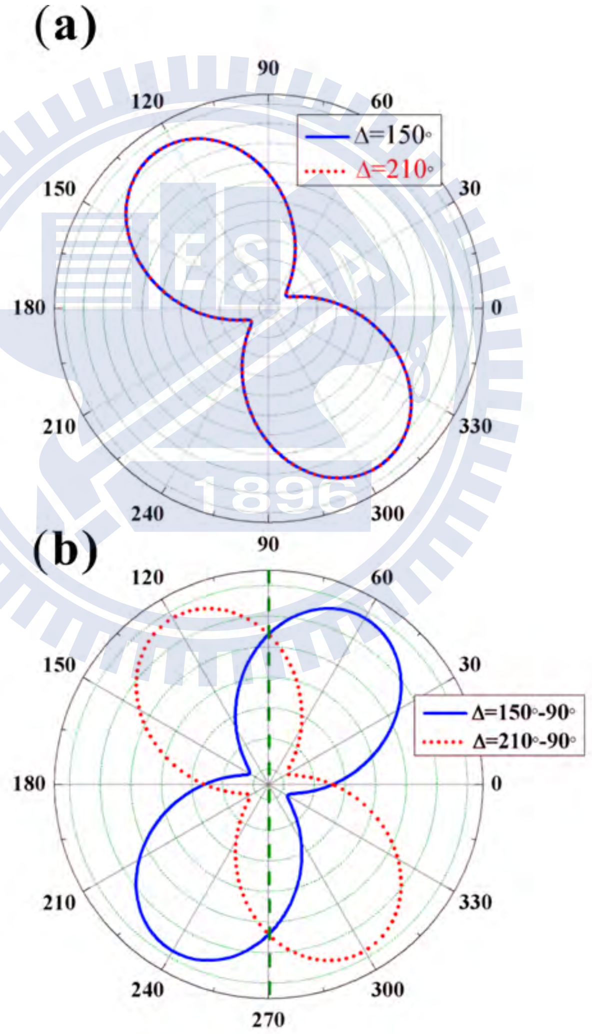

Figure C.1: Comparison of the elliptical intensity distributions with (b) and without (a) a quarter wave plate.

Appendix D

Finite-Well with Effective Mass Mismatch at Heterojuctions

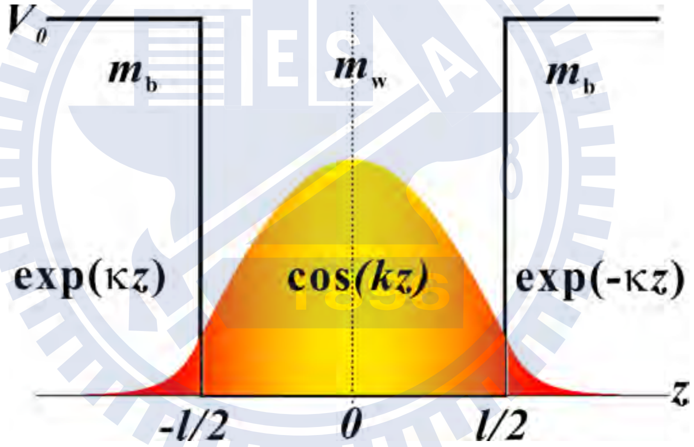

FIGURE D.1: Diagram of a wavefunction in a QW.

The Schrödinger equation can be written for each region as follows

$$
\begin{aligned}
[-\frac{\hbar^2}{2m_{\mathrm{b}}(E_n)}\frac{\partial^2}{\partial z^2}+V_0]\varphi(z) &= E_n\varphi(z),\ z\leq -\frac{l}{2} && \text{(D.1a)}\\
-\frac{\hbar^2}{2m_{\mathrm{w}}(E_n)}\frac{\partial^2}{\partial z^2}\varphi(z) &= E_n\varphi(z),\ -\frac{l}{2}\leq\ z\leq\frac{l}{2} && \text{(D.1b)}\\
[-\frac{\hbar^2}{2m_{\mathrm{b}}(E_n)}\frac{\partial^2}{\partial z^2}+V_0]\varphi(z) &= E_n\varphi(z),\ z\geq -\frac{l}{2} && \text{(D.1c)}
\end{aligned}
$$

Considering the symmetry of the problem, the solutions are either even parity or odd parity. The wavefunctions for the even parity states yield

$$\begin{aligned} \varphi(z) &= B\exp(\kappa z),\ z \le -\frac{l}{2} && \text{(D.2a)} \\ \varphi(z) &= A\cos(kz),\ -\frac{l}{2} \le\ z \le \frac{l}{2} && \text{(D.2b)} \\ \varphi(z) &= B\exp(-\kappa z),\ z \ge \frac{l}{2} && \text{(D.2c)} \end{aligned}$$

where

$$k = \frac{\sqrt{2m_{\mathrm{w}}E_n}}{\hbar}, \qquad \text{and} \qquad \kappa = \frac{\sqrt{2m_{\mathrm{b}}(V_0 - E_n)}}{\hbar}. \tag{D.3}$$

The boundary conditions[1] of the envelope functions for electron transport across a heterojunction are [101, 102]:

$$\text{both} \qquad \varphi(z) \qquad \text{and} \qquad \frac{1}{m}\frac{\partial}{\partial z}\varphi(z) \qquad \text{continuous.} \tag{D.4}$$

Thus we can obtain the relation between k and κ

$$\frac{\kappa}{k} = \frac{m_{\mathrm{b}}}{m_{\mathrm{w}}}\tan(\frac{kl}{2}). \tag{D.5}$$

Replacing Eg. (D.3) to Eg. (D.5) and taking the derivative of both sides to l, we can obtain

$$\frac{\partial E_n}{\partial l} = \frac{2E_n\digamma}{l\digamma + \frac{\sqrt{2}\hbar[m_{\mathrm{b}}+m'_{\mathrm{b}}(E_n-V_0)]}{\sqrt{m'_{\mathrm{b}}(V_0-E_n)}} + \frac{E_n l\digamma m'_{\mathrm{w}}}{m_{\mathrm{w}}} + \frac{\sqrt{2}\hbar\tan\eta[2E_n m_{\mathrm{w}}m'_{\mathrm{b}}+m_{\mathrm{b}}(m_{\mathrm{w}}-E_n m'_{\mathrm{w}})]}{(E_n m_{\mathrm{w}}^3)^{1/2}}}, \tag{D.6}$$

where $m'_{\mathrm{b}} = \partial m_{\mathrm{b}}/\partial E_n$, $m'_{\mathrm{w}} = \partial m_{\mathrm{w}}/\partial E_n$, $\digamma = m_{\mathrm{b}}\sec^2\eta$, and $\eta = (E_n m_{\mathrm{w}} l^2/2\hbar^2)^{1/2}$. And considering the symmetry and using the normalization condition

$$|A|^2\int_0^{l/2}\cos^2 kz\ \ dz + |B|^2\int_{l/2}^{\infty}\exp(-2\kappa z)\ \ dz = \frac{1}{2}, \tag{D.7}$$

we can obtain the normalization coefficients

$$B^2 = \frac{e^{\kappa l}(1+\cos kl)}{l + k^{-1}\sin kl + \kappa^{-1}(1+\cos kl)}, \tag{D.8a}$$

and

$$A^2 = \frac{2}{l + k^{-1}\sin kl + \kappa^{-1}(1+\cos kl)}. \tag{D.8b}$$

---

[1] The conditions have been know as the BenDaniel-Duke boundary conditions.

Bibliography

[1] R. M. A. Azzam and N. M. Bashara. *Ellipsometry and Polarized Light*. North-Holland Amsterdam, 1977.

[2] D. H. Goldstein and E. Collett. *Polarized light, 2nd Edition*. Marcel Dekker Inc., 2003.

[3] H. Tompkins and E. A. Irene. *Handbook of Ellipsometry*. Access Online via Elsevier, 2005.

[4] O. Voskoboynikov, C. M. J. Wijers, J. L. Liu, and C. P. Lee. Magneto-optical response of layers of semiconductor quantum dots and nanorings. *Physical Review B*, 71(24), 2005.

[5] C. M. J. Wijers, J. H. Chu, J. L. Liu, and O. Voskoboynikov. Optical response of layers of embedded semiconductor quantum dots. *Physical Review B*, 74(3), 2006.

[6] C. M. J. Wijers, O. Voskoboynikov, and J. L. Liu. A hybrid model for the magneto-optics of embedded nano-objects. In M. Stutzmann, editor, *Physica Status Solidi C - Current Topics in Solid State Physics, Vol 3, No 11*, of *Physica Status Solidi C-Current Topics in Solid State Physics*, pages 3782–3785. 2006.

[7] L. M. Thu and O. Voskoboynikov. Magneto-optics of layers of double quantum dot molecules. *Physical Review B*, 80(15), 2009.

[8] O. Voskoboynikov. Hybrid model for simulation of magneto-optical response of layers of semiconductor nano-objects. *International Journal for Multiscale Computational Engineering*, 8(2):195–205, 2010.

[9] J. Tignon, T. Hasche, D. S. Chemla, H. C. Schneider, F. Jahnke, and S. W. Koch. Unified picture of polariton propagation in bulk GaAs semiconductors. *Physical Review Letters*, 84(15):3382–3385, 2000.

[10] H. C. Schneider, F. Jahnke, S. W. Koch, J. Tignon, T. Hasche, and D. S. Chemla. Polariton propagation in high quality semiconductors: Microscopic theory and experiment versus additional boundary conditions. *Physical Review B*, 63(4):045202, 2001.

[11] S. Schumacher, G. Czycholl, and F. Jahnke. Microscopic description of exciton-polaritons in thin semiconductor layers. *Phys. Stat. Sol.(b)*, 234(1): 172–182, 2002.

[12] S. Schumacher, G. Czycholl, F. Jahnke, I. Kudyk, H. I. Rückmann, J. Gutowski, A. Gust, G. Alexe, and D. Hommel. Polariton propagation in shallow-confinement heterostructures: Microscopic theory and experiment showing the breakdown of the dead-layer concept. *Physical Review B*, 70 (23):235340, 2004.

[13] D. Schiumarini, N. Tomassini, L. Pilozzi, and A. D'Andrea. Polariton propagation in weak-confinement quantum wells. *Physical Review B*, 82(7):075303, 2010.

[14] A. Berger and M. R. Pufall. Generalized magneto-optical ellipsometry. *Applied Physics Letters*, 71:965, 1997.

[15] G. Neuber, R. Rauer, J. Kunze, T. Korn, C. Pels, G. Meier, U. Merkt, J. Backstrom, and M. Rubhausen. Temperature-dependent spectral generalized magneto-optical ellipsometry. *Applied Physics Letters*, 83(22):4509–4511, 2003.

[16] M. Schubert, T. Hofmann, and C. M. Herzinger. Generalized far-infrared magneto-optic ellipsometry for semiconductor layer structures: determination of free-carrier effective-mass, mobility, and concentration parameters in n-type GaAs. *Journal of the Optical Society of America A-Optics Image Science and Vision*, 20(2):347–356, 2003.

[17] T. Hofmann, U. Schade, C. M. Herzinger, P. Esquinazi, and M. Schubert. Terahertz magneto-optic generalized ellipsometry using synchrotron and blackbody radiation. *Review of Scientific Instruments*, 77(6), 2006.

[18] K. Mok, N. Du, and H. Schmidt. Vector-magneto-optical generalized ellipsometry. *Review of Scientific Instruments*, 82(3):033112, 2011.

[19] J. J. Hopfield. Theory of the contribution of excitons to the complex dielectric constant of crystals. *Physical Review*, 112(5):1555–1567, 1958.

[20] H. Haug and S. Koch. On the theory of laser action in dense exciton systems. *Physica Status Solidi (b)*, 82(2):531–543, 1977.

[21] S. W. Koch, H. Haug, G. Schmieder, W. Bohnert, and C. Klingshirn. Stimulated intrinsic recombination processes in II-VI compounds. *Physica Status Solidi (b)*, 89(2):431–440, 1978.

[22] H. Haug and S.W. Koch. *Quantum Theory of the Optical and Electronic Properties of Semiconductors*. World Scientific Publishing Company Incorporated, 2004.

[23] H.M. Gibbs, G. Khitrova, and S.W. Koch. Exciton-polariton light-semiconductor coupling effects. *Nature Photonics*, 5(5):273–273, 2011.

[24] J. Keeling, F. M. Marchetti, M. H. Szymaska, and P. B. Littlewood. Collective coherence in planar semiconductor microcavities. *Semiconductor Science and Technology*, 22(5):R1, 2007.

[25] J. Kasprzak, M. Richard, A. Baas, B. Deveaud, R. André, and J-Ph. Poizat. Second-order time correlations within a polariton Bose-Einstein condensate in a CdTe microcavity. *Physical Review Letters*, 100(6):067402, 2008.

[26] Andrei Faraon, Ilya Fushman, Dirk Englund, Nick Stoltz, Petroff Pierre, and Vukovi Jelena. Coherent generation of non-classical light on a chip via photon-induced tunnelling and blockade. *Nature Physics*, 4(11):859–863, 2008.

[27] W. J. Johnston, M. Yildirim, J. P. Prineas, Arthur L. Smirl, H. M. Gibbs, and G. Khitrova. All-optical spin-dependent polarization switching in Bragg-spaced quantum well structures. *Applied Physics Letters*, 87(10):101113–101113–3, 2005.

[28] Zhenshan S. Yang, Nai H. Kwong, Rolf Binder, and Arthur L. Smirl. Stopping, storing, and releasing light in quantum-well Bragg structures. *JOSA B*, 22(10):2144–2156, 2005.

[29] Stefan Strauf. Quantum optics: Towards efficient quantum sources. *Nature Photonics*, 4(3):132–134, 2010.

[30] Dirk Englund, David Fattal, Edo Waks, Glenn Solomon, Bingyang Zhang, Toshihiro Nakaoka, Yasuhiko Arakawa, Yoshihisa Yamamoto, and Jelena Vukovi. Controlling the spontaneous emission rate of single quantum dots in a two-dimensional photonic crystal. *Physical Review Letters*, 95(1):013904, 2005.

[31] Julien Claudon, Joel Bleuse, Nitin Singh Malik, Maela Bazin, Prine Jaffrennou, Niels Gregersen, Christophe Sauvan, Philippe Lalanne, and Jean-Michel Gerard. A highly efficient single-photon source based on a quantum dot in a photonic nanowire. *Nature Photonics*, 4(3):174–177, 2010.

[32] S. I. Pekar. The theory of electromagnetic waves in a crystal in which excitons are produced. *Soviet Journal of Experimental and Theoretical Physics*, 6:785, 1958.

[33] J. J. Hopfield and D. G. Thomas. Theoretical and experimental effects of spatial dispersion on the optical properties of crystals. *Physical Review*, 132 (2):563–572, 1963.

[34] Roland Zeyher, Joseph L. Birman, and Wilhelm Brenig. Spatial dispersion effects in resonant polariton scattering. I. additional boundary conditions for polarization fields. *Physical Review B*, 6(12):4613–4616, 1972.

[35] C-S Ting, M. J. Frankel, and J. L. Birman. Electrodynamics of bounded spatially dispersive media: The additional boundary conditions. *Solid State Communications*, 17(10):1285–1289, 1975.

[36] P. Halevi and R. Fuchs. Generalised additional boundary condition for nonlocal dielectrics: I. reflectivity. *Journal of Physics C: Solid State Physics*, 17 (21):3869, 1984.

[37] Jun-ichi Kusano, Gerrit E. W. Bauer, and Yoshinobu Aoyagi. Two-dimensional versus three-dimensional excitons in wide GaAs quantum wells. *Journal of Applied Physics*, 75(1):289–296, 1994.

[38] A. Tredicucci, Y. Chen, F. Bassani, J. Massies, C. Deparis, and G. Neu. Center-of-mass quantization of excitons and polariton interference in GaAs thin layers. *Physical Review B*, 47(16):10348–10357, 1993.

[39] Y. Chen, F. Bassani, J. Massies, C. Deparis, and G. Neu. Interference of the exciton-polariton waves in GaAs thin layers. *EPL (Europhysics Letters)*, 14 (5):483, 1991.

[40] R. P. Seisyan. Diamagnetic excitons and exciton magnetopolaritons in semiconductors. *Semiconductor Science and Technology*, 27(5):053001, 2012.

[41] J. J. Davies, D. Wolverson, V. P. Kochereshko, A. V. Platonov, R. T. Cox, J. Cibert, H. Mariette, C. Bodin, C. Gourgon, E. V. Ubyivovk, Yu P. Efimov, and S. A. Eliseev. Motional enhancement of exciton magnetic moments in Zinc-Blende semiconductors. *Physical Review Letters*, 97(18):187403, 2006.

[42] V. P. Kochereshko, L. C. Smith, J. J. Davies, R. T. Cox, A. Platonov, D. Wolverson, H. Boukari, H. Mariette, J. Cibert, and M. Wiater. Excitons in motion: universal dependence of the magnetic moment on kinetic energy. *Physica Status Solidi (b)*, 245(6):1059–1063, 2008.

[43] D.K. Loginov. Magnetic-field-induced polariton effects in light reflection spectra of structures with wide exciton quantum wells. *Physics of the Solid State*, 52(1):70–78, 2010.

[44] D. K. Loginov, V. P. Kochereshko, R. T. Cox, L. Besombes, H. Mariette, J. J. Davies, D. Wolverson, and L. C. Smith. Excitonic polaritons in transverse magnetic fields. *Physica Status Solidi (b)*, 247(6):1528–1530, 2010.

[45] L. V. Butov, C. W. Lai, D. S. Chemla, Yu E. Lozovik, K. L. Campman, and A. C. Gossard. Observation of magnetically induced effective-mass enhancement of quasi-2D excitons. *Physical Review Letters*, 87(21):216804, 2001.

[46] Yu E. Lozovik, I. V. Ovchinnikov, S. Yu Volkov, L. V. Butov, and D. S. Chemla. Quasi-two-dimensional excitons in finite magnetic fields. *Physical Review B*, 65(23):235304, 2002.

[47] D. D. Sell, R. Dingle, S. E. Stokowski, and J. V. DiLorenzo. Observation of polaritons in GaAs: A new interpretation of the free-exciton reflectance and luminescence. *Physical Review Letters*, 27(24):1644, 1971.

[48] D. D. Sell. Resolved free-exciton transitions in the optical-absorption spectrum of GaAs. *Physical Review B*, 6(10):3750, 1972.

[49] A. M. White, P. J. Dean, L. L. Taylor, R. C. Clark, D. J. Ashen, and J. B. Mullin. The photoluminescence spectrum of bound excitons in indium phosphide and gallium arsenide. *Journal of Physics C: Solid State Physics*, 5(13):1727, 1972.

[50] R. Dingle. Magneto-optical investigation of the free-exciton reflectance from high-purity epitaxial GaAs. *Physical Review B*, 8(10):4627–4633, 1973.

[51] D. D. Sell, S. E. Stokowski, R. Dingle, and J. V. DiLorenzo. Polariton reflectance and photoluminescence in high-purity GaAs. *Physical Review B*, 7(10):4568, 1973.

[52] F. Willmann, S. Suga, W. Dreybrodt, and K. Cho. Magneto-reflectance of the 1s exciton ground states in InP and GaAs. *Solid State Communications*, 14(8):783–786, 1974.

[53] M. Schubert, B. Rheinlander, J. A. Woollam, B. Johs, and C. M. Herzinger. Extension of rotating-analyzer ellipsometry to generalized ellipsometry: Determination of the dielectric function tensor from uniaxial TiO_2. *Journal of the Optical Society of America A-Optics Image Science and Vision*, 13(4): 875–883, 1996.

[54] W. Budde. Photoelectric analysis of polarized light. *Applied Optics*, 1(3): 201–205, 1962.

[55] D. E. Aspnes. Optimizing precision of rotating-analyzer and rotating-compensator-ellipsometers. *Journal of the Optical Society of America A-Optics Image Science and Vision*, 21(3):403–410, 2004.

[56] John David Jackson. *Classical Electrodynamics, 3rd Edition*. Wiley-VCH, July 1998. ISBN 0-471-30932-X.

[57] A. Baldereschi and Nunzio C. Lipari. Energy levels of direct excitons in semiconductors with degenerate bands. *Physical Review B*, 3(2):439–451, 1971.

[58] Jasprit Singh. *Physics of Semiconductors and their Heterostructures*, McGraw-Hill, New York, 1993.

[59] K. Cho, S. Suga, W. Dreybrodt, and F. Willmann. Theory of degenerate 1s excitons in Zinc-Blende-type crystals in a magnetic field: Exchange interaction and cubic anisotropy. *Physical Review B*, 11(4):1512–1521, 1975.

[60] M. Altarelli and Nunzio O. Lipari. Perturbation-theory investigation of the exciton ground state of cubic semiconductors in a magnetic field. *Physical Review B*, 7(8):3798, 1973.

[61] G.H. Cocoletzi and W.L. Mochán. Excitons: from excitations at surfaces to confinement in nanostructures. *Surface Science Reports*, 57(1):1–58, 2005.

[62] Frank L Pedrotti and Leno S Pedrotti. *Introduction to optics, 2nd Edition*, Prentice-Hall Englewood Cliffs, 1993.

[63] G. H. Cocoletzi and W. Luis Mochán. Spatial dispersion effects on the optical properties of an insulator-excitonic-semiconductor superlattice. *Physical Review B*, 39(12):8403–8408, 1989.

[64] G. H. Cocoletzi, A. Ramrez Perucho, and W. Luis Mochán. Optical properties of insulator-excitonic-semiconductor superlattices in the presence of inert layers. *Physical Review B*, 44(20):11514–11517, 1991.

[65] B. Flores-Desirena, F. Pérez-Rodríguez, and P. Halevi. Interaction of exciton polaritons with the surface potential of thin semiconductor films: s-polarization geometry. *Physical Review B*, 50(8):5404–5411, 1994.

[66] H. A. Coyotécatl and G. H. Cocoletzi. Optical response of localized excitons near surfaces of multilayer systems. *Journal of Physics: Condensed Matter*, 10(1):79, 1999.

[67] Takuji Tanaka, Zhenlong Zhang, Masao Nishioka, and Yasuhiko Arakawa. Magnetic field dependence of exciton oscillator strength by measurements of magnetoexcitonpolariton mode splitting in quantum wells with a microcavity. *Applied Physics Letters*, 69(7):887–889, 1996.

[68] S. B. Nam, D. C. Reynolds, C. W. Litton, R. J. Almassy, T. C. Collins, and C. M. Wolfe. Free-exciton energy spectrum in GaAs. *Physical Review B*, 13 (2):761, 1976.

[69] J. S. Blakemore. Semiconducting and other major properties of gallium arsenide. *Journal of Applied Physics*, 53(10):R123–R181, 1982.

[70] W. Ekardt, K. Lösch, and D. Bimberg. Determination of the analytical and the nonanalytical part of the exchange interaction of InP and GaAs from polariton spectra in intermediate magnetic fields. *Physical Review B*, 20(8): 3303, 1979.

[71] F. Pérez-Rodríguez and P. Halevi. Interaction of excitons with a generalized morse surface potential: s-polarized incident light at a semiconductor surface. *Physical Review B*, 45(20):11854–11862, 1992.

[72] F. Pérez-Rodríguez and P. Halevi. Quantized polarization waves of excitons at semiconductor surfaces. *Physical Review B*, 48(3):2016–2019, 1993.

[73] Robin F. C. Farrow. *Molecular Beam Epitaxy: applications to key materials*. Access Online via Elsevier, 1995.

[74] K. Mok, G.J. Kovcs, J. McCord, L. Li, M. Helm, and H. Schmidt. Magneto-optical coupling in ferromagnetic thin films investigated by vector-magneto-optical generalized ellipsometry. *Physical Review B*, 84(9):094413, 2011.

[75] Daniel Schmidt, Chad Briley, Eva Schubert, and Mathias Schubert. Vector magneto-optical generalized ellipsometry for sculptured thin films. *Applied Physics Letters*, 102(12):123109, 2013.

[76] P. Khne, Vanya Darakchieva, Rositsa Yakimova, J.D. Tedesco, R.L. Myers-Ward, C.R. Eddy Jr, D.K. Gaskill, C.M. Herzinger, J.A. Woollam, and M. Schubert. Polarization selection rules for inter-Landau-level transitions in epitaxial graphene revealed by the infrared optical Hall effect. *Physical Review Letters*, 111(7):077402, 2013.

[77] C. Kittel and P. McEuen. *Introduction to solid state physics, 7th Edition*. Wiley, New York, 1976.

[78] G. Bastard. *Wave mechanics applied to semiconductors*. Les Éditions de Physique, 1988.

[79] A. Gold. Electronic transport properties of a two-dimensional electron gas in a silicon quantum-well structure at low temperature. *Physical Review B*, 35(2):723–733, 1987.

[80] H. Sakaki, T. Noda, K. Hirakawa, M. Tanaka, and T. Matsusue. Interface roughness scattering in GaAs/AlAs quantum wells. *Applied Physics Letters*, 51(23):1934–1936, 1987.

[81] R. Gottinger, A. Gold, G. Abstreiter, G. Weimann, and W. Schlapp. Interface roughness scattering and electron mobilities in thin GaAs quantum wells. *EPL (Europhysics Letters)*, 6:183, 1988.

[82] F. Szmulowicz, S. Elhamri, H. J. Haugan, G. J. Brown, and W. C. Mitchel. Demonstration of interface-scattering-limited electron mobilities in InAs/-GaSb superlattices. *Journal of Applied Physics*, 101:043706, 2007.

[83] J. M. Li, J. J. Wu, X. X. Han, Y. W. Lu, X. L. Liu, Q. S. Zhu, and Z. G. Wang. A model for scattering due to interface roughness in finite quantum wells. *Semiconductor Science and Technology*, 20:1207, 2005.

[84] B.R. Bennett, R. Magno, J.B. Boos, W. Kruppa, and M.G. Ancona. Antimonide-based compound semiconductors for electronic devices: A review. *Solid-State Electronics*, 49(12):1875–1895, 2005.

[85] R. L. Kallaher, J. J. Heremans, N. Goel, S. J. Chung, and M. B. Santos. Spin-orbit interaction determined by antilocalization in an InSb quantum well. *Physical Review B*, 81(7):075303, 2010.

[86] S. Nadj-Perge, V. S. Pribiag, J. W. G. van den Berg, K. Zuo, S. R. Plissard, E. P. A. M. Bakkers, S. M. Frolov, and L. P. Kouwenhoven. Spectroscopy of spin-orbit quantum bits in indium antimonide nanowires. *Physical Review Letters*, 108(16):166801, 2012.

[87] T. Ando, A.B. Fowler, and F. Stern. Electronic properties of two-dimensional systems. *Reviews of Modern Physics*, 54:437–672, 1982.

[88] H. C. Huang, O. Voskoboynikov, and C. P. Lee. Spin-orbit interaction and electron elastic scattering from impurities in quantum wells. *Physical Review B*, 67(19):195337, 2003.

[89] Frank Stern and W. E. Howard. Properties of semiconductor surface inversion layers in the electric quantum limit. *Physical Review*, 163(3):816–835, 1967.

[90] I. Vurgaftman, J. R. Meyer, and L. R. Ram-Mohan. Band parameters for III-V compound semiconductors and their alloys. *Journal of Applied Physics*, 89:5815, 2001.

[91] Chris G. Van de Walle. Band lineups and deformation potentials in the model-solid theory. *Physical Review B*, 39(3):1871–1883, 1989.

[92] M. Levinshtein, M. S. Shur, and S. Rumyanstev. *Handbook series on semiconductor parameters*. World Scientific, 1996.

[93] T. H. Glisson, J. R. Hauser, M. A. Littlejohn, and C. K. Williams. Energy bandgap and lattice constant contours of III-V quaternary alloys. *Journal of Electronic Materials*, 7(1):1–16, 1978.

[94] Y. Li, Y. Zhang, and Y. Zeng. Electron mobility in modulation-doped AlSb/InAs quantum wells. *Journal of Applied Physics*, 109:073703, 2011.

[95] P. Harrison. *Quantum wells, wires and dots.* Wiley Online Library, 2000.

[96] A. Gold. Scattering time and single-particle relaxation time in a disordered two-dimensional electron gas. *Physical Review B*, 38(15):10798, 1988.

[97] F. Szmulowicz and G.J. Brown. Calculation of interface roughness scattering-limited vertical and horizontal mobilities in InAs/GaSb superlattices as a function of temperature. *Journal of Applied Physics*, 113(1): 014302, 2013.

[98] A. Agrawal, A. Ali, R. Misra, P.E. Schiffer, B.R. Bennett, J.B. Boos, and S. Datta. Experimental determination of dominant scattering mechanisms in scaled InAsSb quantum well. pages 27–28. IEEE, 2011.

[99] A. Ali, H. Madan, R. Misra, A. Agrawal, P. Schiffer, J.B. Boos, B.R. Bennett, and S. Datta. Experimental determination of quantum and centroid capacitance in arsenide-antimonide quantum-well MOSFETs incorporating nonparabolicity effect. *Electron Devices, IEEE Transactions on*, (99):1–7, 2011.

[100] Z. Q. Qiu and S. D. Bader. Surface magneto-optic Kerr effect. *Review of Scientific Instruments*, 71:1243, 2000.

[101] J. W. Conley, C. B. Duke, G. D. Mahan, and J. J. Tiemann. Electron tunneling in metal-semiconductor barriers. *Physical Review*, 150(2):466–469, 1966.

[102] D. J. BenDaniel and C. B. Duke. Space-charge effects on electron tunneling. *Physical Review*, 152(2):683–692, 1966.

Vita

Name: Sheng-Kai Su (蘇聖凱)

Date of birth: October 13, 1983

Sex: Male

Education:
National Chiao Tung University Ph. D. September, 2007 ~ June, 2014
Department of Electronics Engineering & Institute of Electronics

National Chiao Tung University M. S. September, 2006 ~ June, 2007
Department of Electronics Engineering & Institute of Electronics

National Chiao Tung University B. S. September, 2002 ~ June, 2006
Department of Electrophysics

Title of Ph. D. Dissertation:
Low Temperature and High Magnetic Field Ellipsometer Design and Measurment & Well-thickness Dependent Electron Transport Effective Mass and Mobility in Low Bandgap Quantum Wells

Honor/Award

[1] 第一屆 i-ONE國際儀器科技創新獎 (業餘組) 佳作 (2009)

Publication List

1. [Full paper] **S. K. Su**, O. Voskoboynikov, L. C. Li, Y. W. Suen, and C. P. Lee, "*GaAs polariton propagation in magnetic field: Oblique incident ellipsometry measurement*" (unpublished).

2. [Full paper, 2 points] **S. K. Su**, L. C. Li, Y. W. Suen, J. Y. Wu, H. R. Kuo, Y. T. Sung, C. P. Lee, and O. Voskoboynikov, "*Low Temperature and High Magnetic Field Spectroscopic Ellipsometry System*", Rev. Sci. Instrum. **85**, 055101 (2014).

3. [Full paper, 2 points] **S. K. Su**, C. P. Lee, and O. Voskoboynikov, "*Well-thickness dependent electron transport effective mass mobility in Sb-based quantum wells*" Physica E **48**, 80-84 (2013).

4. [Conference paper, 1 points] **S. K. Su**, L. C. Li, Y. W. Suen, Y. T. Sung, C. P. Lee, and O. Voskoboynikov, "*Magneto-optical study of GaAs exciton using ellipsometry*" The 19th international conference on Electronic Properties of Two-Dimensional Systems (EP2DS19), Tallahassee, Florida, USA (Jul. 25-29, 2011).

5. [Conference paper] **S. K. Su**, L. C. Li, Y. W. Suen, J. Y. Wu, H. R. Kuo, Y. T. Sung, O. Voskoboynikov, and C. P. Lee, "*Ellipsometer System for Low Temperature and High Magnetic Field* " The 19th International Conference on the Application of High Magnetic Fields in Semiconductor Physics and Nanotechnology (HMF-19), Fukuoka, Japan, (Aug. 1-6, 2010).

6. [Full paper] C. H. Lin, H. S. Lin, **S. K. Su**, S. D. Lin, C. P. Lee, and K. W. Sun, "*Shape dependent carrier dynamics in InAs/GaAs nanostructures* " J. Appl. Phys. **106**, 113522 (2009).

7. [Letter] C. H. Lin, H. S. Lin, C. C. Huang, **S. K. Su**, S. D. Lin, K.W. Sun, C. P. Lee, Y.K. Liu, M. D. Yang, and J. L. Shen, "*Temperature Dependence of Time-resolved Photoluminescence Spectroscopy in InAs/GaAs Quantum Ring*" Appl. Phys. Lett. **94**, 183101 (2009).